Multiscale Modelling and Simulation of Rapid Granular Flows

Dissertation

zur

Erlangung des Doktorgrades (Dr. rer. nat.)

der

Mathematisch-Naturwissenschaftlichen Fakultät

der

Rheinischen Friedrich-Wilhelms-Universität Bonn

vorgelegt von

Birte Domnik

aus

Bielefeld

Bonn 2013

Angefertigt mit Genehmigung der Mathematisch-Naturwissenschaftlichen Fakultät der
Rheinischen Friedrich-Wilhelms-Universität Bonn
am Steinmann-Institut für Geologie, Mineralogie und Paläontologie

1. Gutachter: Prof. Dr. Stephen A. Miller
2. Gutachter: Prof. Dr. Andreas Kemna

Tag der Promotion: 5. November 2013
Erscheinungsjahr: 2013

Abstract

Granular flows are often encountered in geophysical contexts like debris flows, snow and rock avalanches, and also in transport processes in engineering applications. The damage caused by geophysical mass flows can be huge. Hence, there is a need for an appropriate description and efficient simulation of these types of flows. Depth-averaged models and simulations have been largely successful in describing granular flows and avalanches down channels and slopes. Their success is basically founded on their simplicity and a typically small computational effort. However, for a physically complete description of the flow dynamics, without reduction of the information through the flow depth, a non depth-averaged, full dimensional model is required.

In this work, we present full dimensional models and simulations for rapid granular free-surface flows in steep inclined channels, including the initiation process of material stored in a silo and the deposition processes when hitting an obstacle. We address the problem of appropriate boundary conditions for granular flows and develop a multiscale coupled two-dimensional Coulomb-viscoplastic model with non-zero slip velocities, which provides a complete description of the flow dynamics, on the one hand, and a moderate computational effort, on the other hand. This coupled model is based on a full two-dimensional, non depth-averaged model (N-DAM), however, in regions with negligible changes of the flow variables along the flow depth a reduced one-dimensional, depth-averaged model (DAM) is used.

The presented model includes some basic features and observed phenomena in dense granular flows like the exhibition of a yield strength and a non-zero slip velocity. The most important model parameters are the internal and bed friction angle, which are related to the yield strength of the granular material and its interaction with the solid boundary, respectively. The yield strength describes the solid-liquid transitions, and, here, it is considered to be pressure-dependent to account for the frictional nature of granular materials. The numerical treatment of the model requires the set up of a novel pressure equation, which relates the pressure to the bottom boundary velocities.

The numerical results demonstrate a substantial influence of the chosen boundary condition on the flow dynamics. The Coulomb-viscoplastic sliding law reveals completely different flow dynamics compared to the commonly used no-slip boundary condition, for example, the Coulomb-viscoplastic sliding law induces shearing mainly close to the sliding surface in agreement with observations. We demonstrate that the performance of presented multiscale coupling strategy is very high. Its use can reduce the run-time of the simulation from days (for full two-dimensional model) to hours (for coupled model) for the configurations considered here. This shows that the coupled model, which retains all the basic physics of the flow, is an attractive alternative to an expensive, full two-dimensional model. This is a substantial advantage when considering large scale geophysical mass flows in nature such as snow avalanches, rock avalanches, debris flows, and landslides. The coupled two-dimensional Coulomb-viscoplastic model predicts front positions, flow velocities, and deposit heights, which are in very good agreement with data obtained from laboratory experiments.

Zusammenfassung

Granulare Flüsse treten in der Natur in Form von geophysikalischen Flüssen, wie zum Beispiel Schuttströmen, Schnee- und Steinlawinen, aber auch in industriellen Transportprozessen auf. Da der durch geophysikalische Massenflüsse verursachte Schaden sehr groß sein kann, ist eine geeignete Beschreibung und effiziente Simulation dieser Flüsse notwendig. Tiefenintegrierte Modelle und Simulationen wurden bereits sehr erfolgreich zur Beschreibung von granularen Flüssen und Lawinen verwendet, vor allem aufgrund ihrer Schlichtheit und ihrem typischerweise kleinen Rechenaufwand. Eine physikalisch vollständige Beschreibung der Flussdynamik, ohne Informationsverlust entlang der Flusstiefe, erfordert allerdings ein nicht tiefenintegriertes Modell.

In der vorliegenden Arbeit wird das schnelle Fließen granularen Materials entlang eines stark geneigten Kanals, einschließlich dem beginnenden Fließprozess in einem Silo und dem Abbrems- und Ablagerungsprozess beim Auftreffen auf ein Hindernis, modelliert und simuliert. Wir widmen uns dem Problem geeigneter Randbedingungen und entwickeln ein gekoppeltes, zwei-dimensionales, viskoplastisches Modell mit nicht verschwindenden Rutschgeschwindigkeiten, welches eine vollständige Beschreibung der Flussdynamik bei einem moderaten Rechenaufwand liefert. Das gekoppelte Modell basiert auf einem vollen zwei-dimensionalen, nicht tiefenintegrierten Modell (N-DAM), wobei in Regionen mit geringfügigen Änderungen der Flussvariablen entlang der Flusstiefe ein ein-dimensionales, tiefenintegriertes Modell (DAM) verwendet wird.

Das vorgestellte Modell berücksichtigt einige grundlegende Eigenschaften von kompakten granularen Flüssen wie das Aufweisen einer Fließgrenze und einer nicht verschwindenden Rutschgeschwindigkeit. Diese werden durch die zwei wichtigsten Modellparameter, dem Inneren- und dem Bodenreibungswinkel, beschrieben. Die Fließgrenze definiert den Übergang vom ruhenden zum fließenden Material und wird hier als druckabhängig angenommen, um die granulare Reibung zu berücksichtigen. Die numerische Lösung des Modells erfordert die Formulierung einer neuartigen Druckgleichung, die den Druck mit den Randgeschwindigkeiten am Boden verknüpft.

Die numerischen Ergebnisse zeigen einen beachtlichen Einfluss der gewählten Randbedingung auf die Flussdynamik. So erzeugt das Coulombsche Rutschgesetz eine komplett andere Flussdynamik im Vergleich zu der häufig benutzten Haftbedingung, wie zum Beispiel eine Scherung des Materials hauptsächlich in Bodennähe (und nicht entlang der kompletten Flusstiefe) entsprechend experimenteller Beobachtungen. Die präsentierte Mehrskalen-Kopplungsstrategie ist sehr leistungsstark und erlaubt die Reduktion der Simulationslaufzeit von Tagen (für ein komplettes zwei-dimensionales Modell) auf Stunden (für ein gekoppeltes Modell) für die hier betrachteten Konfigurationen. Somit stellt das gekoppelte Modell, das alle grundlegenden physikalischen Fließprozesse berücksichtigt, eine attraktive Alternative zu zeitintensiven, komplett zwei-dimensionalen Modellen dar. Dies ist ein wesentlicher Vorteil bei der Betrachtung von großskaligen geophysikalischen Massenflüssen. Die mit dem gekoppelten Modell prognostizierten Frontpositionen, Fließgeschwindigkeiten und Ablagerungen zeigen eine sehr gute Übereinstimmung mit Daten aus experimentellen Versuchen.

Contents

Chapter 1

Introduction

Granular materials possess unique properties, which differ from those associated with ordinary solids, liquids, and gases (Jaeger et al., 1996; Aranson and Tsimring, 2006; Pudasaini and Hutter, 2007). Due to their rich phenomenology, granular materials pose an interesting but also challenging field in science and technology. A typical granular material is sand, which can exhibit solid-like characteristics (e.g., when arranged on a pile or located at a sandy-beach) but also fluid-like characteristics (e.g., when used in an hourglass). In general, granular materials can show properties similar to that of solids, liquids and gases, depending on how it is prepared and excited (Jaeger et al., 1996). Granular materials flowing like liquids are termed as granular flows, which are often encountered in geophysical contexts like debris flows, landslides, pyroclastic flows, snow and rock avalanches, and also in transport processes in engineering applications (Ancey, 2007; Pudasaini and Hutter, 2007). The damage caused by geophysical mass flows can be huge. Therefore, there is a need for an appropriate description and efficient simulation of this type of flows, for example, in order to predict the flow path, flow height, flow velocities and impact forces on buildings in hazardous areas (Barbolini et al., 2000; Christen et al., 2010; Fischer et al., 2012).

Hydrodynamic models provide a basic approach in modelling granular flows (Jaeger et al., 1996; Ancey, 2007; Pudasaini and Hutter, 2007). However, they require an appropriate rheology, describing the response of granular materials to applied loads in terms of constitutive laws, and appropriate boundary conditions. This is a very challenging task, as "no constitutive law can reproduce the diversity of behavior observed with a cohesionless granular material" (Forterre and Pouliquen, 2008). In many applications, flows of dense granular materials can be described by viscoplastic constitutive laws (Jop et al., 2006; Ancey, 2007; Balmforth and Frigaard, 2007; Forterre and Pouliquen, 2008; Moriguchi et al., 2009). However, the explicit rheology depends on the specific situation, that is, for example, the material composition, boundary conditions, and the driving forces of the flow, and is a current subject in scientific studies (Jop et al., 2006; Moriguchi et al., 2009). Usually, granular materials flow over frictional bottom surfaces. This generates non-zero and non-trivial slip velocities at the bottom boundary (Massoudi and Phuoc, 2000; Pudasaini et al., 2005c, 2007; Platzer et al., 2007a,b; Pudasaini and Hutter, 2007). This observation contradicts with the widely used no-slip boundary condition, in which the slip velocity is set to zero (Jop

et al., 2006; Moriguchi et al., 2009). Already Jaeger et al. (1996) was aware of this issue:

> "... when attempting a hydrodynamic approach to granular flow, we are still at a loss as to how to treat the boundaries correctly, while it is obvious that the ordinary hydrodynamic nonslip boundary assumptions are invalid".

In classical depth-averaged modelling, slip at the bottom boundary can be described by assuming a Coulomb friction law. Due to depth-averaging, the model equations contain this boundary condition only implicitly.

Depth-averaged models (DAM) and simulations have been largely successful in describing different kinds of granular flows, because of their simplicity and typically small computational effort compared to full dimensional, non depth-averaged models (N-DAM) (Savage and Hutter, 1989; Gray et al., 1999; Tai et al., 2002; Pudasaini and Hutter, 2003, 2007). However, their success is limited to the prediction of flow depths and mean velocities. Moreover, in several applications the assumptions made within the depth-averaged framework are fulfilled only very weakly. One basic assumption of depth-averaged models is the shallowness approximation in which it is supposed that a typical flow depth is small in comparison to a typical extent of the avalanche. Furthermore, assumptions concerning the stress states within the material are made. It is supposed that the normal pressure in the flow depth direction is given by the hydrostatic pressure and that downslope and cross-slope normal pressures vary linearly with the normal pressure through the depth of the avalanche. These assumptions may apply for an undisturbed flow but may be violated, e.g., during the flow inception or when the flow hits an obstacle.

In this work we focus on modelling and simulation of gravity-driven granular free-surface flows in steep inclined channels, leading to rapid avalanches. We address the problem of appropriate boundary conditions for granular flows and develop a full two-dimensional pressure-dependent Coulomb viscoplastic model with non-zero slip velocities, which provides a complete description of the flow dynamics on the one hand, and a moderate computational effort on the other hand, when coupled to a depth-averaged model. This coupled two-dimensional Coulomb-viscoplastic model is numerically solved, and the simulation results are compared with data obtained from laboratory experiments. Additionally, we also studied energies associated with rapid granular flows, which are useful in avalanche defence, hazard mitigation and planning. They can also serve as a basis for studies of dissipative mechanisms within the avalanching body with the objective of formulating appropriate constitutive relations.

This work is organised as follows:

In Chapter 2 we provide a theoretical background of this work. This includes descriptions of basic physical properties and some phenomena of granular matter and an explanation of a general hydrodynamic approach, which is useful in modelling dense granular flows.

Chapter 3 addresses the problem of appropriate bottom boundary conditions for granular flows. We present a full two-dimensional, Coulomb-viscoplastic model, which

includes basic features and observed phenomena in dense granular flows like the exhibition of a yield strength and a non-zero slip velocity. The interaction of the flow with the solid boundary is modelled by a pressure and rate-dependent Coulomb-viscoplastic sliding law. The numerical treatment of the presented model requires the set up of a novel pressure equation, which defines the pressure independent of the bottom boundary velocities. A simple viscoplastic granular flow down an inclined channel subject to slip or no-slip at the bottom boundary is studied numerically with the marker-and-cell method.

In Chapter 4 we extend this Coulomb-viscoplastic model by proposing a pressure-dependent yield strength to account for the frictional nature of granular materials. The yield strength is related to the internal friction angle of the material and plays an important role, e.g., in deposition processes. This full two-dimensional, extended Coulomb-viscoplastic model belongs to the class of non depth-averaged models (N-DAM), which involve high computational complexity and require relatively large computing power compared to depth-averaged models (DAM). This motivates the development of a multiscale strategy in which the full two-dimensional, non depth-averaged model is coupled with a one-dimensional, depth-averaged model. In the coupled model N-DAM is used except in regions with negligible momentum transfer along the flow depth direction, where DAM is used instead.

In Chapter 5 a rapid flow of granular material down an inclined channel impinging on a rigid wall in the further downstream is simulated by numerically solving the coupled two-dimensional Coulomb-viscoplastic model. The simulated flow velocities and flow fronts in the channel and the deposition heights at the wall are compared with data obtained from laboratory experiments.

Chapter 6 presents a complete expression for the total energy associated with a rapid frictional granular shear flow down an inclined surface. For this purpose, thickness-averaged mass and momentum conservation laws are utilised. The total energy function takes into account gravity, friction, kinetic energy, and bulk deformation. Simulations and experimental results are used to describe the total energy of non-stationary flows.

Chapter 7 summarises the relevant aspects of the proposed models and numerical simulation methods and strategies, and the main numerical results. We finalise with an outlook on the further use and the impact of the findings provided by this work.

In Appendix A we explicitly compute a strain rate dependent Coulomb friction law on an arbitrarily orientated, flat boundary.

In Appendix B the proposed discretisations of the momentum equations in N-DAM are presented explicitly.

Appendix C explains the implementation of the multiscale coupling strategy, which is introduced in Chapter 4.

Chapter 2

Theoretical Background

This chapter starts with a description of basic physical properties and some phenomena of granular matter. As granular materials exhibit a rich phenomenology (Jaeger et al., 1996; Aranson and Tsimring, 2006; Pudasaini and Hutter, 2007), we focus on several aspects relevant to rapid granular flows. Afterwards, some basic theoretical concepts are presented which are required for a hydrodynamic-type description of dense granular flows. The hydrodynamic approach is based on the continuum assumption and requires an appropriate rheology describing the response of granular materials to applied loads.

2.1 Granular matter

A conglomeration of solid, macroscopic particles is called granular matter, when the size of its constituents (called grains) is large enough ($\geq 1\,\mu$m) such that Brownian motion is irrelevant (Aranson and Tsimring, 2006). When the particles are non-cohesive, attractive forces between them are negligible, so that the grains are generally not bound together. Therefore, granular materials differ from ordinary solids, liquids, and gases, which constitute the usual states of matter, although they all represent many-particle systems. A typical granular material is sand, which consists of individual grains with sizes ranging from 0.063 mm to 2 mm. The grains can be rough or smooth, quite spherical or even non-spherical. Some additional examples of granular materials are nuts, coal, rice, coffee, corn flakes, fertiliser, ball bearings, and much more. For dry grains, an interstitial fluid, such as air or water, can often be neglected (Jaeger et al., 1996), as it does not contribute substantially to the momentum transfer of the solid particles (Pudasaini and Hutter, 2007). The uniqueness of granular materials is generated by two important aspects (Jaeger et al., 1996): (i) in contrast to usual gases, the ordinary temperature plays no role as the gravitational potential energy is much greater than the thermal energy due to the relatively large particle masses (compared to that of molecules or atoms), and (ii) the particle collisions are inelastic, that means energy is lost in particle interactions.

Interestingly, in certain situations granular materials can show properties similar to that of solids, liquids, and gases, depending on how it is prepared and excited (Jaeger et al., 1996; Pudasaini and Hutter, 2007). For example, one can walk on a sandy beach

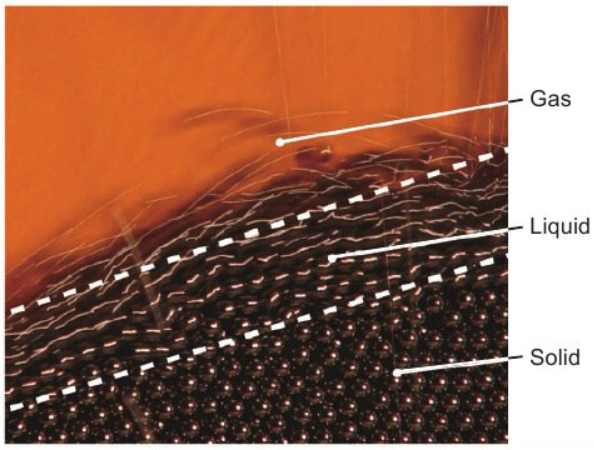

Figure 2.1: Illustration of solid, liquid and gas flow regimes of steel beads poured on a pile (Forterre and Pouliquen, 2008).

without much deforming it, which demonstrates the solid properties of sand. But on the contrary, if one picks up a handful of sand, it runs through the fingers like a liquid. Therefore, the flow of granular materials can be classified into three different regimes (MiDi, 2004; Pudasaini and Hutter, 2007; Forterre and Pouliquen, 2008): (i) a dense quasi-static regime characterised by slow deformations and frictional contacts between the grains, (ii) a gaseous regime, in which the grains are far apart from one another, strongly agitated, and primarily interact by collisions leading to a very rapid and dilute flow, and (iii) an intermediate liquid regime in which the material is dense but flows like a liquid and both particle collisions and frictional particle contacts may be important. These three regimes can be observed simultaneously, when pouring grains on a steep enough pile, Fig. 2.1.

The transition between the solid and liquid regime is described by a friction criterion, which requires that the ratio of shear to normal stress reaches a critical value (Forterre and Pouliquen, 2008). This becomes visible when a sand pile at rest is tilted several degrees above the a critical angel, called angle of repose, which leads to the development of a boundary layer of flowing grains at the pile's surface, Fig. 2.2. The yield strength of granular materials originates from the friction between the grains and the entanglement of the particles.

The transition between liquid and gaseous regimes depends on the restitution coefficient c_r, which is a measure of the inelasticity of particle collisions, and the volume fraction, which is defined as the ratio of the volume occupied by the grains to the total volume, $\Phi = V_g/V$. The volume fraction is related to the bulk density ρ of the flow by $\Phi = \rho/\rho_g$, where ρ_g is the particle density of the grains. The role of the restitution coefficient becomes clear when considering a sequence of inelastic collisions, in which the kinetic energy of the particles and hence the inter-particle distances are successively decreased. However, the properties of the liquid regime are almost insensitive to the restitution coefficient (MiDi, 2004), although c_r describes the transition to the gaseous regime. For dense granular flows, in many situations the variations of the

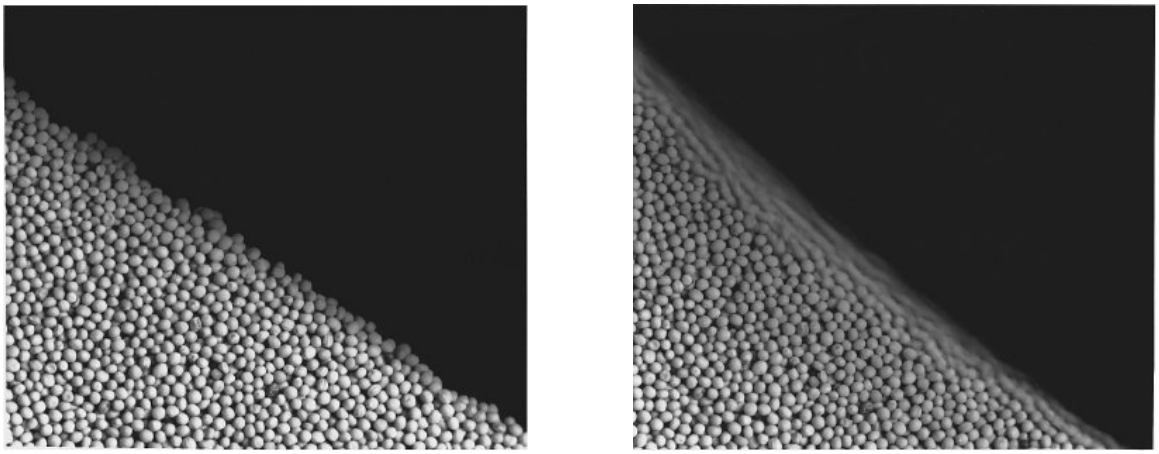

(a) Granular pile at rest. (b) Granular pile with flowing surface layer.

Figure 2.2: A pile of mustard seeds that is tilted to an angle lower than the angle of repose (a) and the same pile after the slope has been increased slightly larger than the angle of repose (b) (Jaeger et al., 1996).

volume fraction (density) are small and can be neglected (Pudasaini and Hutter, 2007; Forterre and Pouliquen, 2008).

Physics of granular materials spans a wide variety of phenomena, which are discussed in detail in Pudasaini and Hutter (2007). One common phenomenon is the Brazil nut effect, which describes the accumulation of large particles (Brazil nuts) at the top, because they cannot be packed so dense like smaller particles. Note that although size separation seems to violate the increase of entropy principle, this principle does not apply here, as entropy considerations can easily be outweighed by dominant dynamical effects (ordinary temperature plays no role in granular materials) (Jaeger et al., 1996). Reynolds (1885) introduced the notion of dilatancy, which states that shearing a granular material usually leads to a bulk volume increase. This implies that under simple shear the bulk density decreases and normal stresses are generated. The dilatation phenomenon arises from the need of a densely packed granular material to expand in order to make enough room for allowing grains to move. As density variations may be neglected for dense granular flows, dilatation of the material can also be neglected.

In this work, we focus on the dense granular flow regime, which is most often encountered in applications. In the following, the basic theoretical concepts required for a hydrodynamic-type description of dense granular flows are presented.

2.2 Continuum mechanics approach

In the continuum mechanics approach, a material is considered as a continuum rather than a collection of its constituents (e.g., molecules or grains for granular materials). The continuum assumption is valid on length scales much greater than that of the distances between the individual constituents. For fluids, the dimensionless Knudsen

number is a measure for the validity of the continuum assumption (Young et al., 2010). It is defined as $Kn = \lambda/d$, where λ is the the mean free path and d is a characteristic physical length scale (for example the grain diameter). The mean free path is the average distance travelled by a moving particle between successive impacts (collisions), which modify its direction or energy or other particle's properties. If the Knudsen number is near or greater than one, the mean free path of a molecule is comparable to a length scale of the problem (like for granular gases), and the continuum assumption of fluid mechanics is no longer a valid approximation. In this case, statistical methods must be used (Jenkins and Savage, 1983; Lun et al., 1984; Hwang and Hutter, 1995).

A moving continuum material can be described by the following balance laws (Hutter and Jöhnk, 2004)

$$\dot{\rho} + \rho \nabla \cdot \mathbf{u} \qquad \text{Balance of mass}\,, \tag{2.1}$$

$$\rho \dot{\mathbf{u}} - \nabla \cdot \boldsymbol{\sigma} - \rho \mathbf{b} = \mathbf{0} \qquad \text{Balance of linear momentum}\,, \tag{2.2}$$

$$\boldsymbol{\sigma} = \boldsymbol{\sigma}^T \qquad \text{Balance of angular momentum}\,, \tag{2.3}$$

$$\rho \dot{e} - \boldsymbol{\sigma} : (\nabla \mathbf{u}) + \nabla \cdot \mathbf{q} - \rho s_e = 0 \qquad \text{Balance of energy}\,. \tag{2.4}$$

In the above equations, ρ is the bulk density, $\mathbf{u}$ is the velocity, $\boldsymbol{\sigma}$ is the Cauchy stress tensor, $\mathbf{b}$ is the body force density, e is the specific internal energy, $\mathbf{q}$ is the heat flux, s_e is the specific energy supply, $\dot{\rho}$ denotes the total time derivative of ρ, $\nabla \cdot \mathbf{u}$ is the divergence of $\mathbf{u}$, $\nabla \mathbf{u}$ is the gradient of $\mathbf{u}$, the superscript T denotes transpose, and the colon denotes the inner matrix product. In this work, gravity driven flows are considered, and the body force density is given by the gravitational acceleration $\mathbf{g}$. The balance equations (2.1)-(2.4) form a system of partial differential equations and are completed by kinematic relations, constitutive equations, and appropriate boundary and initial conditions. Often materials can be assumed to be incompressible, i.e. having a constant density. Then, the mass balance (2.1) simplifies to

$$\nabla \cdot \mathbf{u} = 0\,, \tag{2.5}$$

which is called the continuity equation. For an incompressible material, the energy balance (2.4) is not required to close the system, and the motion is described by the momentum balance (2.2) and the continuity equation (2.5). The stress tensor appearing in (2.2) has to be modelled by appropriate constitutive relations depending on the material and flow configurations. The angular momentum balance (2.3) requires the symmetry of the stress tensor.

Stress is defined as the force acting on a surface per unit area. The three-dimensional state of stress (at a point inside a material) is defined by the second-order (Cauchy) stress tensor

$$\boldsymbol{\sigma} = \begin{pmatrix} \sigma_{xx} & \sigma_{xy} & \sigma_{xz} \\ \sigma_{yx} & \sigma_{yy} & \sigma_{yz} \\ \sigma_{zx} & \sigma_{zy} & \sigma_{zz} \end{pmatrix}. \tag{2.6}$$

The stress vector (traction) across a surface with normal vector $\mathbf{n}$ is then given by $\mathbf{s} = \boldsymbol{\sigma}\mathbf{n}$. The normal stress on a surface is defined as the projection of the stress vector on the surface normal, $\sigma = \boldsymbol{\sigma}\mathbf{n} \cdot \mathbf{n}$. Here, we use the sign convention in which

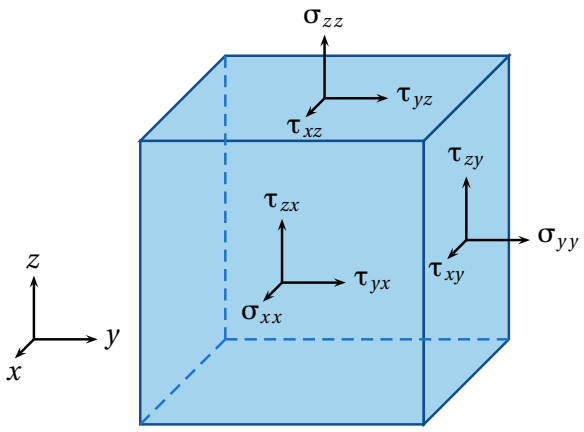

Figure 2.3: Stresses on the surfaces of an infinitesimal small control volume, whose surface normals are aligned with the coordinate axes of a Cartesian coordinate system.

compressional stresses are negative while tensional stresses are positive. The normal pressure on a surface is then defined as $N = -\boldsymbol{\sigma}\mathbf{n} \cdot \mathbf{n}$. The shear stress on a surface is given by the projection of the stress vector along the surface tangent $\mathbf{t}$, $T = \boldsymbol{\sigma}\mathbf{n} \cdot \mathbf{t}$. In a Cartesian coordinate system, the diagonal elements of the stress tensor (2.6) are normal stresses on surfaces whose normals are aligned with the coordinate axis, Fig. 2.3. The off-diagonal elements represent shear stresses on theses surfaces and are often denoted as τ_{ij} instead of σ_{ij}. The conservation of angular momentum (2.3) implies that the stress tensor is symmetric: $\sigma_{xy} = \sigma_{yx}$, $\sigma_{xz} = \sigma_{zx}$ and $\sigma_{yz} = \sigma_{zy}$. Therefore, the stress tensor is specified by only six (instead of nine) independent components. These depend on the chosen coordinate system. Therefore, the stress tensor is often characterised by its eigenvalues, which are called principal stresses. Alternatively, tensor invariants can be used, which are also independent of the coordinate system. These invariants are defined by the coefficients of the characteristic polynomial of the tensor (Akivis and Goldberg, 1972; Fischer, 2008). For a symmetric tensor $\boldsymbol{\sigma}$ of dimension $N^d = 3$, three tensor invariants can be found, which are given by

$$I_\sigma = \operatorname{tr} \boldsymbol{\sigma} , \tag{2.7}$$

$$II_\sigma = \frac{1}{2} \left((\operatorname{tr} \boldsymbol{\sigma})^2 - \operatorname{tr} \boldsymbol{\sigma}^2 \right) , \tag{2.8}$$

$$III_\sigma = \det \boldsymbol{\sigma} , \tag{2.9}$$

where $\operatorname{tr} \boldsymbol{\sigma}$ denotes the trace and $\det \boldsymbol{\sigma}$ the determinant of the tensor $\boldsymbol{\sigma}$. For $N^d = 2$, the right-hand sides of (2.8) and (2.9) are the same and only two invariants exist

$$I_\sigma = \operatorname{tr} \boldsymbol{\sigma} , \tag{2.10}$$

$$II_\sigma = \det \boldsymbol{\sigma} . \tag{2.11}$$

The stress tensor can be decomposed into a volumetric stress tensor $\boldsymbol{\sigma}_V$, which tends to change the volume of the stressed body, and a deviatoric stress tensor $\boldsymbol{\sigma}_D$, which

tends to distort it:

$$\boldsymbol{\sigma} = \boldsymbol{\sigma}_V + \boldsymbol{\sigma}_D\,, \quad \text{with} \quad \boldsymbol{\sigma}_V = \frac{I_\sigma}{N^d}\mathbb{1}\,, \tag{2.12}$$

where $\mathbb{1}$ denotes the unit tensor. This construction implies that the trace of the deviatoric stress tensor vanishes, $\operatorname{tr}\boldsymbol{\sigma}_\mathrm{D} = 0$. With the definition of an isotropic pressure

$$p = -\frac{I_\sigma}{N^d}\,, \tag{2.13}$$

the volumetric stress tensor is then related to p by $\boldsymbol{\sigma}_V = -p\mathbb{1}$.

2.3 Rheology

The stress tensor appearing in the linear momentum balance, (2.2), has to be modelled by appropriate constitutive equations depending on the material and flow configurations. This belongs to the field of rheology. Constitutive relations provide a connection between applied stresses to deformations. A constitutive relation is not a fundamental law of nature but an approximation that holds in some materials under certain conditions.

When stress is applied to a 'solid body', both its size and shape may change. The deformations can be described by a linearised, symmetric strain tensor of second-order

$$\boldsymbol{\varepsilon} = \frac{1}{2}\left((\nabla\mathbf{d}) + (\nabla\mathbf{d})^T\right)\,, \tag{2.14}$$

where $\mathbf{d}$ is the displacement vector (Hutter and Jöhnk, 2004). For an elastic material, the stress-strain relation is linear and is described by Hook's law

$$\boldsymbol{\sigma} = \boldsymbol{C}\boldsymbol{\varepsilon}\,, \tag{2.15}$$

where $\boldsymbol{C}$ is the fourth-order elasticity tensor. Equation (2.15) implies that when the applied stress is removed, an elastic material returns to its original configuration. Hook's law is a good model for most solids, as long as the forces and deformations are small enough.

In an analogous manner, the viscous deformation of a fluid is described by the symmetric, second-order strain rate tensor

$$\mathbf{D} = \dot{\boldsymbol{\varepsilon}} = \frac{1}{2}\left((\nabla\mathbf{u}) + (\nabla\mathbf{u})^T\right)\,, \tag{2.16}$$

where $\mathbf{u}$ is the velocity vector (Landau and Lifshitz, 1987). Note that the velocity gradient, $\nabla\mathbf{u}$, includes not only deformations but also rotations, which do not contribute to the rate of change of the deformation. Therefore, the actual strain rate in (2.16) is given by the symmetric part of the velocity gradient. The diagonal elements of the strain rate tensor are called compression rates and the off-diagonal elements, the shear rates. For an incompressible material, the velocity field is divergence-free (2.5) and the trace of the strain rate tensor vanishes, $\operatorname{tr}\mathbf{D} = 0$.

A simple incompressible Newtonian fluid (e.g., water under ordinary conditions) is described by the linear relationship

$$\boldsymbol{\sigma}_D = 2\eta\mathbf{D}\,, \tag{2.17}$$

where the proportionality constant η is called (dynamic) viscosity. As only the ratio η/ρ appears in the momentum balance, the kinematic viscosity is defined by $\nu = \eta/\rho$.

Fluids which do not obey the simple linear relationship with constant viscosity (2.17) are called non-Newtonian fluids. For a non-Newtonian fluid, the relation between the stress and the strain rate can often be expressed in an analogous manner as for a Newtonian fluid

$$\boldsymbol{\sigma}_D = 2\eta_{\text{eff}}\mathbf{D}\,, \tag{2.18}$$

where the Newtonian viscosity η is now replaced by an effective viscosity η_{eff}, which is not constant and may, e.g., depend on the strain rate. Replacing the stress tensor in the linear momentum balance (2.2) with (2.12) and using (2.5), (2.13), and (2.18) yields the momentum balance for an incompressible, non-Newtonian fluid

$$\rho\dot{\mathbf{u}} = -\nabla p + \eta\Delta\mathbf{u} + 2\left(\nabla\cdot\left(\eta_{\text{eff}} - \eta\right)\mathbf{D}\right) + \rho\mathbf{g}\,. \tag{2.19}$$

For a constant viscosity, $\eta_{\text{eff}} = \eta$, this reduces to the well-known Navier-Stokes equations for an incompressible Newtonian fluid

$$\rho\dot{\mathbf{u}} = -\nabla p + \eta\Delta\mathbf{u} + \rho\mathbf{g}\,. \tag{2.20}$$

The Navier–Stokes equations are nonlinear partial differential equations of second order. The nonlinearity is due to convective acceleration, which is contained in $\dot{\mathbf{u}}$. In general, solutions of (2.20) cannot be calculated analytically. Rather, they are most often solved numerically.

When a stress is applied to a plastic material, it may first deform elastically and, when the applied stress exceeds the yield strength, it starts to deform plastically and a non-reversible deformation of the material occurs. Flows of dense granular materials may exhibit both viscous and plastic deformations and are in many situations well described by viscoplastic constitutive laws (Jop et al., 2006; Ancey, 2007; Balmforth and Frigaard, 2007; Forterre and Pouliquen, 2008; Moriguchi et al., 2009), in which the material yields and starts to flow once a yield criterion is satisfied. The yield criterion depends on the stress state and a yield strength τ_y, which has to be exceeded to start flowing. A two-dimensional yield surface can be used to represent the yield criterion in the three-dimensional principal stress space. Viscoplastic flows belong to the category of non-Newtonian fluids and a typical constitutive equation for elastic and viscoplastic flow regimes, respectively, reads

$$\begin{aligned} &\sqrt{II_{\sigma_D}} < \tau_y: \qquad \boldsymbol{\sigma} = \mathbf{C}\boldsymbol{\varepsilon}\,, \\ &\sqrt{II_{\sigma_D}} \geq \tau_y: \qquad \boldsymbol{\sigma}_D = 2\eta_{\text{eff}}\mathbf{D}, \quad \text{with} \quad \eta_{\text{eff}} = \eta + \frac{\tau_y}{||\mathbf{D}||}\,, \end{aligned} \tag{2.21}$$

where the norm of a tensor $\mathbf{D}$ has been defined through its second invariant as $||\mathbf{D}|| = 2\sqrt{|II_D|}$. As the second invariant of the deviatoric stress tensor, II_{σ_D}, is connected to

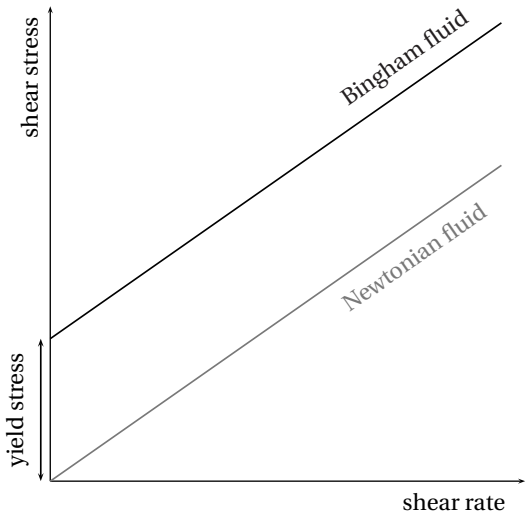

Figure 2.4: Relation of shear stress to shear rate for a Bingham and a Newtonian Fluid.

the elastic strain energy of distortion, a physical interpretation of (2.21) suggests that the material starts to flow when the distortion energy reaches a critical value (Hill, 1998). For a one-dimensional shear flow, the shear rate $\partial_z u$ and the shear stress τ are related by

$$\tau = \tau_y + \eta\, \partial_z u\,, \tag{2.22}$$

for $\tau \geq \tau_y$. A lot of yield criteria for different specific situations have been proposed (Yu, 2006). Some common yield criteria in the field of granular flows are the von Mises criterion, the Drucker-Prager yield criterion and the Mohr-Coulomb failure criterion, each of them will be discussed in the following.

The von Mises yield criterion (von Mises, 1913) suggests that a material yields when II_{σ_D} reaches a critical constant value

$$\sqrt{II_{\sigma_D}} \geq \tau_y\,. \tag{2.23}$$

The von Mises yield criterion is assumed for Bingham materials (Bingham, 1922), Fig. 2.4.

In the Mohr-Coulomb failure criterion (Coulomb, 1776), a material yields (or fails) when the shear stress τ on the failure plane is related to the normal stress σ on this plane by

$$\tau = c + \sigma \tan\phi\,, \tag{2.24}$$

where ϕ is the internal friction angle and c is the cohesion of the material. For granular materials the internal friction angle is usually close to the angle of repose (Pudasaini and Hutter, 2007). The Mohr-Coulomb failure criterion can be illustrated with the aid of Mohr's circle, Fig. 2.5. Mohr's circle represents all possible stress states (σ, τ) at a fixed point within the material. For two-dimensional stress states, the centre σ_m and the radius r of the circle can be expressed by the principal stresses σ_1 and σ_2 (assume

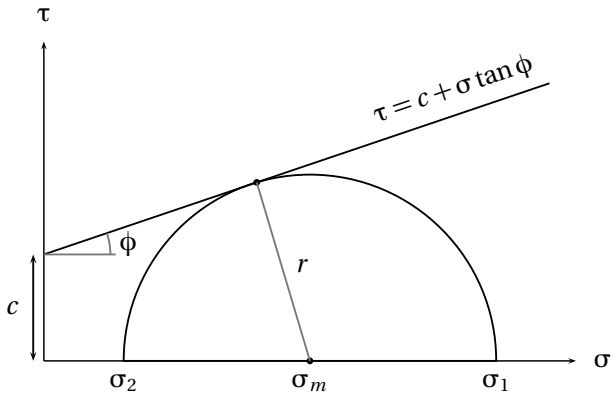

Figure 2.5: Mohr's circle and Mohr-Coulomb failure criterion for two-dimensional stress states. Shear-stresses are denoted by τ and normal stresses by σ. The circle is defined by its radius r and its centre σ_m, which can be computed from the the principal stresses σ_1 and σ_2.

$\sigma_1 > \sigma_2$) as

$$\sigma_m = \frac{\sigma_1 + \sigma_2}{2}\,, \tag{2.25}$$

$$r = \frac{\sigma_1 - \sigma_2}{2}\,. \tag{2.26}$$

By using some geometrical arguments (Pudasaini and Hutter, 2007), the Mohr-Coulomb failure criterion (2.24) can be expressed by σ_m and r as

$$r = |\sigma_m| \sin\phi + c\cos\phi\,. \tag{2.27}$$

The Drucker-Prager yield criterion (Prager and Drucker, 1952) suggests that yielding of materials begins when $\sqrt{II_{\sigma_D}}$ reaches a critical value, the yield stress, which depends on the first invariant of the stress tensor (I_σ):

$$\sqrt{|II_{\sigma_D}|} \geq A + B\,|I_\sigma|\,, \tag{2.28}$$

where the constants A, B are to be determined (e.g., from experiments). As the first stress tensor invariant (I_σ) is related to the pressure (2.13), the Druck-Prager yield criterion assumes a pressure-dependent yield stress. The Drucker-Prager yield surface is a smooth version of the Mohr-Coulomb yield surface (for $N^d = 2$ they even coincidence). Therefore, the yield criterion (2.28) is often expressed in terms of the cohesion and the internal friction angle, which are used to describe the Mohr-Coulomb yield surface (Khan and Huang, 1995). In granular channel flows, the observed stress states are basically two-dimensional ($N^d = 2$) (Pudasaini et al., 2007; Pudasaini and Kröner, 2008). Then, the first stress tensor invariant (2.7) is expressed in terms of principal stresses as

$$I_\sigma = \sigma_1 + \sigma_2\,. \tag{2.29}$$

Equation (2.8) and the continuity equation (2.5) yields for the second invariant of the deviatoric stress tensor

$$II_{\sigma_D} = -\frac{1}{2}\mathrm{tr}\left(\boldsymbol{\sigma}_{\mathrm{D}}^2\right),$$

with (2.12), this reads:

$$\begin{aligned} II_{\sigma_D} &= -\frac{1}{2}\mathrm{tr}\left(\boldsymbol{\sigma} - \frac{\mathrm{I}_\sigma}{2}\mathbb{1}\right)^2 \\ &= -\frac{1}{2}\left(\mathrm{tr}\left(\boldsymbol{\sigma}^2\right) - \frac{\mathrm{I}_\sigma^2}{2}\right). \end{aligned}$$

When $\boldsymbol{\sigma}$ and I_σ are expressed in terms of principal stresses, one obtains

$$II_{\sigma_D} = -\frac{1}{4}\left(\sigma_1 - \sigma_2\right)^2. \tag{2.30}$$

With (2.25), (2.26), (2.29), and (2.30), the tensor invariants in (2.28) can be expressed by the centre of the Mohr's circle and its radius as

$$\begin{aligned} I_\sigma &= 2\sigma_m, \\ II_{\sigma_D} &= -r^2. \end{aligned}$$

With this, in two-dimensions, the Drucker-Prager yield criterion (2.28) reads

$$r \geq A + 2B\left|\sigma_m\right|. \tag{2.31}$$

By comparing (2.31) with the Mohr-Coulomb failure criterion (2.27), the constants A and B can be related to ϕ and c (for $N^d = 2$) as

$$A = c\cos\phi, \tag{2.32}$$

$$B = \frac{\sin\phi}{2}. \tag{2.33}$$

Together with (2.13), the Drucker-Prager yield criterion (2.28) for two-dimensional stress states can be written as

$$\sqrt{II_{\sigma_D}} \geq \tau_y, \quad \text{with} \quad \tau_y = c\cos\phi + p\sin\phi. \tag{2.34}$$

For a cohesionless dry granular material, the yield stress reduces to

$$\tau_y = p\sin\phi. \tag{2.35}$$

This equation states that the yield stress depends linearly on the isotropic pressure with a proportionality constant given by the sine of the internal friction angle for a Drucker-Prager type yield criterion.

Chapter 3

Full 2D Rapid Granular Chute Flows with a Slip Velocity*

We present a fully two-dimensional, novel Coulomb-viscoplastic sliding model, which includes some basic features and observed phenomena in dense granular flows like the exhibition of a yield strength and a non-zero slip velocity. The interaction of the flow with the solid boundary is modelled by a pressure and rate-dependent Coulomb-viscoplastic sliding law. The bottom boundary velocity is required for a fully two-dimensional model, whereas in classical, depth-averaged models its explicit knowledge is not needed. It is observed in experiments and in the field that in rapid flow of frictional granular material down the slopes, even the lowest particle layer in contact with the bottom boundary moves with a non-zero and non-trivial velocity. Therefore, the no-slip boundary condition, which is generally accepted for simulations of ideal fluid, e.g., water, is not applicable to granular flows. The numerical treatment of the Coulomb-viscoplastic sliding model requires the set up of a novel pressure equation, which defines the pressure independently of the bottom boundary velocities. These are dynamically and automatically defined by our Coulomb-viscoplastic sliding law for a given pressure. A simple viscoplastic granular flow down an inclined channel subject to slip or no-slip at the bottom boundary is studied numerically with the marker-and-cell method. The simulation results demonstrate the substantial influence of the chosen boundary condition. Compared to the commonly used no-slip boundary condition, the Coulomb-viscoplastic sliding law reveals completely different flow dynamics and flow depth variations of the field quantities, mainly the velocity and full dynamic pressure, and also other derived quantities, such as the bottom shear-stress and the mean shear rate. We show that for the proposed Coulomb-viscoplastic sliding law, observable shearing mainly takes place close to the sliding surface in agreement with observations but in contrast to the no-slip boundary condition.

*This chapter is based on: Domnik, B. and Pudasaini, S.P., 2012. Full two-dimensional rapid chute flows of simple viscoplastic granular materials with a pressure-dependent dynamic slip-velocity and their numerical simulations. Journal of Non-Newtonian Fluid Mechanics, 173:72–86.

3.1 Introduction

Granular flows play an important role in our daily life. They take place in form of geophysical and industrial mass flows and show very different phenomena. The flow of a granular avalanche is characterised by three different flow regimes: (i) the starting zone where rupture and fragmentation of the solid material occurs and/or the granular material begins to flow, (ii) the avalanching zone where the granular material reaches fast supercritical speed, and (iii) the run-out zone where the moving mass is decelerated and comes to a rather sudden standstill (Pudasaini et al., 2007). Observations, both in the laboratory and nature, show flow transitions from a subcritical to a supercritical regime after the flow release. In further downstream, a rapid flow regime develops, which is characterised by fairly uniform velocity profiles with depth, strong shearing in the vicinity of the base and dominant sliding at the base (Pudasaini and Hutter, 2007). In the deposition regime and, in particular, in the transition region from the rapid flow into the deposition zone, shock-like structures may form, and an overall depth flow changes into a surface boundary layer flow, which quickly slows down and eventually settles (Pudasaini et al., 2007).

Depth-averaged model equations and simulations have been largely successful in describing the flows of granular materials, avalanches, and debris flows down channels and slopes (Savage and Hutter, 1989; Gray et al., 1999; Pudasaini and Hutter, 2007; Pudasaini, 2012). However, the depth-averaged equations are restricted to smooth basal surfaces and smooth changes of the slopes. Those equations could not fully be applied when topography changes are large (large curvatures), in the vicinity of the flow obstacle interactions, during the depositions, for strongly converging and diverging flows (Pudasaini et al., 2008), in flow initiations, and also during the deposition processes. All these complex processes can typically be characterised by a dominant basal slip, followed by a region in vicinity of the sliding surface with strong velocity shearing along the flow depth, which merges into a plug-flow like region with weak velocity shearing.

The most important physical quantities in avalanche and granular flow dynamics are the velocity and pressure distribution through the depth and along the slope, evolution of the geometry, and the deposition profile. From a structural engineering and planning point of view, one must properly predict the flow field and estimate impact pressures on civil structures that may be hit by an avalanche, in order to adequately design buildings, roadways, and rail transportation in mountainous regions. Equally important is to know the depth and velocity evolution of flowing granular materials through various channels in process engineering scenarios. Therefore, in general, we need a physically complete description of the flow dynamics without reduction of the information through the flow depth.

A first step towards modelling such complicated three-dimensional flows is to reduce it to two dimensions by first studying the inclined chute flow to obtain detailed information on velocities and build up of deposition geometries. Some basic two-dimensional channel flow experiments and their simulations with depth-averaged model equations are reported in (Pudasaini et al., 2007; Pudasaini and Kröner, 2008; Pudasaini and

Domnik, 2009). In this chapter, we are concerned with the development of a new theoretical model and simulation results in the first two regimes (starting and avalanching zone), which can also be extended in the third (depositional) regime (see Chapter 4 and Chapter 5).

Depending on the flow configuration, granular deformation may behave as an elastic, plastic, or viscous material, or the combination of them (Ancey, 2007; Pudasaini and Hutter, 2007; Fang et al., 2008; Forterre and Pouliquen, 2008). In this chapter, we will model the internal deformation as a simple viscoplastic material with a constant yield strength. Another important aspect of granular flow simulation is the basal boundary condition. In the classical depth-averaged modelling, explicit knowledge of the basal boundary is not needed, due to the depth-averaging. However, for the full dimensional treatment of the flow, we need to explicitly supply the bottom and the free surface boundary conditions, which automatically evolves in time and space. In the fluid-dynamic approach, the no-slip boundary condition, in which the slip velocity is set to zero, is widely and successfully used in many fluid simulations (Goldstein, 1938; Griebel et al., 1997; Hartel et al., 2000; Liu et al., 2004). However, it is observed in experiments and in the field that in rapid flow of granular material down the slopes, even the lowest particle layer in contact with the bottom boundary moves with a non-zero and non-trivial velocity (Massoudi and Phuoc, 2000; Kern et al., 2004; Pudasaini et al., 2005c; Platzer et al., 2007a,b; Pudasaini et al., 2007; Pudasaini and Hutter, 2007; Rognon et al., 2008).

The flow of granular material is not the only situation in which the no-slip condition is no longer appropriate. Also in polymer-processing, different attempts were made to formulate boundary conditions which allow partial slip at rigid boundaries (Schowalter, 1988; Leger et al., 1997). Generally, the no-slip condition works well for a single-component fluid, a wetted surface, and low levels of shear-stress (Granick et al., 2003). This is not the case, when non-absorbing polymers are dissolved in fluids of lower viscosity or in the case of granular flows, in which the interstitial fluid (e.g., air) between the particles can play the role of the fluid with low viscosity. Also, Navier was not satisfied with the no-slip boundary condition and proposed a slip-condition, in which a constant ς is introduced to describe the slip velocity u^b (Schowalter, 1988): $\varsigma u^b = \nu \left[\partial u_t/\partial n\right]^b$, where ν is the viscosity, u_t is the tangential fluid velocity, n is the normal of wall boundary directed into the fluid, and the ratio ν/ς has the dimension of a length. We want to continue with Navier's idea of a slip velocity at the wall boundary, but by relating the normal pressure to the shear-stress on the wall and so generating a slip velocity as observed in rapid granular flows. This is an entirely novel and innovative concept in rapid granular flows. The problem with Navier's slip is that it produces also a high shearing in fast but thin flows with low normal pressures on the wall, what is not observed in rapid granular flows (Pudasaini et al., 2005c, 2007). Therefore, we are using the Coulomb sliding law to relate the shear-stress T^b to the normal stress N^b at the bottom sliding surface (b): $T^b = \tan\delta N^b$, where δ is the bed friction hangle.

The Coulomb sliding law has successfully been used to model friction in many depth-averaged simulations of rapid granular flows (Savage and Hutter, 1989; Naaim et al.,

1997; Gray et al., 1999; Kerswell, 2005; Pudasaini et al., 2005c; Gruber and Bartelt, 2007; Pudasaini and Hutter, 2007; Pudasaini et al., 2008; Pudasaini and Kröner, 2008; Pudasaini and Domnik, 2009). Platzer et al. (2007b) showed that in dense snow avalanches, the relation between the normal and shear-stress can be described by a Coulomb friction law, in which cohesion has to be taken into account especially for wet snow avalanches. Uhland (1976) also utilised the Coulomb friction law to describe the slip velocity of a plastic melt flow through a pipe of circular cross-section. The stress-strain behaviour is described by a viscous power law. He assumed a steady, non-accelerated (no gravitational acceleration), one-dimensional (no radial component) flow. Based on these assumptions, which do not hold in general and in particular for rapid granular flows, he presented analytical solutions for the flow velocity and pressure. However, his velocity solution does not satisfy the continuity equation.

In this chapter, we will first develop a novel Coulomb frictional basal slip model, which uses the Coulomb friction law to model the interaction of the flow with the solid basal boundary surface. Formulation of the new pressure equation is presented in terms of finite differences for both pressure-independent and pressure-dependent basal slips. Afterwards, we study three different basal boundary conditions: no-slip, free-slip (pressure-independent), and the Coulomb-type slip (pressure-dependent) at the base. The observed differences in the flow dynamics for the no-slip and free-slip boundary conditions and the Coulomb sliding law are discussed in detail. The flow dynamics include the novel modelling and simulation of the evolution of the pressure and velocity field through the flow depth and the depth profile itself.

3.2 A viscoplastic granular flow model with slip

3.2.1 Field equations

The motion of granular material in a two-dimensional inclined rectangular channel (Fig. 3.1) is characterised by the pressure p and the velocity $\mathbf{u} = (u, w)^T$, with u the velocity component in downslope direction (x) and w the velocity component perpendicular to the channel surface (z). Incompressible flow is assumed, so density changes are negligible (Pudasaini and Hutter, 2007). The flow in a channel inclined by an angle ζ is described by a system of partial differential equations, representing the mass and momentum balances:

$$\operatorname{div} \mathbf{u} = 0, \tag{3.1}$$

$$\frac{d\mathbf{u}}{dt} = \operatorname{div} \boldsymbol{\sigma} + \mathbf{g}, \tag{3.2}$$

where $\boldsymbol{\sigma}$ is the Cauchy stress tensor normalised by density, $\mathbf{g}(\zeta) = (g \sin \zeta, -g \cos \zeta)^T$ is the gravitational acceleration with the gravity constant g, and d/dt is the material derivative.

We are considering a dry dense granular material, which is assumed to be described by a viscoplastic fluid (Bingham, 1922; Jop et al., 2006; Ancey, 2007; Balmforth and

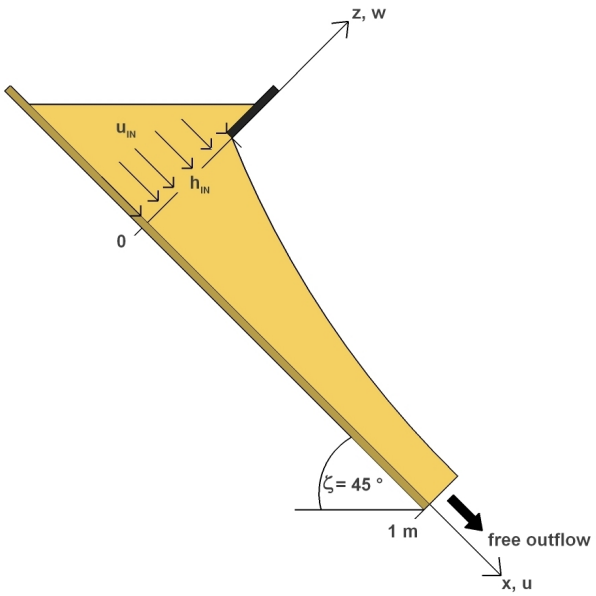

Figure 3.1: Side view of the inclined chute used for the simulation of rapid channel flow of granular material with free outflow. The material enters into the channel at $x = 0$ with an inlet height of $h_{\text{in}} = 0.15\,\text{m}$ and an average inlet velocity of $\bar{u}_{\text{in}} = 0.9\,\text{ms}^{-1}$. The computational domain is $[0, 1]$ m. The inlet velocity varies exponentially from the top of the opening gate to the bottom sliding surface and is indicated by the arrows at $x = 0$. ζ is the inclination angle of the channel.

Frigaard, 2007; Forterre and Pouliquen, 2008). The normalised stress tensor for a viscoplastic fluid can be written as

$$\boldsymbol{\sigma} = -p\mathbb{1} + 2\nu_{\text{eff}}\mathbf{D}, \tag{3.3}$$

where p is the normalised pressure, the strain rate tensor is given by the symmetric part of the velocity gradient, $\mathbf{D} = 1/2\left[(\nabla\mathbf{u}) + (\nabla\mathbf{u})^T\right]$, and ν_{eff} is the effective kinematic viscosity, which is defined by

$$\nu_{\text{eff}} = \nu + \frac{\tau_y}{||\mathbf{D}||}\left[1 - \exp\left(-m_y\,||\mathbf{D}||\right)\right]. \tag{3.4}$$

The effective kinematic viscosity depends on the kinematic viscosity ν, the yield stress τ_y (normalised by density), and the norm of the strain rate tensor, defined as $||\mathbf{D}|| = \sqrt{2\text{tr}\,(\mathbf{D}^2)}$. With the introduction of the exponential factor, $[1 - \exp\left(-m_y\,||\mathbf{D}||\right)]$, (3.4) holds uniformly in yielded and unyielded regions, and the transition between these regions is smoother for smaller exponents m_y (Papanastasiou, 1987). We used $m_y = 100$ for the simulations presented in Section 3.4. For $\tau_y = 0$, the effective viscosity equals the viscosity ν, and the material behaves as a Newtonian fluid. In this chapter, we assume a constant Bingham yield stress for simplicity. In applications, this simple viscoplastic rheology is often an adequate choice (Dent and Lang, 1982; Voight and Sousa, 1994; Whipple, 1997; Gauer et al., 2006). Then, shearing within the material is induced by friction at the rigid boundaries through the boundary conditions. If

shearing which results from direct contacts between the granular particles becomes considerable, the assumption of a constant yield stress could be too simple and a pressure-dependent yield stress should have been considered like in (Moriguchi et al., 2005; Jop et al., 2006). This will be presented in Chapter 4.

With the notations

$$F = -\partial_x\left(u^2\right) - \partial_z\left(uw\right) + 2\partial_x\left(\nu_{\text{eff}}\partial_x u\right) + \partial_z\left[\nu_{\text{eff}}\left(\partial_z u + \partial_x w\right)\right] + g\sin(\zeta), \quad (3.5)$$

$$G = -\partial_z\left(w^2\right) - \partial_x\left(uw\right) + 2\partial_z\left(\nu_{\text{eff}}\partial_z w\right) + \partial_x\left[\nu_{\text{eff}}\left(\partial_z u + \partial_x w\right)\right] - g\cos(\zeta), \quad (3.6)$$

the momentum equation (3.2) can now be expressed as

$$\partial_t u = F - \partial_x p, \quad (3.7)$$

$$\partial_t w = G - \partial_z p. \quad (3.8)$$

Equations (3.7) and (3.8) are integrated numerically to compute the velocities u and w. To calculate the pressure, a Poisson equation for the pressure is derived by applying ∂_x or ∂_z on the x or z-momentum-conservation ((3.7) and (3.8)), adding both resulting equations, and using the continuity equation (3.1) to yield:

$$\Delta p = \partial_x^2 p + \partial_z^2 p = \partial_x F + \partial_z G. \quad (3.9)$$

Equation (3.7), (3.8), and (3.9) require appropriate boundary conditions for the velocities at the free surface and basal surface, which is one of the main focuses of this chapter.

3.2.2 Velocity boundary condition at the base

In the following, we consider the friction induced by the movement of granular material on sliding planes, which can be at rigid boundaries with an inner normal vector $\mathbf{n}$ and a tangential vector $\mathbf{t}$. In rapid flows of granular material down the slopes, even the lowest particle layer in contact with the bottom boundary moves with a non-zero and non-trivial velocity. Therefore, the generally used no-slip boundary condition does not represent the flow physics. A non-zero slip velocity is determined by the frictional strength, which depends on the load the material exerts on the rigid boundary. So, it is natural to relate the shear-stress $T^b = \boldsymbol{\sigma}^b\mathbf{n}\cdot\mathbf{t}$ to the normal pressure $N^b = -\boldsymbol{\sigma}^b\mathbf{n}\cdot\mathbf{n}$ at the sliding surface (b). This can be achieved by using the Coulomb sliding law, which was already successfully used in simulations of rapid granular flows:

$$T^b = \frac{u^b}{|u^b|}\tan\delta N^b. \quad (3.10)$$

This relation asserts that a material yields plastically if the shear-stress attains the critical value given by (3.10). The tangent of the bed friction angle δ defines the proportionality constant and higher values of δ go along with a higher shearing and, therefore, with a higher frictional force at the rigid boundary. To guarantee that the frictional force is always opposite to the direction of motion, the factor $u^b/\left|u^b\right|$ is

introduced. The flowing granular material does not penetrate through the boundary, so $\mathbf{n}\cdot\mathbf{u}^b = 0$ and also $[(\mathbf{t}\cdot\nabla)(\mathbf{n}\cdot\mathbf{u})]^b = 0$. Therefore, from (3.3) and with a bit of algebra*, the normal and shear stresses at the bottom are given by $N^b = p^b + 2\nu^b_{\text{eff}}[(\mathbf{t}\cdot\nabla)(\mathbf{t}\cdot\mathbf{u})]^b$ and $T^b = \nu^b_{\text{eff}}[(\mathbf{n}\cdot\nabla)(\mathbf{t}\cdot\mathbf{u})]^b$. This leads to a pressure and rate-dependent Coulomb-viscoplastic sliding law expressed in terms of the tangential velocity and the pressure at the boundary

$$[(\mathbf{n}\cdot\nabla)(\mathbf{t}\cdot\mathbf{u})]^b - 2c^{\text{F}}[(\mathbf{t}\cdot\nabla)(\mathbf{t}\cdot\mathbf{u})]^b = \frac{c^{\text{F}}}{\nu^b_{\text{eff}}}p^b. \tag{3.11}$$

Here the 'friction factor', c^{F}, is defined by

$$c^{\text{F}} = \begin{cases} \dfrac{u^b}{|u^b|}\tan\delta, & u^b \neq 0, \\ 0, & u^b = 0. \end{cases} \tag{3.12}$$

The ratio between the grain friction, c^{F}, and the viscous friction is called the 'effective friction ratio':

$$F^r_e = \frac{c^{\text{F}}}{\nu^b_{\text{eff}}}\,. \tag{3.13}$$

The pressure and rate-dependent Coulomb-viscoplastic sliding law, (3.11), dynamically and automatically defines the bottom boundary velocity $[\mathbf{t}\cdot\mathbf{u}]^b$. Note that in the classical, depth-averaged plastic flow models for granular material, N^b is the overburden pressure (material normal load), i.e., the hydrostatic pressure, which is independent of the flow dynamics. Then, the Coulomb sliding law, (3.10), does not include any dynamic information about the flow and deformation, such as the velocity and pressure. So, (3.10) is then a rate-independent plastic law.

It is important to observe that if the Coulomb friction coefficient c^{F} equals zero ($\delta = 0$ or no material motion), then no grain friction exists, and (3.11) reduces to the well-known free-slip condition $[(\mathbf{n}\cdot\nabla)(\mathbf{t}\cdot\mathbf{u})]^b = 0$, for which no friction at the boundary is present and, therefore, the basal shear-stress equals zero.

For negligible granular friction or for very high effective viscosity (in both cases $F^r_e \approx 0$), the pressure dependency is lost, and (3.11) becomes

$$\left[\frac{(\mathbf{n}\cdot\nabla)(\mathbf{t}\cdot\mathbf{u})}{(\mathbf{t}\cdot\nabla)(\mathbf{t}\cdot\mathbf{u})}\right]^b = 2c^{\text{F}}. \tag{3.14}$$

So, the friction factor in terms of the bed friction angle defines the ratio between the normal and tangential derivative of the tangential velocity at the bottom. In the following, we will treat the more general case where the bottom pressure is not negligible (i.e., $F^r_e \neq 0$).

We are considering the motion of granular material in a narrow rectangular inclined channel with the main flow direction parallel to the x-axis. The main shearing occurs at the bottom boundary with the basal normal vector parallel to the z-direction

*This is explicitly calculated in Appendix A.

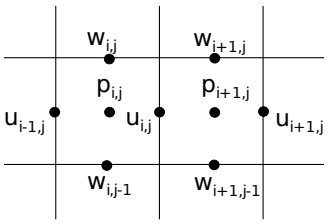

Figure 3.2: Staggered grid. The pressure p is located in the cell centres and the $x(z)$-velocity u (w) in the midpoint of the vertical (horizontal) cell edges.

$\left(\mathbf{n} = (0,1)^T,\ \mathbf{t} = (1,0)^T\right)$. The shearing at the sidewalls has only a marginal influence on the granular flow and will be neglected (Pudasaini et al., 2007; Pudasaini and Kröner, 2008). Then, the Coulomb shear-stress at the bottom, (3.10), can simply be written as

$$T^b = c^{\mathrm{F}} N^b \quad \text{with} \quad N^b = p^b + 2\nu_{\mathrm{eff}}^b \left[\partial_x u\right]^b . \tag{3.15}$$

If the strain rate approaches zero, the shear-stress is given by $T^b = c^{\mathrm{F}} p^b$. Hence, the Coulomb-viscoplastic friction law defines a yield criterion with a pressure-dependent yield stress. This describes the frictional nature of the interaction of the granular material with the rigid boundary. An increase in $\partial_x u$ results in a higher bottom normal stress and, consequently, in a higher frictional bottom shear-stress (3.15). This is different for shear-stresses within the material, which will decrease due to a decline of the effective Bingham viscosity (3.4).

For a rectangular inclined channel, the Coulomb-viscoplastic sliding law, (3.11), is given by

$$\left[\partial_z u\right]^b - 2c^{\mathrm{F}} \left[\partial_x u\right]^b = \frac{c^{\mathrm{F}}}{\nu_{\mathrm{eff}}^b} p^b. \tag{3.16}$$

Equation (3.16) is an equation for pressure in terms of the velocity gradients or vice versa. In the following, (3.16) will be used as pressure-dependent velocity boundary condition at the sliding surface. Note that with (3.16) the bottom shear-stress depends on the normal stress contrary to Navier's slip and the no-slip boundary condition, in which it depends only on the velocity near the sliding surface.

3.3 Numerical method

3.3.1 Discretisation and free surface treatment

In order to compute the velocities and the pressure from equations (3.7), (3.8), and (3.9), an appropriate discretisation has to be carried out. Our numerical method is based on *NaSt2D* (Griebel et al., 1997), a computer code using the finite-volume method for the simulation of incompressible Newtonian fluids. Following (Harlow and Welch, 1965; Griebel et al., 1997), we introduce a staggered grid (see, Fig. 3.2), in which the velocities and the pressure are not located at the same grid points to avoid possible pressure oscillations. The pressure p is located in the cell centres ('p-grid'), the x-velocity u in the midpoint of the vertical cell edges ('u-grid') and the z-velocity

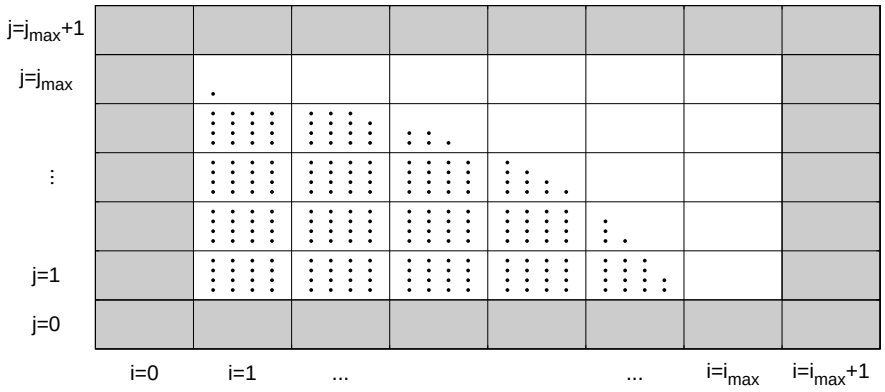

Figure 3.3: Flow domain including marker particles and boundary strip. Cells in the boundary strip are called boundary cells.

w in the midpoint of the horizontal cell edges ('w-grid'). To describe the boundary conditions, a boundary strip is added at $i = 0$, $i = i_{max} + 1$, $j = 0$ and $j = j_{max} + 1$ (Fig. 3.3). Therefore, the whole grid consists of $(i_{max} + 2) \cdot (j_{max} + 2)$ cells $C_{i,j}$ with $i \in [0, i_{max} + 1]$ and $j \in [0, j_{max} + 1]$. The length of one single cell is $dx(dz)$ in $x(z)$-direction.

The Poisson equation (3.9) is discretised on the p-grid, and the $x(z)$-momentum equations (3.7), (3.8) are discretised on the $u(w)$-grid. The spatial derivatives are replaced by centred differences except for the convective terms, which are discretised by using a mixture of central differences and the donor-cell discretisation. The Bingham terms (terms containing τ_y) in the momentum equations cannot be discretised straightforward, as they contain the norm of the strain rate tensor. In Appendix B we propose a discretisation approach which uses the momentum equations in conservative form. It yields the same numerical scheme as for a Newtonian fluid, hence no additional velocities, which are not available near free surfaces or boundaries, are required and more stable results are observed. To discretise the time derivatives, we use first-order difference quotients. The complete discretisations of the momentum equations are presented explicitly in Appendix B.

To simulate and visualise the rapid free surface flow of frictional granular material, the marker-and-cell (MAC) method is applied, in which marker-particles are used to determine whether a cell contains 'fluid' or not (see, Fig. 3.3), (Harlow and Welch, 1965; Tomé et al., 2007; Muravleva, 2009).

The originality of our approach is also due to the fact that we numerically implement the Coulomb-viscoplastic sliding law, which is presented in Section 3.3.3.

Kröner (2013) presents an alternative full dimensional continuum model and its simulations describing rapid granular flows and avalanches. The model employs a simple Coulomb sliding law, and the model equations are solved by using a finite volume method together with OpenFOAM®, which is an open source computational fluid dynamics (CFD) software package. OpenFOAM® uses the volume of fluid method

(VOF) (Hirt and Nichols, 1981) to model the free surface.

3.3.2 Pressure calculation for pressure-independent basal slip

If a pressure-independent friction law such as the no-slip or free-slip condition is used, the velocity boundary conditions are known before calculating the pressure. In case of the no-slip condition, the tangential velocities should vanish at the boundary, e.g., for the bottom boundary at $z = 0$ the condition reads: $(u_{i,1} + u_{i,0})/2 = 0$ (by using linear interpolation). This is achieved by setting $u_{i,0} = -u_{i,1}$. The free-slip condition requires the normal derivative of the velocity component tangential to the boundary to vanish. For example, the free-slip boundary condition can be written as, $(u_{i,1} - u_{i,0})/dz = 0$, for the bottom boundary at $z = 0$ by using central differences. This leads to the velocity boundary condition $u_{i,0} = u_{i,1}$. Together with the condition for the normal velocities, $w_{i,0} = 0$, which asserts that the material cannot penetrate through a rigid boundary, the right hand side of the Poisson equation, (3.9), is fixed for a given velocity field. Using central finite differences, (3.9) results in the discrete Poisson equation for the pressure p:

$$\begin{aligned} \frac{p_{i+1,j} - 2p_{i,j} + p_{i-1,j}}{dx^2} + \frac{p_{i,j+1} - 2p_{i,j} + p_{i,j-1}}{dz^2} \\ = \left(\frac{F_{i,j} - F_{i-1,j}}{dx} + \frac{G_{i,j} - G_{i,j-1}}{dz} \right). \end{aligned} \tag{3.17}$$

Equation (3.17) can also be written as a system of N_I linear equations,

$$\mathbf{M}\mathbf{p} = \mathbf{b}_p, \tag{3.18}$$

with $\mathbf{M} \in \mathbb{R}^{N_I \times N_I}$ and $\mathbf{p}, \mathbf{b}_p \in \mathbb{R}^{N_I}$, where N_I is given by the number of inner 'fluid' cells. The matrix $\mathbf{M}$ depends only on the grid refinement. The right-hand-side of (3.18), $\mathbf{b}_p$, contains the spatial derivatives of the convective, diffusive and gravitational forces. Note that $\mathbf{M}$ is symmetric and negative definite and the system of linear equations can be solved for the pressure, e.g., with the successive overrelaxation (SOR) method (Young, 2003).

After the pressure is calculated with the discrete Poisson equation, (3.18), the momentum equations ((3.7), (3.8)) are used to calculate the velocities for the next time step.

3.3.3 Pressure calculation for pressure-dependent basal slip

If a pressure-dependent friction law, i.e., slip velocity at the base, is used for the rigid boundaries, (3.18) cannot be used for the pressure computation, because the vector $\mathbf{b}_p$ depends on the velocity boundary values, consequently, also on the pressure. Therefore, a pressure equation has to be formulated, which guarantees that the pressure satisfies both the Poisson equation and the pressure-dependent friction law at the bed. For this reason, here we develop a completely new approach, which is a fundamental contribution and an advancement in granular flow simulations from a computational point of view with ample applications in geophysical and industrial mass flows.

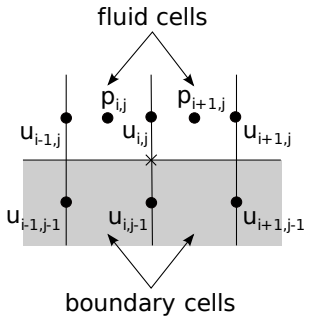

Figure 3.4: Discretisation points (cross) of Coulomb sliding law. If the cells $C_{i,j}$ and $C_{i+1,j}$ are 'fluid' cells and the cells $C_{i,j-1}$ and $C_{i+1,j-1}$ are boundary cells, the cell $C_{i,j}$ is called a Coulomb cell.

Coulomb sliding law

With the following discretisations at the lower right corner of a cell $C_{i,j}$ adjacent to a boundary cell $C_{i,j-1}$ (see, Fig. 3.4)

$$c^{\mathrm{F}} \equiv \begin{cases} \dfrac{u_{i,j}}{|u_{i,j}|} \tan\delta, & u_{i,j} \neq 0, \\ 0, & u_{i,j} = 0, \end{cases} \tag{3.19}$$

$$p^b \equiv \frac{1}{2}\left(p_{i,j} + p_{i+1,j}\right), \tag{3.20}$$

$$\left[\partial_z u\right]^b \equiv \frac{1}{dz}\left(u_{i,j} - u^b_{i,j-1}\right), \tag{3.21}$$

$$\left[\partial_x u\right]^b \equiv \frac{1}{4dx}\left(u_{i+1,j} + u^b_{i+1,j-1} - u_{i-1,j} - u^b_{i-1,j-1}\right), \tag{3.22}$$

the Coulomb-viscoplastic sliding law, (3.16), can be expressed in terms of the bottom boundary values $u^b_{i,j}$

$$\begin{aligned} u^b_{i,j-1} + c^u_{i,j}\left(u^b_{i+1,j-1} - u^b_{i-1,j-1}\right) = u_{i,j} - c^u_{i,j}\left(u_{i+1,j} - u_{i-1,j}\right) - \\ c^p_{i,j}\left(p_{i,j} + p_{i+1,j}\right), \\ \text{with} \quad c^u_{i,j} = \frac{1}{2}\frac{dz}{dx} c^{\mathrm{F}}_{i,j} \quad \text{and} \quad c^p_{i,j} = \frac{dz}{2\nu^{i,j}_{\mathrm{eff}}} c^{\mathrm{F}}_{i,j}. \end{aligned} \tag{3.23}$$

Note that the discretisation of c^{F} at $z = dz/2$, instead at the bottom ($z = 0$), is not critical, because only the sign of the tangential velocity is required, which is not expected to change within a half cell height. The pressure at the bottom is approximated by the next available pressure values. To compute the velocity derivatives, central differences are used, and for $\left[\partial_x u\right]^b$ an additional averaging is performed as mentioned in (3.22).

The Coulomb sliding law (3.23) can only be used to compute the bottom boundary velocity $u^b_{i,j-1}$ for cell $C_{i,j}$ if both cells $C_{i,j-1}$ and $C_{i+1,j-1}$ are boundary cells and both cell $C_{i,j}$ and also its right neighbouring cell $C_{i+1,j}$ contain 'fluid'. Then, the cell $C_{i,j}$ is called a Coulomb cell, Fig. 3.4. Therefore, (3.23) requires boundary values near the

free surface, which are given by the traction free condition of the free surface.

Equation (3.23) can be written as a system of N_c linear equations

$$\mathbf{A}\mathbf{u}^b = \mathbf{b}_c - \mathbf{B}\mathbf{p}, \tag{3.24}$$

with $\mathbf{A} \in \mathbb{R}^{N_c \times N_c}$, $\mathbf{B} \in \mathbb{R}^{N_c \times N_I}$, $\mathbf{b}_c$ and $\mathbf{u}^b \in \mathbb{R}^{N_c}$, where N_c is given by the number of Coulomb cells. The matrix $\mathbf{A}$ is invertible, therefore, the velocity boundary values can be calculated with (3.24) after the pressure computation. For $c^{\mathrm{F}} = 0$ (no grain friction), the matrix $\mathbf{A}$ equals the identity matrix, and for $c^{\mathrm{F}} \neq 0$, its off-diagonal elements are proportional to c^u. The elements of $\mathbf{B}$, with which the pressure is multiplied, are given by c^p. Therefore, the increase of both the bottom pressure and the effective friction ratio leads to a decrease of the bottom velocity for an accelerating flow. This is characteristic for the flow of frictional granular material.

Pressure equation

The pressure must satisfy both the Poisson equation (3.18) and the friction law (3.24), which both depend on the bottom velocities. Therefore, a central and novel idea is that these equations can be combined into a single pressure equation, which is independent of the bottom velocity.

The inhomogeneity $\mathbf{b}_p$ of the Poisson equation (3.18) contains F and G (compare with (3.17)), which are given by (3.5) and (3.6) and depend on the boundary velocities. The knowledge of the bottom velocity is necessary for the computation of the derivative $\partial_z^2 u$ in F, which can be expressed for a cell $C_{i,j}$ in terms of the bottom boundary velocity $u^b_{i,j-1}$ (Appendix B):

$$F_{i,j} = f^{(1)}_{i,j} u^b_{i,j-1} + f^{(2)}_{i,j}, \tag{3.25}$$

whereas $f^{(1)}_{i,j}$ and $f^{(2)}_{i,j}$ depend on the discretisation and can be calculated without the knowledge of the bottom boundary velocity. With (3.17) and (3.25), $\mathbf{b}_p$ can now directly be related to the bottom boundary velocity:

$$\mathbf{b}_p = \mathbf{Q}\mathbf{u}^b + \mathbf{q}_p, \tag{3.26}$$

with $\mathbf{Q} \in \mathbb{R}^{N_I \times N_c}$ and $\mathbf{q}_p \in \mathbb{R}^{N_I}$. The vector $\mathbf{q}_p$ contains the boundary velocity-independent terms of the spatial derivatives of the convective and diffusive forces. The boundary velocity-dependent terms are included in $\mathbf{Q}\mathbf{u}^b$. Hence, the Poisson equation (3.18) can be written explicitly in terms of the bottom boundary velocity

$$\mathbf{M}\mathbf{p} = \mathbf{Q}\mathbf{u}^b + \mathbf{q}_p. \tag{3.27}$$

Combining (3.27) with (3.24) gives an equation for the pressure, which unlike (3.18) no longer requires the knowledge of bottom boundary velocities (this is a great advantage):

$$\underbrace{\left(\mathbf{M} + \mathbf{Q}\mathbf{A}^{-1}\mathbf{B}\right)}_{\mathbf{L}} \mathbf{p} = \underbrace{\mathbf{Q}\mathbf{A}^{-1}\mathbf{b}_c + \mathbf{q}_p}_{\mathbf{b}_L}, \tag{3.28}$$

where the sparse pressure matrix $\mathbf{L} \in \mathbb{R}^{N_I \times N_I}$ and the vector $\mathbf{b}_L \in \mathbb{R}^{N_I}$ are defined. Note that, in general, the pressure matrix $\mathbf{L}$ is not symmetric, because $\mathbf{Q}\mathbf{A}^{-1}\mathbf{B}$ is not symmetric. The pressure matrix $\mathbf{L}$ depends on the Coulomb friction coefficient and the grid refinement. The right-hand-side of (3.28), $\mathbf{b}_L$, contains, on the one hand, the boundary velocity-independent terms of the spatial derivatives of the convective and diffusive forces and, on the other hand, velocity-dependent terms, which originate from the Coulomb sliding law, (3.24), and hence are also affected by the Coulomb friction coefficient.

For a vanishing Coulomb friction coefficient, $c^{\mathrm{F}} = 0$, (3.28) reduces to the Poisson equation, (3.18), because $\mathbf{A} = \mathbb{1}$, $\mathbf{B} = \mathbf{0}$ and $\mathbf{b}_c = \mathbf{u}^b$ according to (3.24). In this case, the velocity boundary condition equals the one for the free-slip boundary condition. For the more general case, $c^{\mathrm{F}} \neq 0$, the bottom shear-stress depends on the bottom normal stress, i.e., the bottom pressure and derivative of the tangential velocity in downslope direction, but not on the velocity itself. Therefore, the new Coulomb-viscoplastic sliding law, (3.16), differs substantially from the no-slip boundary condition, for which the bottom shear-stress is velocity-dependent.

The Coulomb friction law is implemented by solving (3.28) for the pressure and obtaining the bottom boundary velocities according to (3.24) afterwards. So, we simultaneously have both the pressure and the slip-velocity at the bottom. It is worth mentioning that combination of the viscoplastic and Coulomb law made it possible to obtain (analytical or theoretical) expressions for both the pressure and the basal-slip velocity. For pressure-independent no-slip and free-slip boundary conditions, the Poisson equation (3.18) is used instead of (3.28). In the following, benchmark simulations are performed in which no-slip, free-slip, and Coulomb-slip are implemented and analysed. These simulations demonstrate the applicability of the new Coulomb-viscoplastic rheology and the performance of our new numerical method.

3.4 Granular flow simulations for different basal friction laws

3.4.1 Flow configuration and parameters

Here, we simulate the fully two-dimensional (non depth-averaged) rapid viscoplastic granular flow down an inclined channel with an open end for different basal friction laws. The channel is 1 m long, has an inclination of $\zeta = 45°$, and it is continuously fed from a silo, see Fig. 3.1. The inlet height is $h_{\mathrm{in}} = 0.15\,\mathrm{m}$, and the mean inlet velocity is $\bar{u}_{\mathrm{in}} = 0.9\,\mathrm{ms}^{-1}$. These flow configurations are similar to those used in (Pudasaini et al., 2007; Pudasaini and Kröner, 2008; Pudasaini and Domnik, 2009). To achieve realistic inflow conditions, the inflow velocity is varied exponentially with the flow depth: $u_{\mathrm{in}}(z) = \kappa\left[\alpha - \exp(\beta z)\right]$ with $\alpha = 1000$, $\beta = 45.9$, and $\kappa = 1.05 \times 10^{-3}$ (with appropriate dimensions) so that $\bar{u}_{\mathrm{in}} = 0.9\,\mathrm{ms}^{-1}$. With this choice, the inlet velocity changes only slightly with depth until z is close to the inlet height, where u_{in} drops to almost zero, because of influence of the upper tip of the inlet gate. This

is an observable phenomenon in silo-discharge. Note that the variation of the inlet velocity along the flow depth has only a slight impact on the overall flow characteristics, because immediately after the material has entered the channel, it is subject to strong deformations. Setting the inlet velocity at the upper tip of the inlet gate to zero mainly affects the formation of the free surface in the vicinity of the flow front. The dynamic viscosity of mass flows events, like natural rock avalanches, debris avalanches and debris flows, can range from 0.01 to 20 Pa s or even more (Takahashi, 1991; Iverson, 1997; Takahashi, 2007). In the simulation, we use a value of 15 Pa s, which corresponds to a kinematic viscosity of $\nu = 0.01\,\mathrm{m^2 s^{-1}}$ for a bulk density of $\rho = 1500\,\mathrm{kg\,m^{-3}}$. The estimated value of the lower limit of the yield stress for a rock avalanche is about 15 kPa. This holds for an assumed flow depth of about 5 m, a true rock density of about $3000\,\mathrm{kg\,m^{-3}}$, and a friction coefficient about 0.7 (Dade and Huppert, 1998; Davies et al., 2010). In our numerical simulations, the representative flow depth (along the channel) is 0.065 m, and the friction coefficient is about 0.5 (for a basal friction angle of 25°). Together with the assumed granular bulk density, the yield stress can be estimated to 60 Pa, as used in the present simulation. However, here these numbers are taken mainly for the simulation purpose. So, depending on specific flow situation and the materials in use, the actual values of these physical parameters may deviate substantially from those used here. To study the role of the Coulomb friction and other basal sliding laws numerically, we present results for quasi-steady-state and complete transient channel flows. The physical variables are non-dimensionalised by using the scalings (following Pudasaini and Hutter (2007))

$$(x, z, t, u, p) = \left(L\hat{x}, H\hat{z}, T\hat{t}, U\hat{u}, P\hat{p}\right), \tag{3.29}$$

where L is a characteristic length, and H is a characteristic depth. The characteristic time is given by $T = \sqrt{L/g}$, the characteristic velocity can be estimated by $U = \sqrt{gL}$, and the characteristic pressure is evaluated by $P = \rho g H$. The hats represent non-dimensional variables. Here, the channel length is chosen as characteristic length, $L = 1\,\mathrm{m}$, and the inlet height is taken as characteristic depth, $H = 0.15\,\mathrm{m}$.

3.4.2 Channel flow simulations

Quasi-steady-state flow

In the following, the simulated flows are considered at an instant of time, when the flow is in a quasi-steady-state. Figure 3.5(a) and Fig. 3.5(b) show that for all considered friction laws, the quasi-steady-state is attained well for $\hat{t} > 2$. For the no-slip simulation, the chosen time is $\hat{t}^{\mathrm{sim}} = 2.5$ and for the other simulations (free-slip and Coulomb friction laws), $\hat{t}^{\mathrm{sim}} = 2.2$.

Figure 3.6 shows the simulated flow depth (in background grey) and velocity vectors throughout the channel for three different basal friction laws. For the flow obeying the no-slip boundary condition (panel a), a strong shearing along the whole channel is observed contrary to the flow obeying the free-slip condition (panel b), which does not show a structured evolution of the velocity along depth but the velocity profile is uniform over depth. The simulation using the pressure-dependent Coulomb sliding law

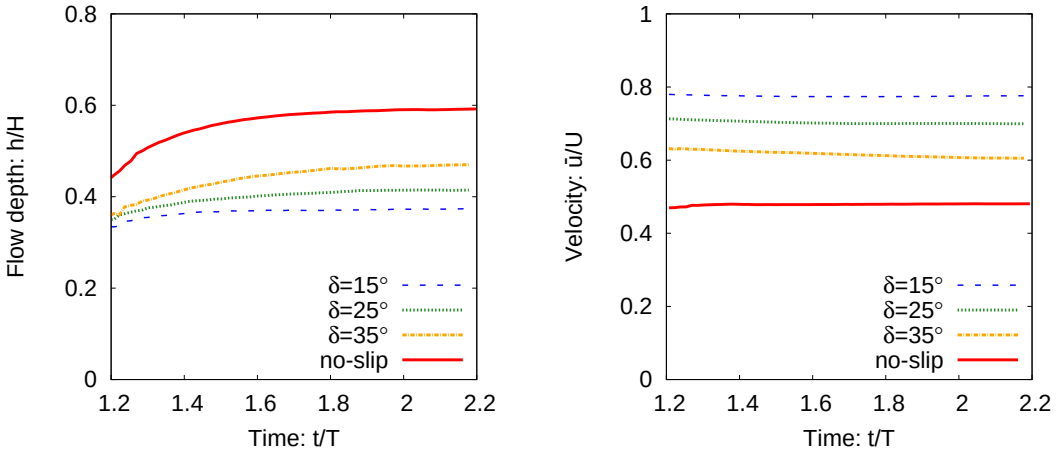

(a) Flow depth.

(b) Mean velocity.

Figure 3.5: Time dependence of characteristic flow quantities: depth (a) and mean velocity (b) (considered at $\hat{x} = 0.5$) for different basal friction laws.

(panel c) differs substantially from both the no-slip and the free-slip simulations. It generates a non-zero slip velocity at the bottom, which increases along the downslope channel position, and produces a clear and strong shear profile through a substantial flow depth in the vicinity of the bottom. However, the shear rate is decreased and is close to zero in the upper half flow-depth and in the vicinity of the free surface.

These simulation results reveal that although the same internal viscoplastic flow rheologies, traction-free conditions, and inlet outlet conditions are applied for all three types of simulations, the results and flow patterns (flow depth, velocity and pressure patterns; are discussed in more detail later) are fundamentally different in the three panels. This means that the bottom boundary condition is an important mechanism to control and describe the flow dynamics in rapid granular flows in steep channels. Experiments in rapid granular flows in inclined chutes and channels show that the material slips along the channel (so, panel (a) is not appropriate there) and shears mainly in the vicinity of the bottom, whereas the shear rate adjacent to the free surface is low (Kern et al., 2004; Pudasaini et al., 2005c, 2007; Pudasaini and Hutter, 2007; Rognon et al., 2008). These typical characteristics of rapid granular flows are illustrated by panel (c). So, for such flow configuration, panel (a) and (b) are not applicable, at least in the far downstream. However, we continue our analysis also with the no-slip boundary condition (panel (a)), because locally granular flow can behave as a no-slip material in the vicinity of the silo gate, in strong flow obstacle interactions, in the deposition, in situations when the channel inclination is at or below the basal friction angle, and when the basal surface is rough (e.g., glued with the same material). In the later cases, the flow sticks at the basal surface and the flow is slow or creeping. Panel b of Fig. 3.6 indicates that free-slip is not a right candidate as there is no velocity structure and the velocity magnitude is also much higher as compared to panels a and c.

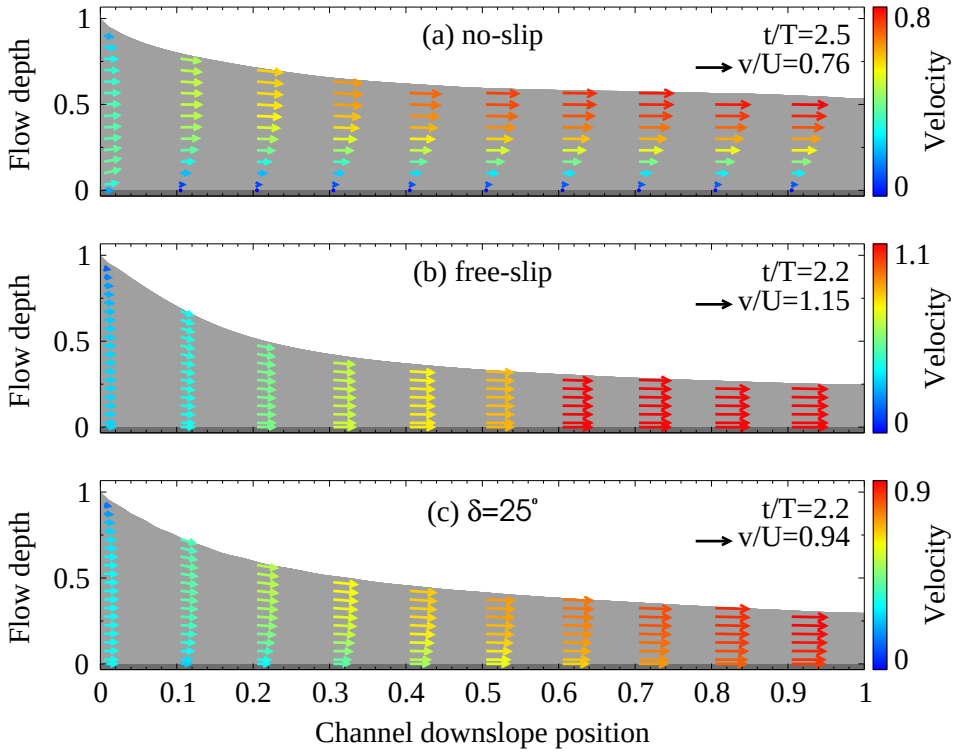

Figure 3.6: Full two-dimensional velocity vectors at different channel positions for three different basal friction laws: no-slip (a), free-slip (b), and Coulomb friction law (c) with $\delta = 25°$. The flow enters the channel at $x = 0$ with an average velocity of $\bar{u}_{\text{in}}/U = 0.29$. The background grey colour represents the flow depth. All quantities are dimensionless.

The tangential surface and bottom velocities behave completely differently under the change of friction law, Fig. 3.7. For the Coulomb friction law (with $\delta = 25°$), the bottom velocity is non-zero (dotted green line), contrary to the same with the no-slip boundary condition (solid red line), and illustrates a quick decrease near the silo inlet followed by a quick increase along the channel. The decline in the bottom velocity in the vicinity of the inlet ($\hat{x} < 0.1$) reveals the high bottom pressure in this region (see Fig. 3.11(a)). The free surface velocities (dashed green and dot-dashed red line) increases rapidly in the beginning ($\hat{x} < 0.3$) for both friction laws, Fig. 3.7. However, the no-slip boundary condition generates a very strong, velocity-dependent friction, which afterwards almost compensates the gravitational acceleration, and hence the free surface velocity grows very slowly (dot-dashed red line).

The different friction laws result not only in different shear profiles but also in different mean flow velocities and heights (depths), which are shown in Fig. 3.8 and Fig. 3.9, respectively. The mean flow velocity strongly depends on the frictional resistance at the bottom, e.g., for the Coulomb friction with $\delta = 25°$, the mean velocity at the end of the channel is roughly double the one for the no-slip boundary condition. Simulations using the Coulomb sliding law generate mean velocities which are controlled by the bed friction angle and are always higher than the mean velocities induced by the no-slip boundary condition. This also affects the flow heights (Fig. 3.9), which are inversely correlated to the velocity by the continuity condition. The increase of

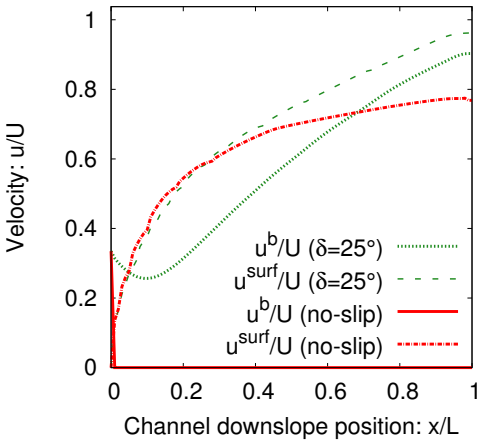

Figure 3.7: Dimensionless surface and bottom velocities, u^{surf}/U and u^{b}/U, along the channel for no-slip and Coulomb friction law with $\delta = 25°$.

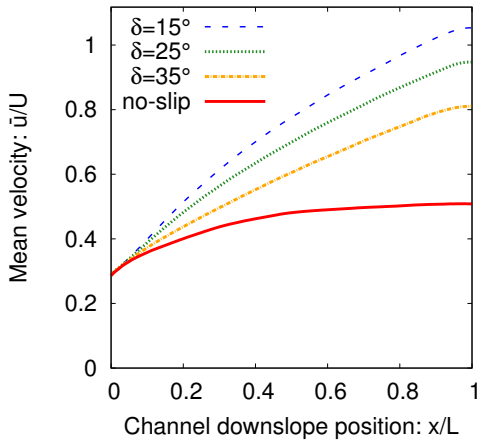

Figure 3.8: Dimensionless mean velocity $\bar{u}/U$ along the channel for different basal friction laws.

flow depth averaged along the channel with length L, $\mathcal{H} = 1/L \int_0^L h dx$, with rising bed friction angle is shown in Fig. 3.10. It can be described by a simple power law function, $\mathcal{H}(\tan\delta)/H = a\,(\tan\delta)^n + b$, with $a = 0.19$, $b = 0.38$ and $n = 1.3$. This demonstrates that the choice of the boundary condition and the friction coefficient substantially influences the flow dynamics. However, the rate at which the mean velocity increases and depth decreases depends on the ratio of the driving force (gravity) to the resisting forces (e.g., bottom friction). If the bottom friction increases with the flow velocity, the (mean) velocity will saturate at some distance from the silo inlet. This is observed for no-slip flows. We are considering "dry" friction which does not depend on the velocity. A velocity-dependence can be included in the bottom friction

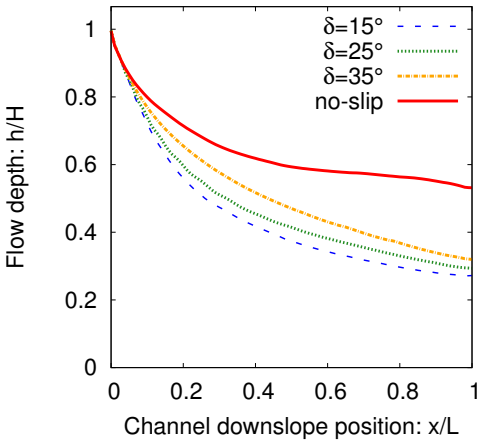

Figure 3.9: Dimensionless flow depth h/H along the channel for different basal friction laws.

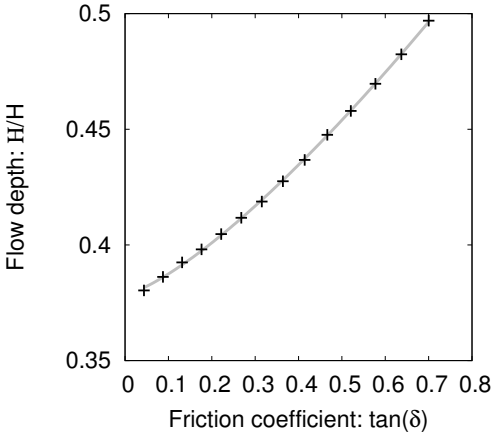

Figure 3.10: Dimensionless flow depth $\mathcal{H}/H$ (averaged through the channel length) for different friction coefficients $\tan\delta$. The flow depths simulated with the Coulomb-viscoplastic sliding model are illustrated by plus marks. The grey line corresponds to a power law function, $\mathcal{H}(\tan\delta)/H = a\,(\tan\delta)^n + b$, with $a = 0.19$, $b = 0.38$ and $n = 1.3$.

by adding the term $c_u u^2$ to the right-hand side of (3.10) (Pudasaini and Hutter, 2007). This becomes eventually important in describing snow avalanches which may show a uniform flow (constant flow height) over a wide range of slope angles (Kern et al., 2004; Rognon et al., 2008; Fischer et al., 2012).

Figure 3.11 presents the pressure fields for the Coulomb friction law with $\delta = 25°$ and the no-slip boundary condition. Although both friction laws show completely different behaviour, for both the pressure exhibits a layered structure along the channel, which originates from the depth-dependence of the pressure and the flow dynamics, see (3.9).

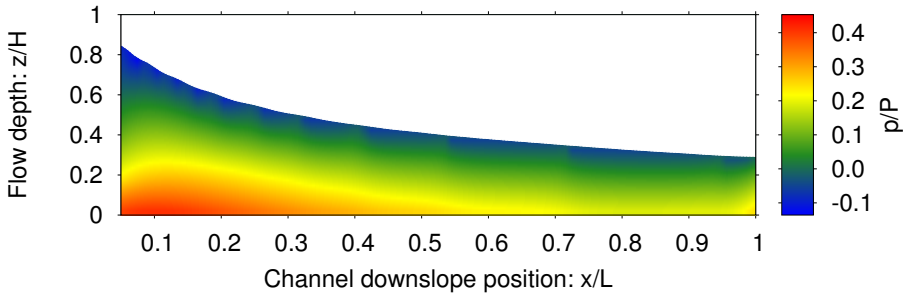

(a) Coulomb friction law with $\delta = 25°$.

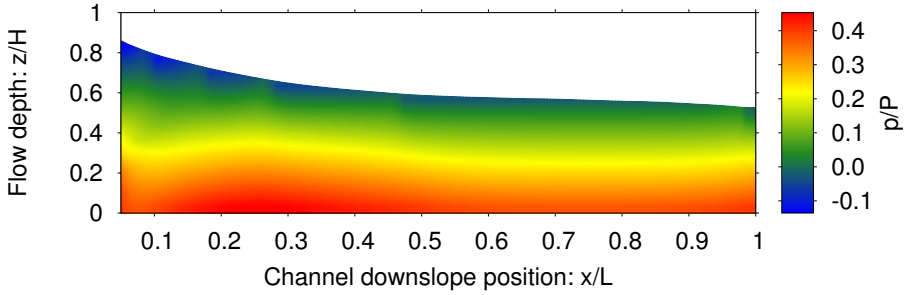

(b) No-slip boundary condition.

Figure 3.11: Dimensionless pressure field p/P for Coulomb friction law with $\delta = 25°$ (a), and no-slip boundary condition (b).

In case of the Coulomb boundary condition, the pressure first increases along x, due to the considerable fall in flow depth, which goes along with a compressional mode of the material near the silo inlet. Later on, the pressure decreases along the channel, because the gravitational acceleration causes a dilatational downslope motion. The latter is not observed for the no-slip boundary condition, because here the frictional resistance at the bottom depends on the tangential velocity and opposes the gravitational acceleration, leading to an almost uniform flow in x-direction (i.e., $\partial_x \bar{u}$ is small), compare Fig. 3.8. So, with no-slip, pressure does not vary much along the downslope direction. It is important to note that the pressures here are the full dynamic pressures in contrast to the usual hydrostatic pressure often dealt with in granular flows and mass flows, such as avalanches and debris flows. The full dynamic pressure p can be expressed as a sum of the hydrostatic (p_H) and the dynamic (p_D) pressure: $p = p_H + p_D$, where $p_H = \rho g \cos\zeta(h - z)$ with the flow height h. We see from Fig. 3.12 that the dynamic pressure is important in granular flows. Due to the extensional motion of the granular material in the channel, the hydrostatic pressure significantly overestimates the full pressure p. This becomes clearly visible near the silo inlet. Except in the vicinity of the silo inlet, the dynamic pressure is almost uniform through the flow depth. Analysis of such phenomena is made possible with the full dimensional consideration of the flow.

The previous discussion of Fig. 3.6 has indicated that the (xz-) shear profile varies along the channel differently depending on the friction law. This becomes clear in

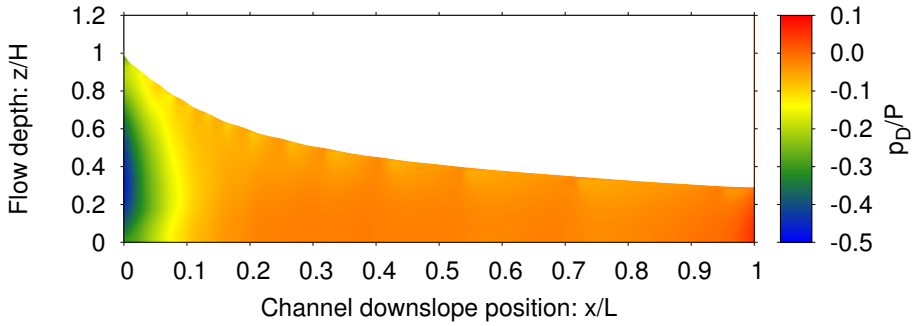

Figure 3.12: Dimensionless dynamic pressure, where $p_D = p - p_H$ and $p_H = \rho g \cos\zeta (h - z)$, for Coulomb friction law with $\delta = 25°$.

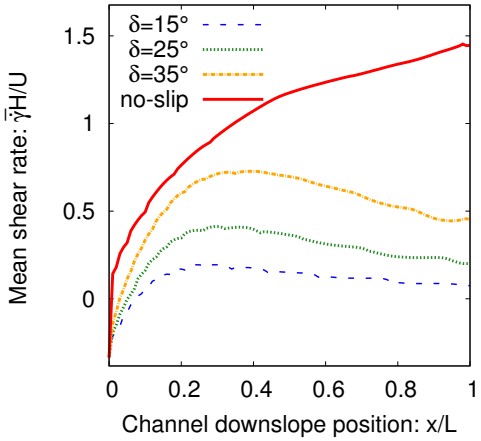

Figure 3.13: Dimensionless mean shear rate, with $\bar{\dot{\gamma}} = (u^{\text{surf}} - u^{\text{b}})/h$, along the channel for Coulomb friction, with $\delta = (15°, 25°, 35°)$, and no-slip basal friction laws.

Fig. 3.13, in which the shearing, characterised by $\bar{\dot{\gamma}} = \left(u^{\text{surf}} - u^{\text{b}}\right)/h$, is presented at different positions in the channel, where u^{surf} is the tangential surface velocity, u^{b} is the tangential bottom velocity, and h the flow depth. Therefore, the mean shear rate $\bar{\dot{\gamma}}$ is an appropriate representative quantity to characterise the interaction of the flowing material with the bottom surface and to distinguish between the different friction laws. The no-slip boundary condition leads to a continuously increasing shearing, see Fig. 3.7 (for velocities) and Fig. 3.9 (for heights), compared to the pressure-dependent Coulomb sliding law. For the latter, shearing reaches its maximum value after a certain distance from the inlet (for $\delta = 25°$ at about $\hat{x} = 0.3$) and afterwards it drops slowly. This is compatible with the pressure distribution in Fig. 3.11(a). For both friction laws and all δ values, negative values of $\bar{\dot{\gamma}}$ are observed in the vicinity of the silo inlet. These result from the inflow boundary conditions, see §3.4.1. The shear rate increases substantially with rising basal friction angle, which controls the frictional strength. Coulomb friction seems to be the more appropriate one for granular flow simulations, whose strength depends on and increases with the material friction.

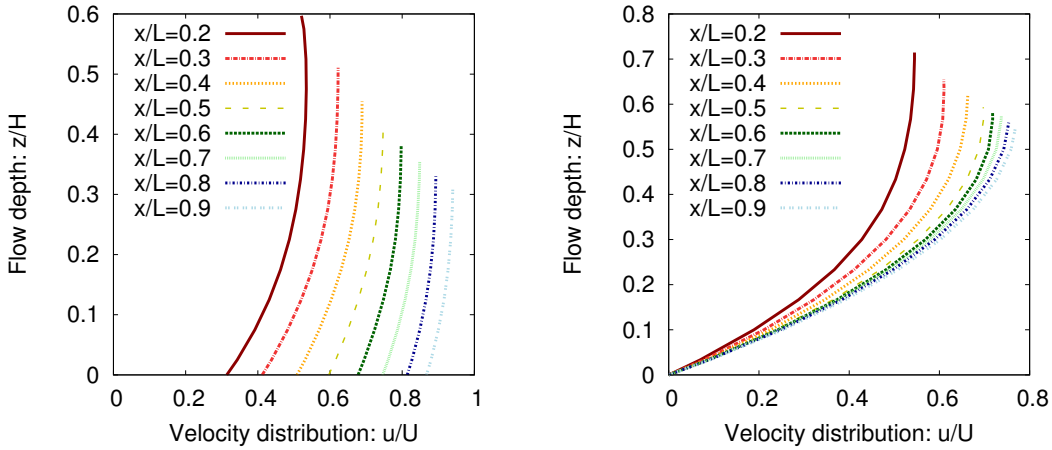

(a) Coulomb friction law with $\delta = 25°$.

(b) No-slip boundary condition.

Figure 3.14: Non-dimensionalised velocity distribution through depth at different channel positions for Coulomb friction law with $\delta = 25°$ (a), and no-slip boundary condition (b).

The variation of the tangential velocity, u, with the flow normal direction z has a completely different characteristic for the simulation with Coulomb friction law as compared to the same with the no-slip boundary condition, see Fig. 3.14(a) and Fig. 3.14(b) and also Fig. 3.15(a) and Fig. 3.15(b). Both simulations show a shear layer near the bottom, which fluently merge into a sliding layer for channel positions at some distant from the inlet ($\hat{x} \geq 0.1$). The results in Fig. 3.14(b) are similar to the fully two-dimensional plane velocity field through the depth and along the channel as derived analytically by Pudasaini (Pudasaini, 2011). For the Coulomb friction law, observable shearing mainly takes place close to the sliding surface, which is in agreement with the experimental observations (Kern et al., 2004; Pudasaini et al., 2005c, 2007; Pudasaini and Hutter, 2007; Rognon et al., 2008), but in contrast to the no-slip boundary condition. Furthermore, we observe that in the case of the no-slip boundary condition, the shear-stress at the bottom increases along the channel, but if the Coulomb sliding law is used, it decreases slightly in the far downstream. The latter is experimentally confirmed for snow avalanches (Upadhyay et al., 2010).

The Froude number (Fr) is an important non-dimensional number that characterises the dynamics of free surface gravity flows (Gray et al., 2003; Hákonardóttir and Hogg, 2005). It distinguishes subcritical (slow), critical, and supercritical (rapid) flow regimes, depending on whether Fr is less than, equal to, or greater than unity. Classically, in channel flows of water or granular flows in inclined channels, Fr is defined as the ratio between the inertial and gravity forces or equivalently between the kinetic and potential energies. It is used to establish dynamical similarities between the full-scale and laboratory-scale flows, e.g., in designing the avalanche protection dam and weir (Hákonardóttir and Hogg, 2005). Here, we consider the extended Froude number (Pudasaini and Domnik, 2009), which includes both the pressure potential and gravity

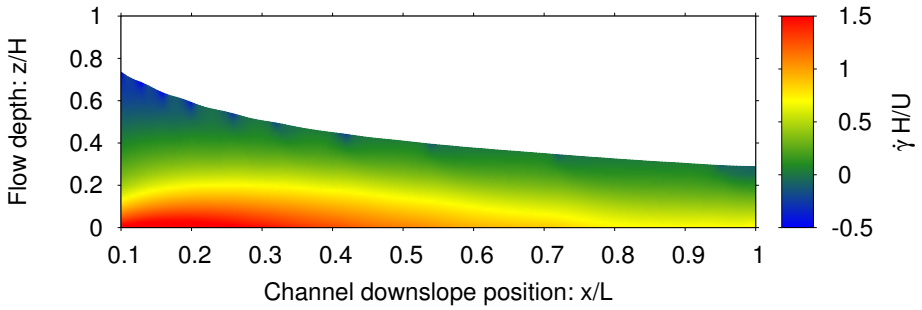

(a) Coulomb friction law with $\delta = 25°$.

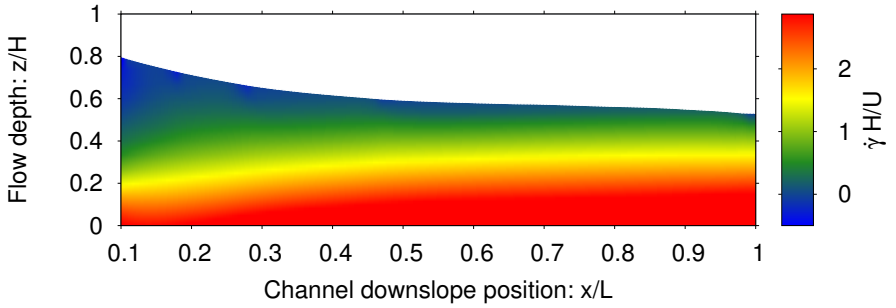

(b) No-slip boundary condition.

Figure 3.15: Non-dimensionalised gradient of the tangential velocity in direction normal to the bottom surface, i.e. the shear rate $\dot{\gamma} = \partial_z u$, for channel positions for Coulomb friction law with $\delta = 25°$ (a) and no-slip boundary condition (b).

potential energies. We further generalise the extended Froude number for non-depth averaged flows and call it 'generalised Froude number':

$$Fr = \sqrt{\frac{(u^2 + w^2)}{g\left[(L - x)\sin\zeta + z\cos\zeta\right] + p/\rho}}\,. \tag{3.30}$$

Here, $u^2 + w^2$ is twice the (two-dimensional) kinetic energy, $g\,(L - x)\sin\zeta$ is the potential energy caused by the downslope gravitational acceleration, $gz\cos\zeta$ is the potential energy caused by the gravitational acceleration along the flow depth, and p/ρ is the pressure potential energy (all energies are considered per unit mass). For $w = 0$, $z = 0$, and p defined by the hydrostatic pressure, (3.30) degenerates into the extended Froude number defined in Pudasaini and Domnik (2009).

The advantage of the generalised Froude number is that the whole spectrum of the Froude number through the flow depth and down the entire channel is available. Following Pudasaini and Domnik (2009), the reference level for the potential energy lies at the bottom surface at the end of the channel. In Fig. 3.16 we observe that the Froude number increases along the downslope position, because the kinetic energy increases, due to gravitational acceleration, and the potential energy decreases. While moving from the bottom to the free surface of the flow, the Froude number increases, although this holds also for the potential energy. This is, because of the frictional resistance at the bottom, which leads to a strong increase of the kinetic energy in the direction of

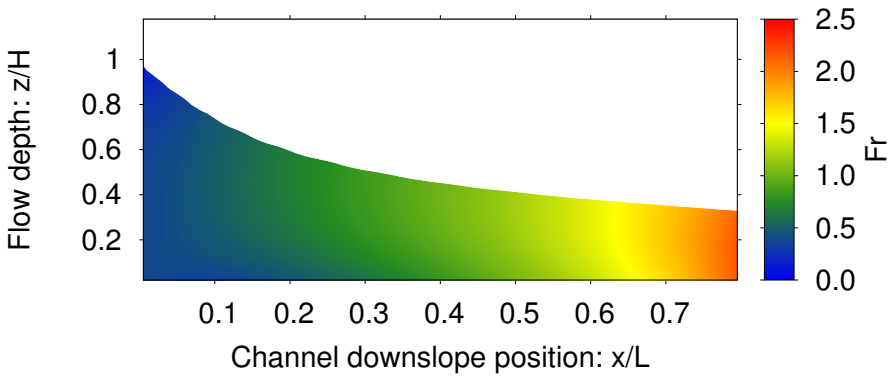

Figure 3.16: Generalised Froude number for Coulomb friction law with $\delta = 25°$.

the free surface. So, in general, the Froude number is not uniform through depth.

At $\hat{x} = 0.4$ the Froude number is approximately one, and the flow passes from the subcritical to the supercritical regime. Therefore, granular flows on inclined surfaces are characteristically rapid supercritical flows. However, note that as viewed from the bottom surface, the flow regime is slightly curved to the upstream and then straight at the top of the free surface. It can be observed by following the central part of the yellow zone.

Parameter studies

Here, the influence of the physical parameters ζ (channel inclination), ν (kinematic viscosity), $\bar{u}_{\text{in}}$ (mean inflow velocity), and h_{in} (inflow height) on the shear rate parameter $\bar{\dot{\gamma}}$ is studied for both quasi-steady-state flows obeying the Coulomb friction law with a bed friction angle of $\delta = 25°$ and flows subject to the no-slip boundary condition. It is observed in Fig. 3.13 that the shear rate parameter lines $\bar{\dot{\gamma}}(x)$ do not cross each other for the simulations with different friction laws. This holds also for simulations which differ in one of the physical parameters. Therefore, the value of $\bar{\dot{\gamma}}$ at the middle of the channel ($\hat{x} = 0.5$), $\bar{\dot{\gamma}}^{\text{c}}$, can be considered as a characteristic value for the entire friction law with a given parameter. The advantage of $\bar{\dot{\gamma}}^{\text{c}}$ is its negligible dependency on the inflow and outflow boundary conditions.

Figure 3.17 shows the fall of $\bar{\dot{\gamma}}^{\text{c}}$ for rising inclination angles ζ for Coulomb friction law. On the one hand, the decreasing gravitational acceleration normal to the bottom surface ($\propto \cos\zeta$) leads to a reduction of the bottom normal stress. On the other hand, the increasing gravitational force parallel to the bottom surface ($\propto \sin\zeta$) results in an additional acceleration of the flow and hence enhances flow velocities and lower flow depth. For the Coulomb friction, the bottom normal stress defines the bottom shear-stress. Therefore, the bottom velocity grows more quickly than the surface velocity, and the bottom shear rate, and also the mean shear rate $\bar{\dot{\gamma}}$, decreases with increasing inclination angle. No-slip flows, for which the frictional resistance is not connected to the bottom normal stress, show an inverse behaviour: The shear rate increases with the inclination angle, because the bottom velocity remains zero independent of the inclination angle. Consequently, the drop of the shear rate with increasing incli-

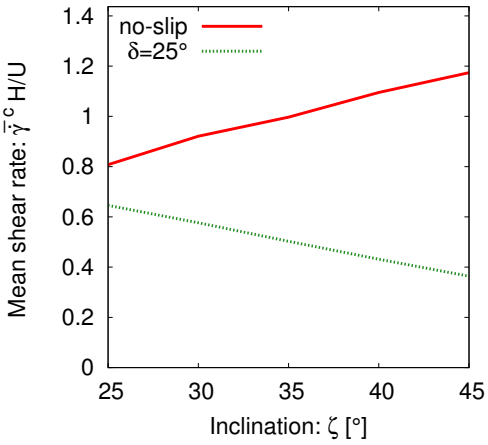

Figure 3.17: Dimensionless shearing parameter $\bar{\dot{\gamma}}^c H/U$ for steady state flows in a rectangular channel with varied inclination angles. The frictional resistance at the bottom is described by the Coulomb friction law with a bed friction angle of $\delta = 25°$ (dotted green line) and the no-slip boundary condition (solid red line), respectively.

nation is characteristic for the (dry) Coulomb friction law. However, Rognon et al. (2008) showed for chute flow experiments with snow that the shear rate increases with inclination, at which a non-zero sliding velocity is observed. This indicates a velocity-dependent friction component, which may result from the roughness of the bottom surface as the channel bottom was covered with sand paper. This shows that the inclusion of drag in the basal sliding law may become necessary in some situations (Fischer et al., 2012).

The viscosity is a measure of the resistance against deformation, e.g., induced by the frictional force at the bottom, and high viscosity means a high resistance. Therefore, a rise in viscosity leads to a decrease in mean and surface flow velocities and hence an increase in flow depth. However, for Coulomb friction, the bottom velocity shows a different behaviour compared to the surface velocity: It grows with rising viscosity, because of a lower amount of transfer of the shear-stress exerted by the bottom surface into the granular material. Note that the bottom shear-stress, which is induced by the Coulomb friction or the no-slip boundary condition, is viscosity-dependent. This dependency is positive and weaker than a linear relation. As a consequence, for both the Coulomb friction and the no-slip boundary condition, the shear rate $\bar{\dot{\gamma}}$ decreases with increasing viscosity, Fig. 3.18. The decrease is faster for the Coulomb friction due to its weaker viscosity-dependency. For a given viscosity, shear rate in Coulomb-sliding is less than the same with no-slip boundary condition.

In Fig. 3.19, the dependence of $\bar{\dot{\gamma}}^c$ on the mean inflow velocity $\bar{u}_{\text{in}}$ is illustrated. If the material is fed with higher velocity, the mean and surface velocity along the channel and also the flow depth will rise. However, for the Coulomb friction the bottom velocity is negatively correlated with the bottom normal stress, which increases due to the growth in depth. Therefore, the bottom shear rate increases substantially with

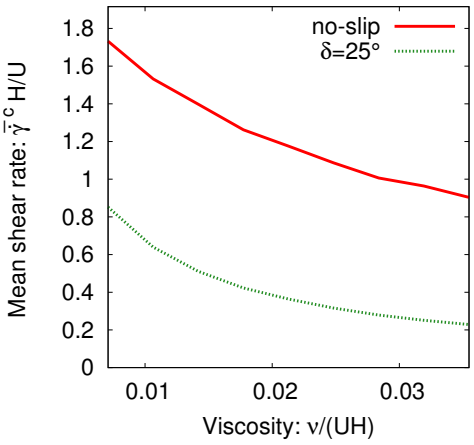

Figure 3.18: Dimensionless shearing parameter $\bar{\dot{\gamma}}^c H/U$ for steady state flows with varied dimensionless viscosities $\nu/(UH)$. The frictional resistance at the bottom is described by the Coulomb friction law with a bed friction angle of $\delta = 25°$ (dotted green line) and the no-slip boundary condition (solid red line), respectively.

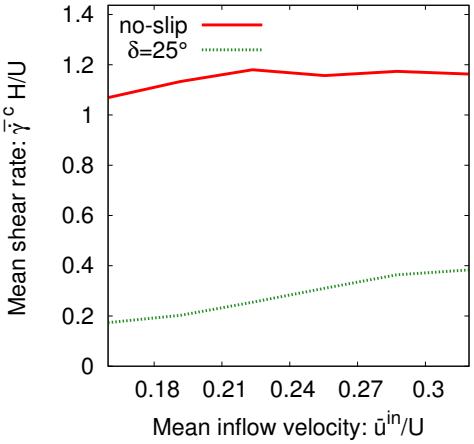

Figure 3.19: Dimensionless shearing parameter $\bar{\dot{\gamma}}^c H/U$ for steady state flows with varied dimensionless inflow velocities $\bar{u}_{\text{in}}/U$. The frictional resistance at the bottom is described by the Coulomb friction law with a bed friction angle of $\delta = 25°$ (dotted green line) and the no-slip boundary condition (solid red line), respectively.

rising inflow velocities and hence the mean shear rate $\bar{\dot{\gamma}}$ for the Coulomb friction law. For the no-slip boundary condition, the variation of the inflow velocity generates a slight change in the bottom shear rate. Consequently, the mean shear rate shows a moderate increase, decrease respectively, with rising $\bar{\dot{\gamma}}$ if the change in the free surface velocity dominates the change in the flow depth, or vice versa respectively. Note that an increase or decrease of the Coulomb friction angle will respectively amplify or soften the change of the mean shear rate with the physical property due to (3.10).

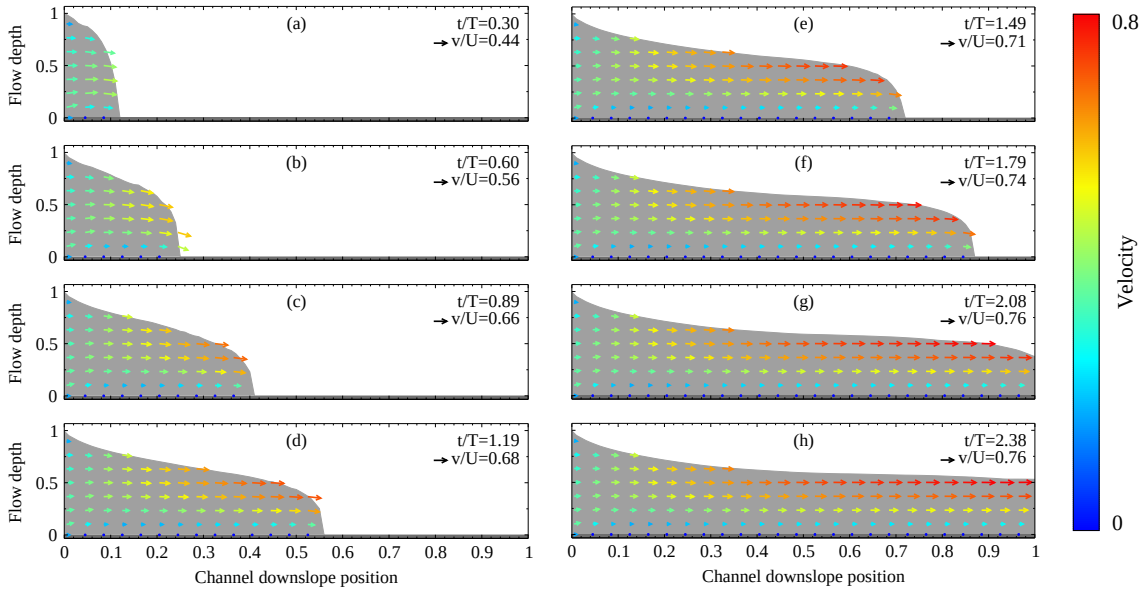

Figure 3.20: Snapshots of rapidly flowing granular material down a steep rectangular open channel. The interaction of the fluid with the channel bottom is modeled by the no-slip boundary condition.

3.4.3 Flow evolution

In this section, the time dependence of the flow is examined. This is important to describe the overall flow dynamics and the temporal and spatial variations of the flow depth and the velocity distributions through the flow depth. Here, we investigate the complete flow evolution from the flow release from the silo gate down the entire channel. This will be done for all three frictional resistances and the results are compared.

In Fig. 3.20, snapshots of the velocity fields are shown for the no-slip boundary condition. In panel (a) (at time $\hat{t} = 0.3$) the maximum front velocity is located at the middle height of the front ($\hat{z} \approx 0.3$). With time (panels b-f), the free surface of the flow front becomes the fastest flowing region as a result of the strong frictional resistance at the bottom. As a consequence, the flow front deforms only marginally. The free-slip boundary condition leads to completely different velocity fields and flow heights due to the missing friction at the bottom, Fig. 3.21. At all timesteps the maximum front velocity is located at the bottom. However, the velocity differs only slightly through the depth. The front shape is more diffusive compared to the no-slip flow.

For a Coulomb friction with $\delta = 25°$, the evolution of the flow with time is presented in Fig. 3.22. For some times, panels (a)-(c), the maximum velocity is located at the front head, somewhere between the free surface and the bottom surface. For later times, panels (d)-(f), the vertical position of the maximum velocity is close to the free surface at the forehead. So, it shows the evolution of the maximum velocity region within the sliding and dynamically evolving material. As time elapses, the flow front becomes more and more diffusive, and the (xz-) shearing becomes more visible. Compared to the other friction laws (Fig. 3.20 and Fig. 3.21), the diffusion and the flow height

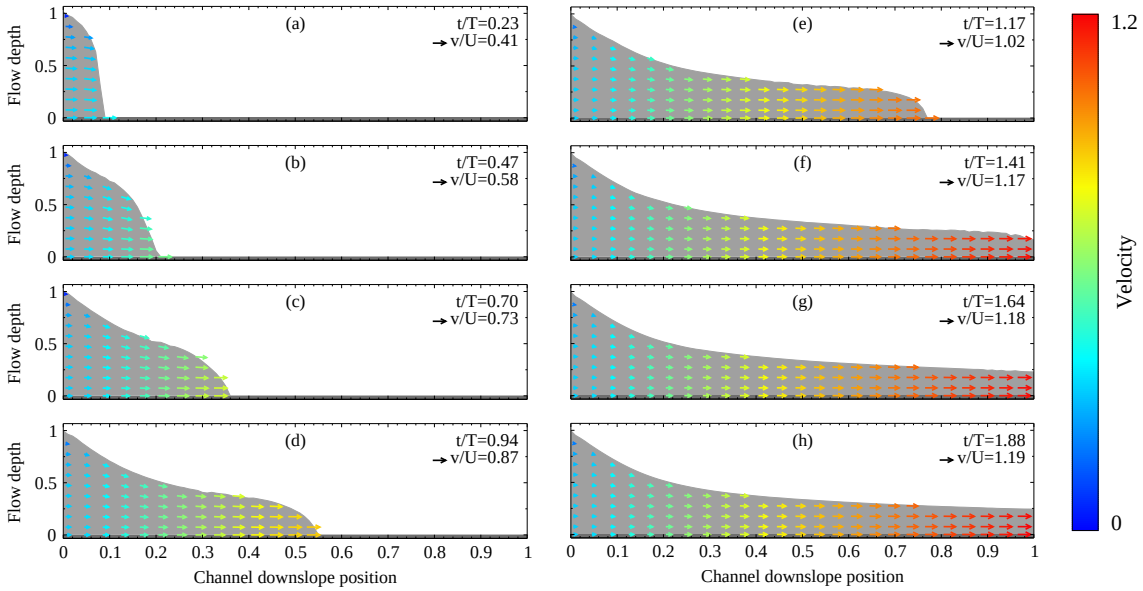

Figure 3.21: Snapshots of rapidly flowing granular material down a steep rectangular open channel. The interaction of the fluid with the channel bottom is modeled by the free-slip boundary condition.

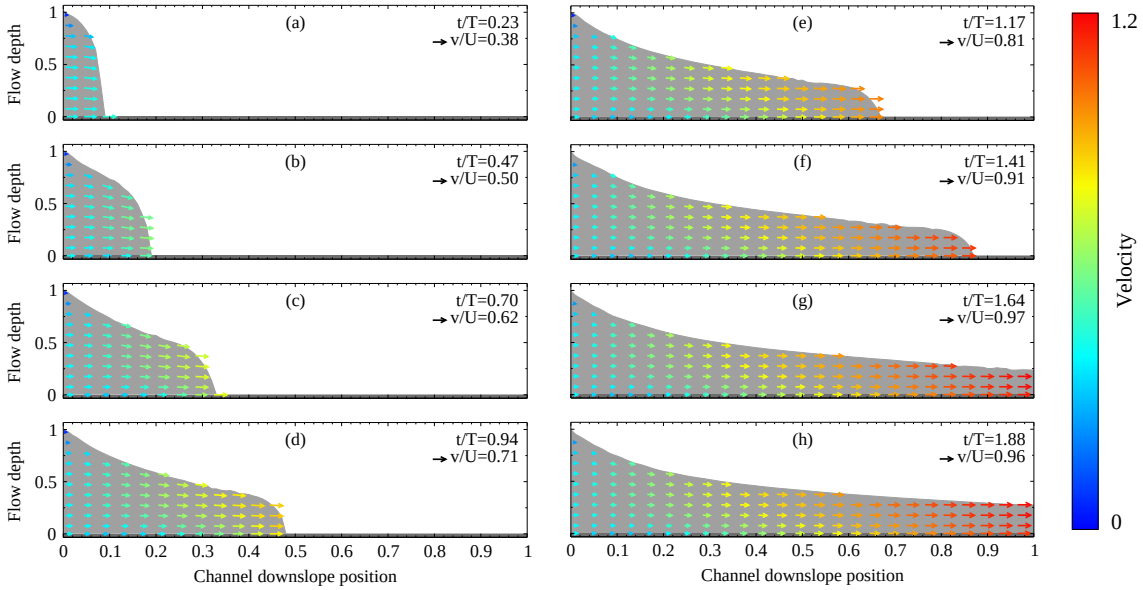

Figure 3.22: Snapshots of rapidly flowing granular material down a steep rectangular open channel. The interaction of the fluid with the channel bottom is modeled by the Coulomb friction law with $\delta = 25°$.

lies between the one produced by the free-slip and the one of the no-slip boundary condition.

This demonstrates that the no-slip, free-slip and Coulomb friction boundary conditions do not only lead to completely different flow properties and characteristics, when a quasi-steady-state flow is considered, but also during the whole temporal evolution of

the flow. The results with Coulomb friction law are in line with our physical intuition and observed phenomena.

3.5 Discussions and summary

Flow dynamical quantities, e.g., depth, velocities and pressure, play a crucial role for the construction of defence structures, hazard mitigation in disaster prone mountain regions, and also in the transportation of granular material in process engineering. Therefore, in general, we need a physically complete description of the flow dynamics without reduction of the information through the flow depth. It is observed in experiments and in the field that in rapid flow of granular material down the slopes, even the lowest particle layer in contact with the bottom boundary moves with a non-zero and non-trivial velocity. Hence, an appropriate physical model, including an adequate rheology, reasonable boundary conditions and a reliable numerical method, is required, in order to properly determine the flow dynamics associated with geophysical and industrial mass flows, such as avalanches, debris flows, and flow of granular materials. Explicit knowledge of the dynamic and variable basal slip was skipped in depth-averaged models and simulation due to depth-averaging.

We developed a fully two-dimensional, novel Coulomb-viscoplastic sliding model, which includes some basic features and observed phenomena in dense granular flows like the exhibition of a yield strength and a non-zero slip velocity. The internal deformation is modelled as a viscoplastic material. The interaction of the flow with the solid boundary is described by the pressure and rate-dependent Coulomb-viscoplastic sliding law, which relates the shear-stress to the normal stress at the boundary. This relation is linear and defined by the bed friction angle. The non-hydrostatic and full dynamic pressures is modelled as a Poisson equation in terms of the flow dynamic and gravity forces, including the material friction, viscous, and strength parameters. The numerical treatment of the Coulomb-viscoplastic sliding model requires the set up of a novel pressure equation, which defines the pressure independently of the bottom boundary velocities. These are dynamically and automatically defined for given pressure by the Coulomb-viscoplastic sliding law, which we numerically implemented for the first time. This represents an entirely novel and innovative concept in rapid granular flows both from a physical modelling and a computational point of view. To simulate and visualise the rapid free surface flow of frictional granular material, the marker-and-cell method is applied. With the new model we can simulate the entire flow dynamics and the flow depth variations of the field quantities, mainly the velocity and full dynamic pressure, and also other derived quantities, such as the shear rate, dynamic pressure, etc. Furthermore, it provides a complete dynamical description of the time and spatial evolution of the basal boundary slip velocity, which was lacking in the literature.

We numerically studied the fully two-dimensional inclined channel flow for three different basal boundary conditions: no-slip, free-slip and the Coulomb-type slip at the base. We showed that the choice of the bottom boundary is very crucial as it can fundamentally alter the flow dynamics. The Coulomb sliding law leads to non-vanishing slip velocities and to completely different distributions of the flow height and veloc-

ities than those obtained with usual boundary conditions like the no-slip boundary condition. The latter are unphysical for many frictional flows, especially for granular materials as observed in experiments and in the field. This means that the bottom boundary condition is an important mechanism to appropriately control and describe the flow dynamics in rapid granular flows in steep channels. It is demonstrated that high bed friction angles go along with a strong shearing. In reality the bed friction angle depends on both the granular material and the boundary substrate. We showed that for Coulomb friction law observable shearing mainly takes place close to the sliding surface in agreement with observations. This cannot be modelled by classical free-slip and no-slip boundary conditions. Furthermore, we observed that the bottom shear-stress increases along the channel, in the case of the no-slip boundary condition, but decreases slightly in the far downstream if the Coulomb sliding law is used.

We defined the general Froude number for a fully two-dimensional inclined channel flow and showed that it increases with downslope positions and also while moving from the bottom to the free surface. In general, the Froude number is not uniform through the depth. The analysis of the Froude number showed that granular flows on inclined surfaces are characteristically rapid supercritical flows.

Also the no-slip and the Coulomb friction law simulations show completely different results for the variation of the inclination angle, which reveals that the drop of the shear rate with increasing inclination is characteristic of the Coulomb friction law. This is useful to classify the flow regimes in laboratory experiments and field events. We showed that the simulated full dynamic pressure differs considerably from the hydrostatic pressure, which is used in classical avalanche and granular flow models. In extensional flow regimes the hydrostatic pressure largely overestimates the full dynamic pressure, whereas we expect that for strong compressional flows, e.g., in the vicinity of flow obstacle interaction, an underestimation may be observed, see Chapter 4. This is particularly critical for the construction of defence structures in disaster prone mountain regions.

Chapter 4

Multiscale Coupling of Granular Flows*

As an extension of the model and simulations presented in Chapter 3, here we develop a full two-dimensional Coulomb-viscoplastic model and apply it for inclined channel flows of granular materials from initiation to deposition. The presented model includes the basic features and observed phenomena in dense granular flows like the exhibition of a yield strength and a non-zero slip velocity. A pressure-dependent yield strength is proposed to account for the frictional nature of granular materials. The yield strength can be related to the internal friction angle of the material and plays an important role, e.g., in deposition processes. The interaction of the flow with the solid boundary is modelled by a pressure and rate-dependent Coulomb-viscoplastic sliding law. We develop an innovative multiscale strategy to couple the full two-dimensional, non depth-averaged model (N-DAM) with a one-dimensional, depth-averaged model (DAM). With the coupled model the computational complexity reduces dramatically by using DAM in regions with smooth changes of flow variables. In regions where depth-averaging becomes inaccurate, like in the initiation and deposition regions and particularly, when the flow hits an obstacle or a defence structure, N- DAM must be used, because in these regions the momentum transfer must be considered in all directions. The performance of the coupling is very high: The numerical results obtained by the coupled model deviate only slightly from the ones generated with the full two-dimensional model. This shows that the coupled model, which retains all the basic physics of the flow, is an attractive alternative to an expensive, full two-dimensional model.

Appendix C presents a graphical representation of the implementation of the multiscale coupling strategy.

*This chapter is based on: Domnik, B., Pudasaini, S.P., Katzenbach, R., and Miller, S.A., 2013a. Coupling of full two-dimensional and depth-averaged models for granular flows. Journal of Non-Newtonian Fluid Mechanics, 201:56–68.

4.1 Introduction

Flows of dense granular materials are well described by viscoplastic constitutive laws (Jop et al., 2006; Ancey, 2007; Balmforth and Frigaard, 2007; Forterre and Pouliquen, 2008; Moriguchi et al., 2009), in which the material yields and starts to flow once a yield criterion is satisfied. The yield criterion depends on the stress state and a yield strength, which has to be exceeded to start flowing. Bingham materials are described by a constant and empirical yield stress and flow like a viscous fluid at high stresses (Bingham, 1922). In applications, this simple viscoplastic rheology is often an adequate choice (Dent and Lang, 1982; Voight and Sousa, 1994; Whipple, 1997; Gauer et al., 2006; Domnik and Pudasaini, 2012). When the friction between the grains becomes considerable or even dominant, like in slow motions and especially in deposition regimes, this assumption could be too simple. Jop et al. (2006) account for the frictional nature of the granular material by assuming a pressure-dependent yield stress and an effective viscosity depending on the shear rate and the local pressure. With their approach, which mainly concerns the yield criterion, the relatively slow motion of granular materials on mild inclines (close to or below the internal friction angle) is successfully described. Moriguchi et al. (2005, 2009) proposed a Bingham type constitutive model for rapid granular flows down inclined planes hitting a rigid obstruction. In their framework the yield stress is defined by the Mohr-Coulomb failure criterion and depends on the internal friction angle. With their model they could reasonably well describe the impact force on a rigid obstruction.

Another important aspect of granular flow simulation is the description of the interaction with the basal boundary, which is often simplified by assuming a no-slip boundary condition (Moriguchi et al., 2005; Jop et al., 2006; Moriguchi et al., 2009). However, as mentioned in Chapter 3, it is observed in experiments and in the field that in rapid flow of granular material down the slopes, even the lowest particle layer in contact with the bottom boundary moves with a non-zero and non-trivial velocity (Massoudi and Phuoc, 2000; Pudasaini et al., 2005c; Platzer et al., 2007a,b; Pudasaini and Hutter, 2007; Pudasaini et al., 2007). In a viscoplastic granular flow model presented in Chapter 3 , the Coulomb friction law is used to model the interaction of the flow with the solid basal boundary surface. The bed friction angle defines the frictional strength and depends on both the granular material and the boundary substrate. Here, we advance this model by introducing a pressure-dependent yield stress, which can be related to the internal friction angle similar to Moriguchi et al. (2009). However, in contrast to Moriguchi et al. (2009), we are able to describe non-zero slip velocities by the Coulomb friction law as in Domnik and Pudasaini (2012). Hence, the presented full two-dimensional Coulomb-viscoplastic granular flow model, characterised by the internal and bed friction angle, constitutes a substantial improvement of the existing models.

Full two-dimensional, non depth-averaged models require very large computational costs. Therefore, it is desirable to develop a coupled hybrid model, in which the more expensive, non depth-averaged model is solved only in some selected local domains, where depth-averaging is not appropriate, and a depth-averaged model is used in the

remaining complementary domain. This coupling method represents a multiscale and multiphysics strategy, as the scale of the momentum transfer in the flow depth direction and also the applied physical model is different for the depth-averaged and non depth-averaged subdomains. The significant advantage using the coupled model is that it requires much less computing time and provides a full two-dimensional description of the flow in the relevant regions. For instance, such a multiscale strategy is reported in Formaggia et al. (2001) and Miglio et al. (2004) for subcritical flows of simple Newtonian fluids. However, to our knowledge, a multiscale and multiphysics strategy has not yet been developed and applied for rapid flows of frictional granular materials on inclined channels, which are very important geophysical and industrial mass flow processes.

As the available computer power has increased enormously, discrete element methods (DEM) become more important. They compute the motion of a large number of particles and can be used to simulate a wide variety of granular flows and rock mechanics problems. Discrete particle simulations on model systems serve as a good possibility for a detailed study of the rheology of moving granular material (MiDi, 2004; da Cruz et al., 2005; Zhu et al., 2008). Nevertheless, the number of particles that can be dealt with at the moment is limited. Therefore, their application is restricted to small scale flows (Pudasaini and Hutter, 2007; Zhu et al., 2008). Geophysical mass flows consist of huge volumes (Pudasaini and Miller, 2013) and are thus less likely to be fully described by DEM.

In Section 4.2 we derive a full two-dimensional Coulomb-viscoplastic model for granular materials with a pressure-dependent yield stress. The yield stress is defined by the internal friction angle and the pressure. The interaction of the flow with the solid basal boundary surface is described by a Coulomb friction law. Section 4.3 is devoted to the derivation and analysis of a depth-averaged, one-dimensional granular flow model for free surface flows down an inclined channel. The constitutive behaviour of the granular material is assumed to be described by a Mohr-Coulomb yield criterion. Then in Section 4.4, the decomposition of the computational domain into full 2D (two-dimensional) and depth-averaged 1D (one-dimensional) regions and appropriate matching conditions at the interfaces are discussed for the coupled model. The performance of the coupled model is studied numerically in Section 4.5. Two different flow configurations are considered: (i) an undisturbed inclined channel flow, and (ii) a flow hitting a perpendicular wall. The correspondence between of the material parameters used in the both models (1D and 2D) is analysed. In detail, we study the impact of the interface position on the accuracy of the coupled model. Finally, some conclusions are drawn in Section 4.6.

4.2 Full 2D Coulomb-viscoplastic granular flow model

In this section we present the full two-dimensional Coulomb-viscoplastic granular flow model, in which the pressure-dependent yield strength is introduced. The model equa-

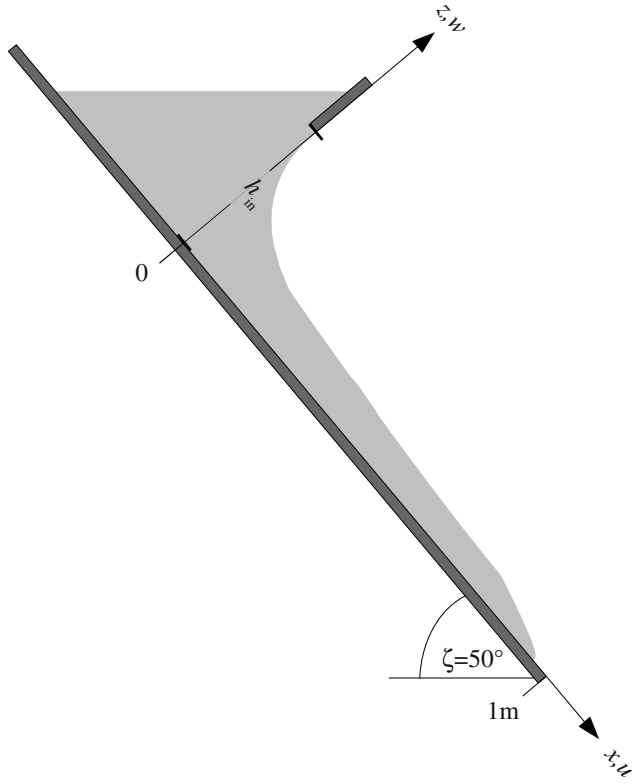

Figure 4.1: Side view of an inclined chute with considered coordinate system. The x-axis is aligned in the downslope direction and the z-axis is orientated perpendicular to it. The granular material (depicted in light grey) enters the channel at $x = 0$ through a silo gate with opening height h_{in} and flows in the downslope direction. ζ is the inclination angle of the chute.

tions and associated boundary conditions are discussed. We develop a procedure to numerically solve these equations.

4.2.1 Model equations

The rapid motion of a granular material in a two-dimensional inclined rectangular channel, Fig. 4.1, is characterised by the pressure p and the velocity $\mathbf{u} = (u, w)^T$, with u the velocity component in downslope direction (x), and w the velocity component perpendicular to the channel surface (z) (Section 3.2.1). In the dense flow regime, in which variations of the (solid) volume fraction are small, granular flow can be assumed incompressible (Iordanoff and Khonsari, 2004; da Cruz et al., 2005; Jop et al., 2006; Pudasaini and Hutter, 2007). Nevertheless, density changes due to dilatation and compaction can become locally considerable, yet small during release, flow-obstacle interactions, or depositions. However, during long distance flows global density changes are negligible. So, in the following, granular flow is assumed incompressible and density changes are neglected. The flow in a channel inclined by an angle

ζ is described by a system of partial differential equations, representing the mass and momentum balances:

$$\begin{aligned} \operatorname{div} \mathbf{u} &= 0, && (4.1)\\ \frac{d\mathbf{u}}{dt} &= \operatorname{div} \boldsymbol{\sigma} + \mathbf{g}. && (4.2) \end{aligned}$$

We consider a dry dense granular material where motion and settlement are assumed to be well described by viscoplastic constitutive laws (Jop et al., 2006; Ancey, 2007; Balmforth and Frigaard, 2007; Forterre and Pouliquen, 2008). The normalised stress tensor (normalised by density) for a viscoplastic fluid can be described by the constitutive relation

$$\boldsymbol{\sigma} = -p\mathbb{1} + 2\nu\mathbf{D} + 2\tau_y \frac{\mathbf{D}}{||\mathbf{D}||}. \tag{4.3}$$

Equation (4.3) can also be written in terms of an effective viscosity

$$\nu_{\text{eff}} = \nu + \frac{\tau_y}{||\mathbf{D}||}\,, \tag{4.4}$$

as $\boldsymbol{\sigma} = -p\mathbb{1} + 2\nu_{\text{eff}}\mathbf{D}$. When the strain rate $||\mathbf{D}||$ equals zero, the effective viscosity becomes infinite. In order to avoid such infinite value, which cannot be treated in numerical simulations, an exponential factor is introduced like in (3.4). For $\tau_y = 0$ the material behaves as a Newtonian fluid. A Bingham material is described by a constant yield stress. Here, we propose a pressure-dependent yield stress to better represent the frictional nature of the granular material:

$$\tau_y = \tau_p p\,. \tag{4.5}$$

Equation (4.5) forms a Drucker-Prager yield criterion with zero cohesion

$$\sqrt{II_{\sigma_D}} \geq \tau_p p\,, \tag{4.6}$$

where II_{σ_D} is the second invariant of the deviatoric stress tensor (Prager and Drucker, 1952). The relation (4.6) states that the material undergoes plastic yielding, when the deviatoric stress is greater than the yield stress. The yield stress plays an important role for the transition of a granular material from a solid (no deformation) to fluid (deformation) state and vice versa, reminiscent of the flow initiation and the deposition process. In two space dimensions the Drucker-Prager yield surface is identical to the Mohr-Coulomb yield surface, and τ_p can be expressed by $\tau_p = \sin\phi$, where ϕ is the internal friction angle and describes the friction between the grains. Note that sometimes the expression $\tau_p = \tan\phi$ is used for the yield stress in the literature (e.g., Moriguchi et al. (2005), Oda et al. (2011)), which is an approximation and only valid for small internal friction angles. For typical values of ϕ, which are in the order of 30° for granular flows, one should use $\tau_p = \sin\phi$. The pressure dependence of the yield stress causes a higher material resistance against deformations for regions under high pressure. Therefore, the shock front evolution for a flow against an obstacle or a rigid

wall is very sensitive to the internal friction angle due to high pressures appearing at or in the vicinity of the wall (Pudasaini and Kröner, 2008). The same is true during the deposition process and the flow convergence. As we will see later, the pressure-dependent yield stress is a good rheological model for granular flows considered here. Cohesion can easily be included in model (4.3) by adding a constant tensile stress τ_c to the total yield stress $\tau_y = \tau_c + \tau_p p$. As we are considering dry granular materials, for simplicity we set $\tau_c = 0$. Note that for slow motion of grains Jop et al. (2006) also utilised a pressure-dependent effective viscosity, $\nu_{\text{eff}} = \mu(I)p/\,||\mathbf{D}||$, where $\mu(I)$ is the friction coefficient, which depends on the inertial number I. However, in their formulation no linear viscous stress contribution (linear in the strain rate $||\mathbf{D}||$) is taken into account ($\nu = 0$) and the strain rate dependence of the stresses is through $\mu(I)$, which is limited by the parameter μ_2 for high values of I. The friction coefficient requires three material dependent constants, which must be determined in experiments on steady uniform flows. In our model, we use the simple relations (4.4) and (4.5), in which τ_p is obtained in terms of the internal friction angle, which does not require any fit parameters. This is an advantage.

With the notation

$$\mathbf{F} = \mathbf{g} - (\mathbf{u} \cdot \nabla)\,\mathbf{u} + \nu \Delta \mathbf{u} + 2\,\text{div}\left(\tau_y \frac{\mathbf{D}}{||\mathbf{D}||}\right), \tag{4.7}$$

the momentum equation (4.2) can now be expressed as (by utilising the continuity equation (4.1))

$$\partial_t \mathbf{u} = \mathbf{F} - \nabla p\,. \tag{4.8}$$

Equation (4.8) is integrated numerically to compute the velocity field $\mathbf{u}$. A pressure equation is derived by applying the divergence operator on the momentum conservation (4.8) and using the continuity equation (4.1) to yield:

$$\Delta p = \nabla \cdot \mathbf{F}. \tag{4.9}$$

As no explicit equation for the pressure is given in the primitive variables formulation (4.1) and (4.2), the equations (4.8) and (4.9) are solved numerically. Note that $\mathbf{F}$, and hence the right-hand-side of (4.9), explicitly depend on the pressure for a pressure-dependent yield stress. This leads to a more complicated situation as illustrated in the following. For a pressure-independent yield stress, (4.9) forms the well-known Poisson equation for the pressure.

4.2.2 Boundary conditions

The model (4.1) and (4.2) must be complemented by appropriate boundary conditions. At every domain border a boundary condition for both the tangential and normal velocity is needed. In rapid flows of granular material down the slopes, even the lowest particle layer in contact with the rigid bottom boundary moves with a non-zero and non-trivial velocity (Massoudi and Phuoc, 2000; Pudasaini et al., 2005c; Platzer et al., 2007a,b; Pudasaini and Hutter, 2007; Pudasaini et al., 2007). As in Chapter

3, we use the Coulomb sliding law to model the interaction of the material with rigid boundaries:

$$T^b = c^{\mathrm{F}} N^b. \tag{4.10}$$

For example, the Coulomb sliding law at the bottom boundary with the basal normal vector parallel to the z-direction can be written as

$$\nu_{\mathrm{eff}}^b \left([\partial_z u]^b - 2c^{\mathrm{F}} [\partial_x u]^b \right) = c^{\mathrm{F}} p^b \,. \tag{4.11}$$

In deposition processes, i.e., situations, in which the material comes to rest, a discontinuity at $u^b = 0$ appears, which cannot be treated in numerical simulations. Therefore, we use an exponential factor, $\left[1 - \exp\left(-m_c u^b\right)\right]$, similar to that for the yield stress, to smooth the friction factor. In Chapter 3 a pressure-independent yield stress is considered, which means that also ν_{eff} does not depend on the pressure and the velocity boundary condition depends linearly on the pressure (4.11). Here, we consider a pressure-dependent yield stress ($\tau_p \neq 0$), which leads to a non-linear dependency of the velocity boundary values on the pressure, and from (4.4), (4.5), and (4.11) it follows:

$$[\partial_z u]^b = c^{\mathrm{F}} \left(2 [\partial_x u]^b + \frac{p^b \left|\left|\mathbf{D}\right|\right|^b}{\nu \left|\left|\mathbf{D}\right|\right|^b + \tau_p p^b} \right) . \tag{4.12}$$

Note that for $\delta = 0$, the friction factor c^{F} also equals zero and the simple free-slip boundary condition is obtained. Also note that Jop et al. (2006) use a no-slip boundary condition, but for particle slip along the base a boundary equation like (4.12) is necessary. At penetrable boundaries the velocity boundary conditions are defined by in- and outflow conditions. This is discussed in more detail later, when we present the coupling of the full two-dimensional with the one-dimensional, depth-averaged model.

For a constant yield stress, $\mathbf{F}$ does not depend on the pressure and consequently the pressure emerges only through a pressure gradient in the momentum equation (4.8). In fact, p appears as a Lagrange multiplier that constrains the velocity field to remain divergence-free and no additional pressure boundary conditions are required. On the contrary, a pressure dependency of the yield stress causes the pressure, p, and its derivatives, $\partial_x p$ and $\partial_z p$, to appear in every vector component of $\mathbf{F}$ in (4.7), and hence in the momentum equation (4.8) (emerging from the fourth term on the right-hand-side of (4.7)). Therefore, both pressure and velocity boundary conditions are needed to close the model equations (4.1) and (4.2). At rigid boundaries we use a Neumann boundary condition for the pressure by applying the momentum conservation in direction of the boundary normal

$$\mathbf{n} \cdot \nabla p = \mathbf{n} \cdot \mathbf{F} \,, \tag{4.13}$$

as often done in defining the boundary conditions for the pressure Poisson equation for a Newtonian fluid (Gresho and Sani, 1987; Sani et al., 2006). Note that the boundary condition (4.13) cannot be used at penetrable boundaries, where the in- or outflow velocities vary with time. However, if this variation is known, (4.13) can still be modified appropriately. At penetrable boundaries (interfaces), which occur in the

coupling between the full two-dimensional with the one-dimensional model, we will employ in- and outflow conditions for the pressure, which represent a type of Dirichlet boundary conditions. When the coupling with the one-dimensional, depth-averaged model is presented, we will cover this in more detail.

4.2.3 Numerical method

A detailed description of the numerical scheme for a pressure-independent yield stress with applications to inclined channel flows of granular materials is presented in Chapter 3. An extension of this scheme for a pressure-dependent yield stress ($\tau_p \neq 0$) is proposed in Appendix B. As in Domnik and Pudasaini (2012), we deduce from the continuity and momentum conservation a second order partial differential equation for the pressure, (4.9), which is closed by velocity and pressure boundary conditions, (4.12) and (4.13). But, different from Domnik and Pudasaini (2012), where a pressure-independent yield stress is considered, here the system of equations, formed by (4.9), (4.12), and (4.13), is non-linear in the pressure. We use a modified version of the Powell's Hybrid method to solve this non-linear system of equations (Powell, 1970; Galassi et al, 2009).

4.3 Depth-averaged 1D granular flow model

In the following a depth-averaged, one-dimensional granular flow model and its numerical solution methods are presented.

4.3.1 Model equations

We consider a simple one-dimensional frictional granular flow model, in which the constitutive behaviour of the granular material is described by a Mohr-Coulomb yield criterion. The Coulomb friction law, (4.10), is used as bottom boundary condition. By depth-averaging the incompressible equations for conservation of mass and momentum, the following equations are then obtained for the depth-averaged model (DAM) (Savage and Hutter, 1989; Gray et al., 1999; Pudasaini and Hutter, 2007):

$$\partial_t h + \partial_x \left(h\bar{u}\right) = 0\,, \tag{4.14}$$

$$\partial_t \left(h\bar{u}\right) + \partial_x \left(h\bar{u}^2\right) + \partial_x \left(\frac{1}{2}\beta h^2\right) = sh\,, \tag{4.15}$$

where t, x, h, $\bar{u}$ are the time, the coordinate along the slope, flow depth, and (depth-averaged) downslope velocity, respectively. The net driving acceleration is given by $s = g\cos\zeta\left(\tan\zeta - \tan\delta\right)$ and $\beta = gK\cos\zeta$, where ζ is the slope angle, δ is the bed friction angle, g is the gravity acceleration, and $K_{act/pas} = 2\sec^2\phi\left(1 \mp \sqrt{1 - \cos^2\phi\sec^2\delta}\right) - 1$ is the earth pressure coefficient, in which ϕ is the internal friction angle of the granular material. Note that K jumps from active (spreading, $\partial_x u > 0$) to passive (contracting, $\partial_x u < 0$) when $\partial_x u = 0$. This can be smoothed by a regularisation process (Tai and Gray, 1998). The term $\partial\left(0.5\beta h^2\right)/\partial x$ represents the pressure gradient. The source

term, s, is the interaction of the medium with the surrounding, namely the gravity and the basal friction, and it makes the system inhomogeneous.

In deriving (4.14) and (4.15), the assumption of shallowness of the granular avalanche is implemented. For this purpose the physical variables are non-dimensionalised by using the scalings (Pudasaini and Hutter, 2007)

$$(x, z, t) = \left(L\hat{x}, H\hat{z}, (L/g)^{1/2}\,\hat{t}\right), \tag{4.16}$$

$$(u, w) = (gL)^{1/2}\,(\hat{u}, \varepsilon\hat{w}), \tag{4.17}$$

where the hats represent non-dimensional variables, L is a characteristic length, and H is a characteristic height of the flow. The aspect ratio of the granular avalanche is defined as $\varepsilon = H/L$ and assumed to be small. The model equations are correct to order higher than ε.

The equations (4.14) and (4.15) comprise a hyperbolic system with the characteristic velocities $\lambda_\pm = \bar{u} \pm \sqrt{\beta h}$ (if K does not switch from active to passive or vice versa). If both characteristic velocities have the same sign, the flow is called supercritical (i.e., $\bar{u}/\sqrt{\beta h} > 1$). If the characteristic velocities have opposite sign, the flow is called subcritical (i.e., $\bar{u}/\sqrt{\beta h} < 1$). When the flowing material is stopped by an obstacle or wall, a previously supercritical flow becomes subcritical, and a shock wave is generated. We consider the depth-averaged model in regions, where ε is small and the flow is in a supercritical state. Otherwise a full two-dimensional model presented in Section 4.2 is used.

4.3.2 Numerical method

In applications the depth-averaged model is successfully solved by a higher-order non-oscillatory central (NOC) total variation diminishing (TVD) differencing scheme mainly with the Minmod TVD limiter (Tai et al., 2002; Pudasaini et al., 2005c; Pudasaini and Hutter, 2007; Pudasaini and Kröner, 2008; Mergili et al., 2012; Pudasaini, 2012). The concept of flux limiters allows to switch between high and low resolution schemes by considering the ratio r of successive gradients of the field variables on the solution mesh. With this higher-order method spurious oscillations induced by high resolution schemes can be avoided by using a low resolution scheme if the ratio r becomes large. The disadvantage of this concept, however, is that the ratio r also becomes large and even negative near extrema and a low-resolution scheme is used in these situations. We observed in simulations that for inflow conditions (at the interface between 2D and 1D regions), which do not vary strictly monotonically with time, even this can be a source for spurious oscillations. As we are considering the depth-averaged model in regions, where the flow is supercritical and no sharp wave fronts occur, we can use a high resolution scheme and do not need to introduce the concept of flux limiters. For this reason, we numerically solve the one-dimensional granular flow model by implementing a second-order non-oscillatory central differencing scheme which is based on the beam-warming method (Beam and Warming, 1976; Pudasaini and Hutter, 2007). This turns out to work very well for our particular problem.

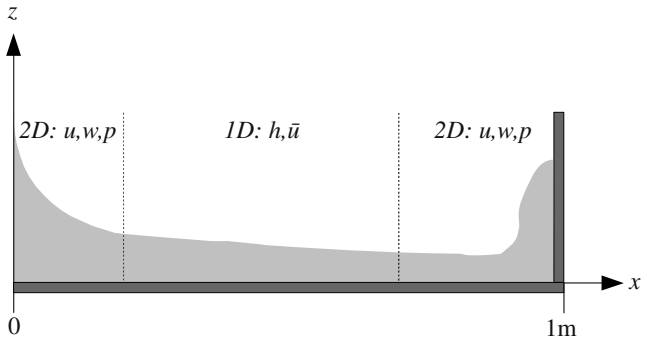

Figure 4.2: A possible domain decomposition and the associated field variables for flow along an inclined channel closed by a perpendicular wall at $x = 1\,\mathrm{m}$ downstream. The 2D model supplies the velocities u, w, and the pressure p. The 1D model provides the flow depth h and the depth-averaged downslope velocity $\bar{u}$. The dotted lines indicate the 2D-1D, 1D-2D, interface, respectively.

4.4 Coupled model

In the coupled model the two-dimensional Coulomb-viscoplastic granular flow model with pressure-dependent yield stress is used in regions with a strong full two-dimensional flow characteristic and the depth-averaged, one-dimensional granular flow model in regions with negligible momentum transfer in z-direction. Here, we propose a domain decomposition strategy of the computational domain in 2D and 1D regions and suggest appropriate boundary conditions at the interfaces, which separates these regions.

4.4.1 Domain decomposition

The computational complexity and cost can be dramatically reduced by using the one-dimensional granular flow model in regions with smooth changes of flow variables. In regions where depth-averaging becomes inaccurate, like in initiation and deposition regions, and also in flow converging and diverging regions, in particular when the flow hits an obstacle or a defence structure, the two-dimensional Coulomb-viscoplastic model is used. The regions in which the 2D (1D) model is used are called 2D (1D) regions. In Fig. 4.2 a possible domain decomposition is sketched for the channel flow illustrated in Fig. 4.1. The full two-dimensional model provides the flow velocities u, w, along x- and z-directions and the pressure p. The flow heights can be obtained by considering the position of the marker particles used in the MAC method. The one-dimensional model supplies the depth-averaged velocity $\bar{u}$ and the flow height h.

To determine whether the one-dimensional model is valid at a given position in the channel, we introduce the shallowness parameter, $\varepsilon = |w| \,/\, |u|$, as the ratio of the velocity normal to the channel (w) to the velocity along the channel (u). The shallowness parameter is equivalent to the aspect ratio H/L, since w scales with UH/L, where U is a typical velocity, which defines the scale for u, compare (4.17). If ε is small ($\varepsilon \ll 1$), the momentum transfer in the flow depth direction is much smaller than the momentum transfer along the downslope (channel) direction and depth-averaging is

legitimate. Hence, the interfaces, which separate the 2D and 1D regions, should be located at positions where the shallowness parameter is sufficiently small. Here, we propose two different strategies of domain decompositions: (i) The interface position can be set automatically during runtime by computing the shallowness parameter at every position in the channel. However, for 1D-2D interfaces this approach is not straightforward as usually the 2D-subdomain has to be enlarged with time due to the evolution of a shock wave like for a flow against an obstacle. This requires the computation of the two-dimensional model in areas where the one-dimensional model was used previously. (ii) In contrast, for simplicity we can consider static interfaces, whose position can be fixed a priori. One possibility is to carry out the domain decomposition a priori, essentially driven by experience, physical and geometrical considerations. Alternatively, an a priori estimate of the interface position can be obtained in a much better and dynamic way by performing a foregoing, fast simulation with the one-dimensional model, from which the shallowness parameter is estimated by $\varepsilon = 1/Fr^2$, where $Fr = u/\sqrt{\beta h}$ is the Froude number. As from dimensional analysis, (4.16) and (4.17), it follows that $1/Fr^2$ is equivalent to ε. However, due to the limited validity of the one-dimensional model, this provides only a rough estimate and the length of two-dimensional subdomain must be chosen somewhat greater than suggested by the one-dimensional simulation.

4.4.2 Boundary conditions for DAM at the interface

The one-dimensional granular flow model requires boundary conditions for the flow height and the mean velocity at the interface. We obtain them from the corresponding values of two-dimensional Coulomb-viscoplastic model as follows:

$$u^{1D}(t, x = x_{\text{IF}}) = \bar{u}^{2D}(t, x = x_{\text{IF}}) \,, \tag{4.18}$$

$$h^{1D}(t, x = x_{\text{IF}}) = h^{2D}(t, x = x_{\text{IF}}) \,, \tag{4.19}$$

where x_{IF} is the interface position, and depth-averaging is defined by

$$\bar{u}(t, x) = \frac{1}{h} \int_0^h u(t, x, z) dz \,. \tag{4.20}$$

However, in the one-dimensional model a staggered grid is used, where the boundaries of the cells at the new time level are the centres of the cells at the old time level. This time-staggered grid is a central concept of NOC schemes. On the contrary, a space-staggered grid, which does not move with time, is considered in the full two-dimensional model. These different numerical grids for the 1D and 2D model have to be taken into account properly, when setting the boundary conditions at the interface for both the 1D and the 2D model. (This is discussed in more detail in Appendix C.)

4.4.3 Boundary conditions for N-DAM at the interface

The treatment of the boundary conditions for the two-dimensional model is much more complex than for the one-dimensional model, because two-dimensional quantities

have to be determined from one-dimensional ones. The two-dimensional Coulomb-viscoplastic model requires boundary conditions at the interface both for the velocities u and w and the pressure p. In an intuitive first approach one can think about setting the channel parallel velocity equal to the depth-averaged one-dimensional velocity and the velocity in the flow depth direction equal to zero at the interface:

$$u^{2D}(t, x = x_{\text{IF}}, z) = u^{1D}(t, x = x_{\text{IF}}) , \tag{4.21}$$

$$w^{2D}(t, x = x_{\text{IF}}, z) = 0 . \tag{4.22}$$

However, this causes several problems. At first, it is by no means clear how to set appropriate pressure boundary conditions such that the continuity equation is fulfilled in the whole N-DAM domain. The Neumann pressure boundary condition which is used at rigid boundaries, (4.13), cannot be used at penetrable boundaries with time-dependent in- or outflow conditions. Secondly, the variation of the u velocity with depth is assumed to vanish, which is actually not the case near the base for bed friction angles $\delta > 0$. Indeed, the shearing of the material should be small at the interface, but using a u velocity constant with depth produces non-smooth velocities and pressures at the interface due to an acceleration of the material near the bottom and a deceleration of the material near the free surface. Furthermore, there is no physical justification for setting the w velocity to zero even if it is small compared to the u velocity. Instead, it contradicts with the continuity requirement, because $\partial_x u \neq 0$ in general. Therefore, we cannot use (4.21) and (4.22) as proper boundary conditions at the interface. Rather, we propose the following natural and legitimate relations at the interface:

$$\bar{u}^{2D}(t, x = x_{\text{IF}}) = u^{1D}(t, x = x_{\text{IF}}) , \tag{4.23}$$

$$\partial_x \partial_z u^{2D} = 0 , \tag{4.24}$$

$$p^{2D}(t, x = x_{\text{IF}}, z) = p^{1D}(t, x = x_{\text{IF}}, z) , \tag{4.25}$$

$$\partial_x u^{2D} + \partial_z w^{2D} = 0 . \tag{4.26}$$

Equations (4.23) and (4.24) define the channel parallel velocity at the interface, which varies with flow depth. The assumption $\partial_x \partial_z u = 0$ is not a strong constraint, because in the vicinity of the interface the momentum change in the flow depth direction is small. The isotropic pressure (defined by the trace of the stress tensor) is given by $p^{1D} = g \cos\zeta \, (h - z) \, (1 + K) \, /2$ in the one-dimensional model (Pudasaini and Hutter, 2007). Equation (4.26) represents the continuity equation. With the boundary conditions at the interface, (4.23)-(4.26), the continuity requirement is fulfilled in the whole N-DAM domain and no artificial acceleration or deceleration of the material at the interface is introduced.

4.5 Performance and numerical results of the coupled model

First, we demonstrate the performance and present an error analysis of the coupled 2D/1D/2D model. For this purpose two different setups are considered: (i) an undisturbed inclined channel flow (Setup I), and (ii) a flow hitting a perpendicular wall

(Setup II). Subsequently, the correspondence of the material parameters in the two- and one-dimensional models are investigated. Furthermore, the impact of the interface position on the numerical results is illustrated.

Some experimental results, depth-averaged exact solutions and depth-averaged numerical simulations for rapid granular flows hitting and flowing around an obstacle can be found in Gray et al. (2003) and Cui and Gray (2013).

We simulate a rapid flow of granular material down a channel with an inclination of $\zeta = 50°$, which is continuously fed from a silo, see Fig. 4.1. The inlet height is $h_{\text{in}} = 6\,\text{cm}$, and the mean inlet velocity is $\bar{u}_{\text{in}} = 0.37\,\text{ms}^{-1}$. The internal friction angle is set to $\phi = 33°$, the bed friction angle to $\delta = 22°$, and the kinematic viscosity to $\nu = 0.003\,\text{m}^2\text{s}^{-1}$. These flow configurations are similar to those used in Pudasaini et al. (2007), Pudasaini and Kröner (2008), Domnik and Pudasaini (2012), and Pudasaini and Domnik (2009). In Setup I the channel has a length of $L = 1.5\,\text{m}$ and at the end of the channel an open end outflow condition is considered. In Setup II we consider a channel of length $L = 1\,\text{m}$, which is closed by a rigid perpendicular wall.

4.5.1 Model assessment

At first, we simulate the channel flow in a rectangular domain $\Omega = [0, L] \times [0, H]$ with the full two-dimensional model, where L is the channel length and H is an appropriately chosen domain height. Secondly, we divide the whole domain in three sub-domains $\Omega_1 = [0, 0.2] \times [0, H]$, $\Omega_2 = [0.2, 0.7] \times [0, H]$ and $\Omega_3 = [0.7, L] \times [0, H]$. In Ω_1 and Ω_3 we use the full two-dimensional model as required by the physics of the flow, whereas in Ω_2 the depth-averaged model is used, because here the momentum transfer in the flow depth direction is negligible. This coupled-simulation is an approximation of the full two-dimensional simulation.

Setup I: Undisturbed flow

In Setup I, we consider an undisturbed flow by setting L to a sufficiently large value ($L = 1.5\,\text{m}$). In Fig. 4.3 the simulated velocity field, $|\mathbf{u}| = \sqrt{u^2 + w^2}$, with the coupled 2D/1D/2D model is presented for a time $t = 0.75\,\text{s}$. The flow enters the channel at $x = 0$. The 2D-1D interface is located at $x = 0.2\,\text{m}$ and the 1D-2D interface is located at $x = 0.7\,\text{m}$ (indicated by the grey vertical lines). Both the velocity and the flow depth show smooth transitions at each interface. Although the flow is very shallow in the third subdomain Ω_3, the two-dimensional model is used there, to study the performance of the coupled model for a 1D-2D interface. This becomes important when high momentum transfer in the flow depth direction are expected in this region like in Setup II, where a flow down a channel closed by a perpendicular wall is considered.

The evolution of the velocity vectors with time is shown in Fig. 4.4. There is a strong velocity shearing through the flow depth in the vicinity of the silo inlet in the the Ω_1 (2D) subdomain. With our choice of boundary conditions for the two-dimensional model, shearing through depth is taken into account. This is a big advantage as shearing near the base is not negligible and the usage of an inflow velocity constant

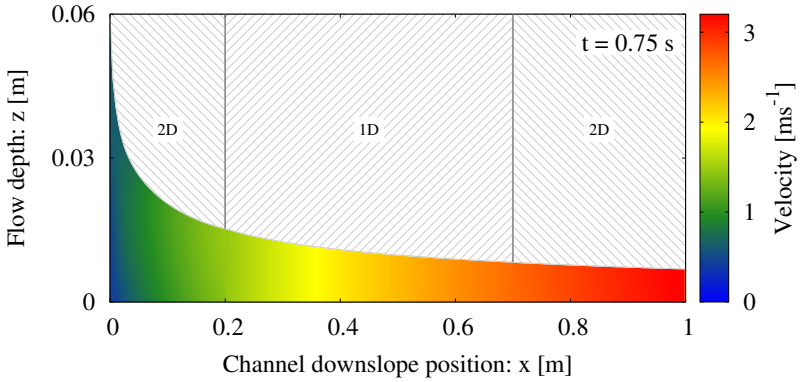

Figure 4.3: Simulation of the velocity field, $|\mathbf{u}| = \sqrt{u^2 + w^2}$, and flow depth of an undisturbed flow with the coupled 2D/1D/2D model. The flow enters the channel at $x = 0$. The 2D-1D interface is located at $x = 0.2\,\mathrm{m}$ and the 1D-2D interface is located at $x = 0.7\,\mathrm{m}$ (indicated by the grey vertical lines).

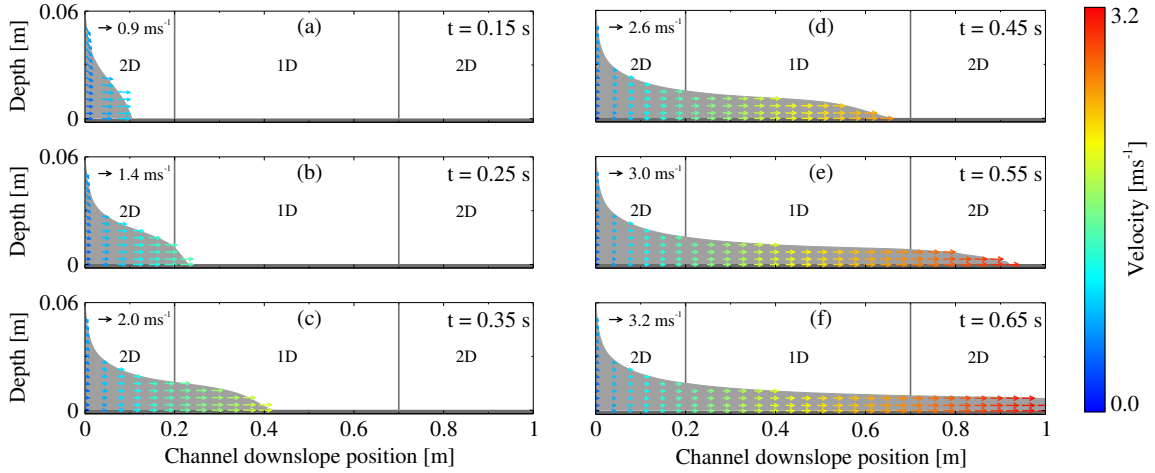

Figure 4.4: Snapshots of velocities (arrows) and depth evolutions (background grey) in rapidly flowing granular material down a steep rectangular open channel simulated with the coupled 2D/1D/2D model.

with depth would not be appropriate at the interface, compare Fig. 4.5. Ultimately, the absence of reflections at the sub-domain boundaries confirms the physical significance of our choice of boundary conditions. In Fig. 4.6 the flow depth and mean (depth-averaged) downslope velocity simulated with the coupled 2D/1D/2D model are compared with ones simulated with the full two-dimensional model. We define the relative error of the coupled simulation by $r = \left|v^{coupled} - v^{2D}\right| / \left|v^{2D}\right|$ for a physical variable v simulated with either the full two-dimensional model (v^{2D}) or the coupled model ($v^{coupled}$). The relative error for the coupled 2D/1D/2D simulation is below 2% for both the flow depth and the mean velocity. This marginal error justifies the coupling of the two-dimensional Coulomb-viscoplastic model with the one-dimensional model, based on the Mohr-Coulomb yield criterion.

Note that although we choose a relatively low value for the viscosity ν, its contribu-

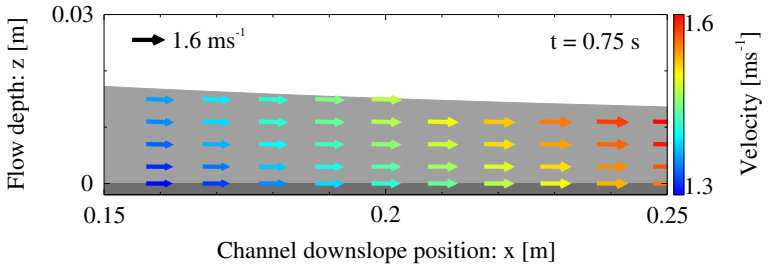

Figure 4.5: Velocity field simulated with the full two-dimensional model around $x = 0.2\,\mathrm{m}$, which corresponds to the 2D-1D interface in the coupled simulation.

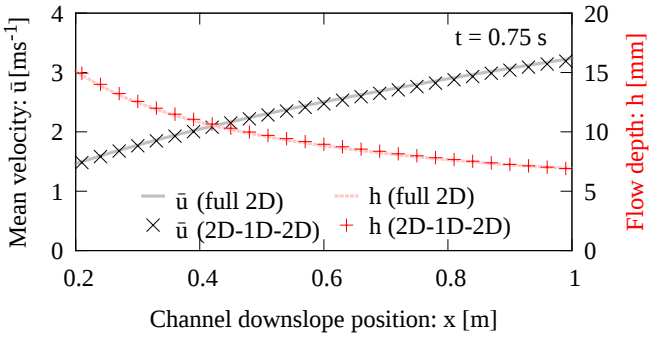

Figure 4.6: Mean downslope velocity and height at $t = 0.75\,\mathrm{s}$ for an undisturbed flow simulated with the full 2D model (lines) and the coupled 2D/1D/2D model (symbols). The 2D-1D interface is located at $x = 0.2\,\mathrm{m}$ and the 1D-2D interface at $x = 0.7\,\mathrm{m}$, respectively.

tion to the effective viscosity ν_{eff} is not negligible. This is exemplarily demonstrated in Fig. 4.7 for the flow near the inlet. Here the ratio of the effective viscosity to the constant viscosity, ν_{eff}/ν, is shown. Figure 4.7 demonstrates that ν_{eff} is of the same order of magnitude as ν for the flow near the inlet. In regions away from the silo gate and close to the free surface, where pressure is small, the effective viscosity is primarily given by ν.

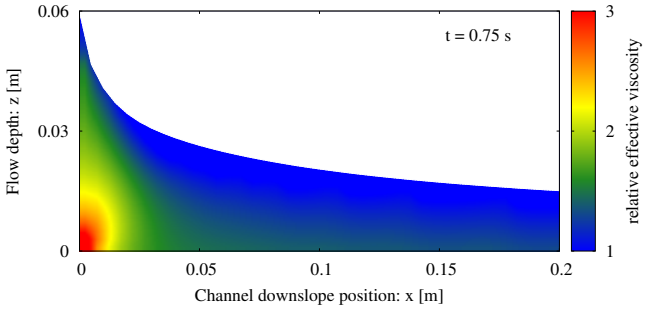

Figure 4.7: Ratio of effective viscosity to constant viscosity, ν_{eff}/ν, near the inlet.

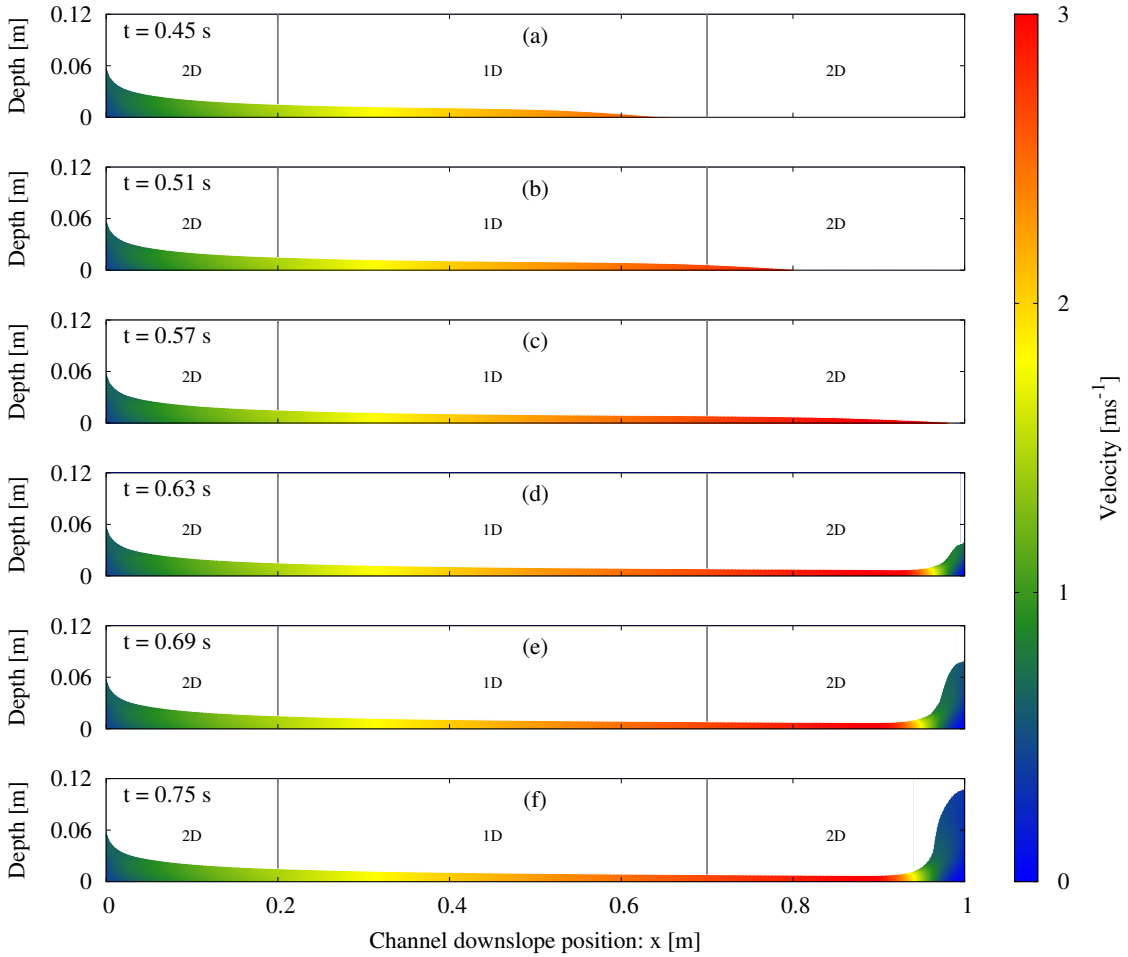

Figure 4.8: Snapshots of the evolution of the velocity, $|\mathbf{u}| = \sqrt{u^2 + w^2}$, and flow depth along the entire channel and simulated with the coupled 2D/1D/2D model. The flow enters the channel at $x = 0$. The 2D-1D interface is located at $x = 0.2\,\mathrm{m}$ and the 1D-2D interface is located at $x = 0.7\,\mathrm{m}$ (indicated by the grey vertical lines). At $x = 1\,\mathrm{m}$ a perpendicular wall is erected.

Setup II: Flow against wall and deposition

A critical point in coupling models of different dimensions is the step moving from the lower dimensional (depth-averaged) model to the higher dimensional (full, non depth-averaged) model as carried out at the 1D-2D interface. It is desired to recapture the higher dimensional properties of the flow on the flow variables when the flow changes its behaviour, e.g., from a supercritical to a subcritical state. This transition is characterised by a substantial momentum transfer in the flow depth direction. This is particularly interesting in view of flows hitting obstacles, where depth-averaging becomes largely inaccurate and a high momentum transfer in z-direction (perpendicular to the channel) evolves. This is demonstrated in Fig. 4.8, where the time evolution of the velocity field, $|\mathbf{u}| = \sqrt{u^2 + w^2}$, and of the flow depth are shown for a granular flow hitting a perpendicular wall. In the following, the behaviour of the granular material

in the vicinity of the wall is considered in more detail.

In Fig. 4.9(a) the velocity field, $|\mathbf{u}| = \sqrt{u^2 + w^2}$, near a perpendicular wall, simulated with the coupled model, is presented at different time steps. As soon as the flow hits the wall it is decelerated and a strong velocity shearing through the depth and along the channel is simulated as observed in experiments (Pudasaini et al., 2007). A deposition region is quickly formed, in which the material is nearly at rest and exhibits solid-like characteristics. In the course of time, the fluidised region, where a strong shearing is observed, shrinks and the deposition region grows, as new arriving material is stopped by the already accumulated, resting mass. Note that we consider here a relatively short time range ($\approx 0.15\,\mathrm{s}$) after the material has hit the wall, where the velocity of the arriving material is still high and hence causes an increasing deposit height at the wall when climbing up the resting material. Fig. 4.9(b) shows the associated pressure field. The dynamic pressure obtains its maximum value, when the flow is hitting the wall, as a result of the extremely strong deceleration of the material near the wall. As in Pudasaini et al. (2007) we define the shock front position as the position, where new arriving mass hits already stopped material. As the shock front position moves in the upstream direction, the pressure decreases slightly with time and is more and more generated by the load of the accumulated material. Note that the pressure distribution along the depth is not linear in the deposit. Hence, it cannot be described by a linear hydrostatic pressure, which is used in classical avalanche and granular flow models. In particular, the hydrostatic pressure underestimates the full dynamic pressure. For example, at $t = 0.75\,\mathrm{s}$ the dynamic pressure at the bottom is $p = 2.3\,\mathrm{kPa}$, and the hydrostatic pressure is calculated as $p_H = 1.0\,\mathrm{kPa}$ (for $h = 0.11\,\mathrm{m}$), which is much smaller than p.

The yield stress is essential in the description of a flow against a wall as a transition of a fluid to a solid state takes place. Here, we considered a pressure-dependent yield stress, which causes the relatively high pressure in the vicinity of the wall to amplify the deceleration of the flow, as the effective viscosity increases. This is not the case for a Bingham-type material (pressure-independent τ_y). In Fig. 4.10 the simulated velocity field, $|\mathbf{u}| = \sqrt{u^2 + w^2}$, and the associated pressure field near a perpendicular wall are shown for a Bingham material with $\tau_y = 100\,\mathrm{Pa}$. The deceleration of the material by the wall is much less compared to a material with a pressure-dependent yield stress (Fig. 4.9(a)). Instead, the wall mainly induces a change of the flow direction to align along the wall. The material climbs up the wall and only a very small deposition region in the corner between the wall and the channel bottom is developed. The pressure (Fig. 4.10(b)) in this region is much higher ($\approx 6\,\mathrm{kPa}$) than the pressure as modelled by a pressure-dependent yield stress material ($\approx 4\,\mathrm{kPa}$, Fig. 4.9(b)). Therefore, a Bingham material shows a completely different flow behaviour when hitting a perpendicular wall as a pressure-dependent yield stress material. This is an evidence for the significance of a pressure-dependent yield stress, used here, in description of a flow hitting a wall. Furthermore, the results for a pressure-dependent yield stress are in line with our physical intuition and some experimental observations (Pudasaini et al., 2007).

In order to investigate the accuracy of the coupled simulation, the depth-averaged

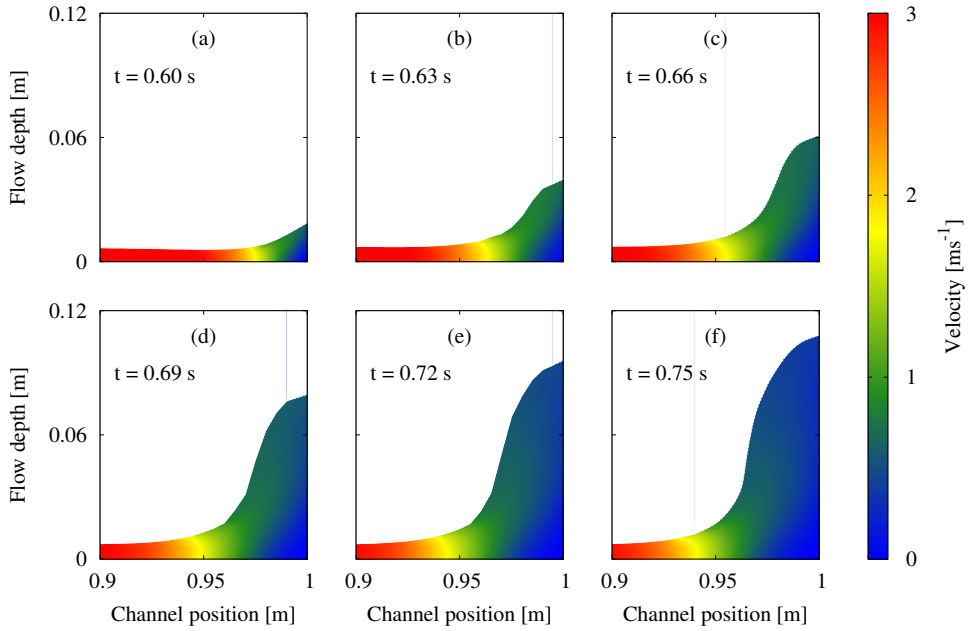

(a) Velocity.

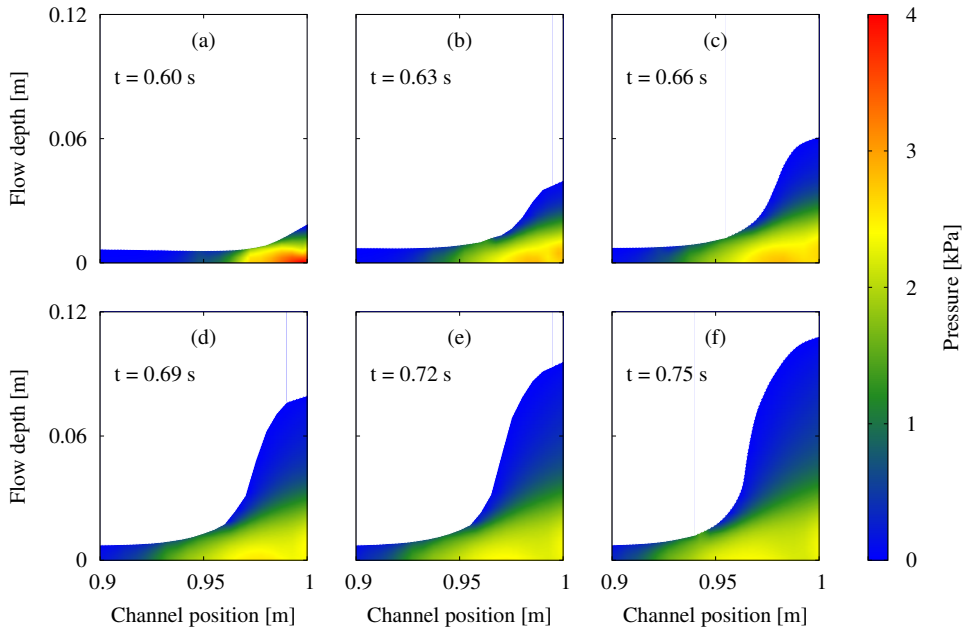

(b) Pressure.

Figure 4.9: Snapshots of the evolution of the velocity, $|\mathbf{u}| = \sqrt{u^2 + w^2}$, pressure p and flow depth in the vicinity of a perpendicular wall erected at $x = 1\,\mathrm{m}$ and simulated with the coupled 2D/1D/2D model for a granular material with pressure-dependent yield stress $\tau_y = \tau_p p$ with $\tau_p = \sin\phi$.

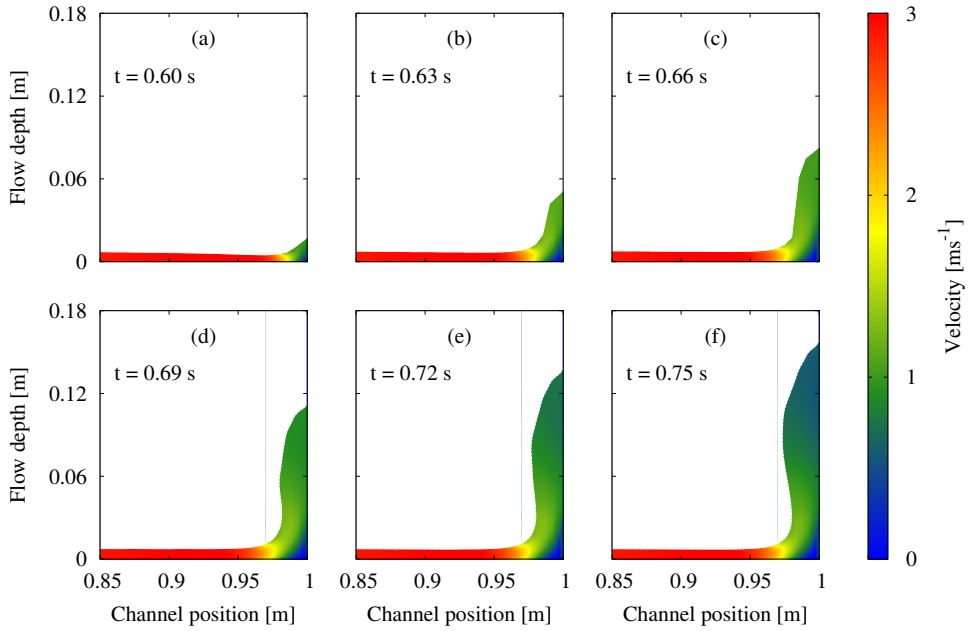

(a) Velocity.

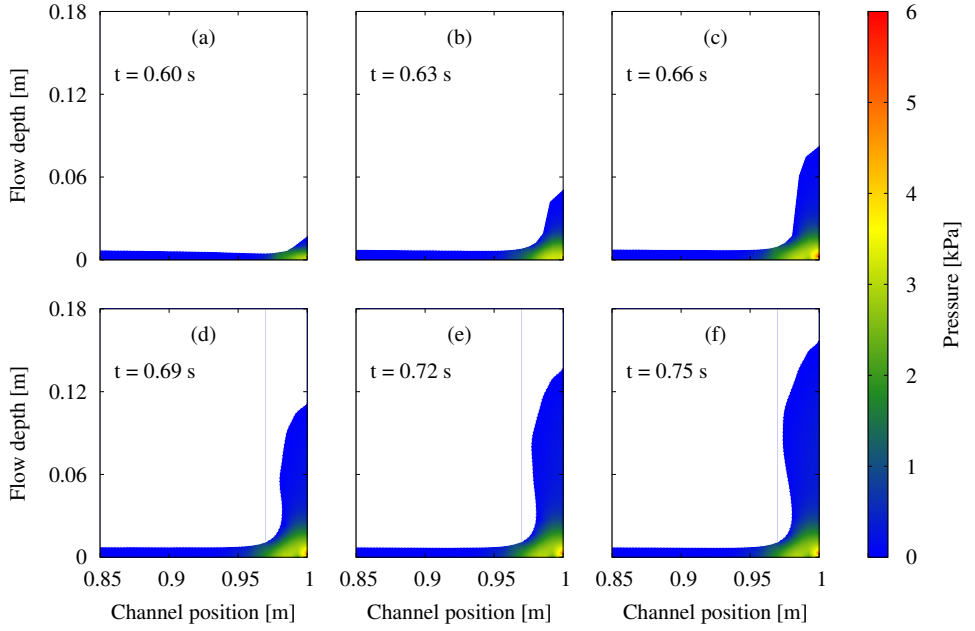

(b) Pressure.

Figure 4.10: Snapshots of the evolution of the velocity, $|\mathbf{u}| = \sqrt{u^2 + w^2}$, pressure p, and flow depth in the vicinity of a perpendicular wall erected at $x = 1\,\mathrm{m}$ and simulated with the coupled 2D/1D/2D model for a Bingham material with a pressure-independent yield stress $\tau_y = 100\,\mathrm{Pa}$.

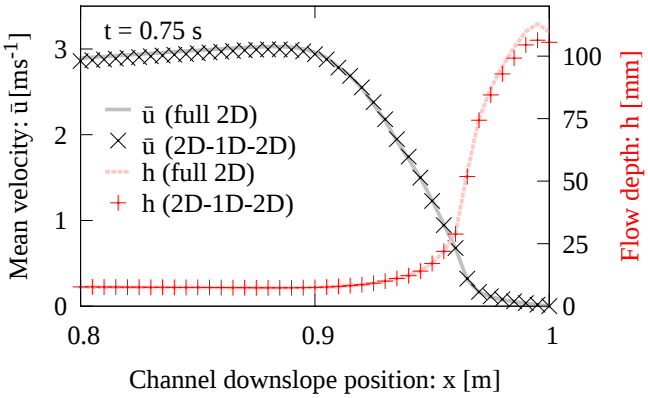

Figure 4.11: Mean velocity and height at $t = 0.75\,\mathrm{s}$ for a flow against a perpendicular wall erected at $x = 1\,\mathrm{m}$, simulated with the full 2D model (lines) and the coupled 2D/1D/2D model (symbols).

(mean) velocity and flow height simulated with the coupled model are compared with the ones simulated with the full two-dimensional model in Fig. 4.11. In vicinity of the wall, the mean velocity decreases rapidly and a shock wave is formed. Both the mean downslope velocity and the flow height, simulated with the full two-dimensional model, are well recaptured by the coupled model. Close to the wall the deviation between the coupled and the full two-dimensional solution increases. This is a consequence of the completely different treatments of the free surface in the 2D and 1D model. In the depth-averaged model the flow height is a field variable, whereas in the full two-dimensional model the free surface is determined by the MAC method. This leads to different descriptions of the front shape of the granular avalanche. Again, Fig. 4.11 demonstrates that our coupling strategy works very well even for sudden changes of flow variables leading to high momentum transfer, energy dissipation and velocity shearing in the flow depth direction.

It is very important to note that by splitting the domain in different subdomains and appropriately using the coupled model instead of a full two-dimensional model, the simulation run-time can be reduced from days to hours for the configurations considered here. The computational cost is mainly affected by the solution of the nonlinear system of equations for the pressure and velocity boundary conditions in the full two-dimensional model, which is very time-consuming for large domains. In general, the running time depends on several factors like grid resolution, domain decomposition, available computing power and more. However, we expect that in most applications the coupled model provides a significant improvement with respect to the computational effort.

Simulation results presented in Figs. 4.9, 4.10, and 4.11 show that the physical-mathematical models and simulation methods adopted and developed here are capable of capturing shock phenomena in rapid granular flows once the flow hits a rigid wall. Another important aspect in our modelling and simulation approach is that, no assumptions are made both in the physical modelling and the numerical simulation scheme in contrast to the depth-averaged modelling and simulation, where a shallow-

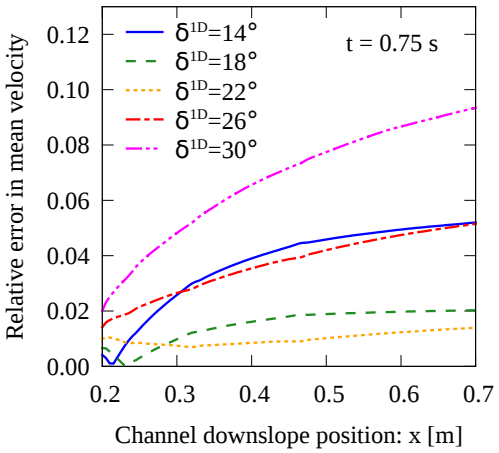

Figure 4.12: Relative error of the mean velocity simulated with the coupled 2D/1D model, where the bed friction angle in the 1D subdomain (δ^{1D}) is set independently of the one in the 2D subdomain ($\delta^{2D} = 22°$).

ness parameter is introduced, hydrostatic pressure, flux limiting and lateral pressure coefficients are assumed. Moreover, full dimensional modelling proposed here avoids the necessity of the inclusion of the earth pressure coefficient as we do not need to close the lateral pressure. Note that in the depth-averaged model simulations, the discontinuity of the pressure coefficient may cause several problems when the flow switches from expanding mode ($\partial_x u > 0$) to diverging mode ($\partial_x u < 0$). The shock-capturing property, the earth pressure coefficient and flux limiting are not required as in depth-averaged modelling, which presents a substantial and genuine advancement.

4.5.2 Correspondence of material parameters

The interaction of the sliding mass with the basal surface is described by the Coulomb friction law for both the two-dimensional and one-dimensional granular flow models, considered here. However, the implementation of this sliding law is completely different for both models. In the full two-dimensional model the Coulomb friction law represents a pressure-dependent velocity boundary condition, which also defines the pressure near the base by complementing the pressure equation (4.9). In the one-dimensional model the Coulomb friction law emerges in the source term due to depth-averaging and defines the net driving acceleration, (4.15). To study the correspondence of the Coulomb friction angle in the two-dimensional model (δ^{2D}) with the friction angle in the one-dimensional model (δ^{1D}), we consider an undisturbed channel flow and split the whole domain in one 2D- and one 1D-subdomain. The two-dimensional model is used in $\Omega_1 = [0, 0.2] \times [0, H]$ and the one-dimensional model is used in $\Omega_2 = [0.2, L] \times [0, H]$. The coupled model is solved numerically with two different bed friction angles. In Ω_1 we assume a bed friction angle of $\delta^{2D} = 22°$ and in Ω_2, where the one-dimensional model is used, we consider different bed friction angles δ^{1D} deviating from δ^{2D}. In Fig. 4.12 the relative error of the mean velocity is considered for different values of $\delta^{1D} = 14°, 18°, 22°, 26°$ and $30°$. It is demonstrated that a deviation of δ^{1D}

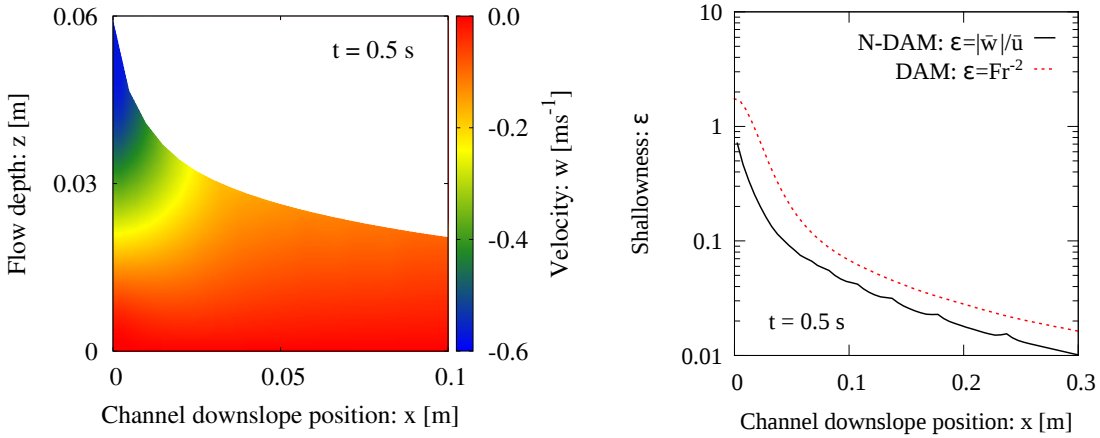

(a) The w velocity in flow depth direction.

(b) Shallowness parameter.

Figure 4.13: Simulation of the velocity component in the flow depth direction (w) and shallowness parameter, ε, in the vicinity of the silo inlet (located at $x = 0$). In the full two-dimensional model (N-DAM) ε is computed by the velocity ratio $|\bar{w}|/\bar{u}$. In the depth-averaged one-dimensional model (DAM) the shallowness parameter is estimated by $\varepsilon = 1/Fr^2$, where Fr is the Froude number.

with respect to δ^{2D} can cause a relative error of several percentages, if the bottom friction in the 1D region is either too strong $\left(\delta^{1D} > \delta^{2D}\right)$ or too weak $\left(\delta^{1D} < \delta^{2D}\right)$. Therefore, we conclude that the bed friction angle used in the one-dimensional model well corresponds to the one in the two-dimensional model. Importantly, this implies that the usage of the Coulomb sliding law in the two-dimensional model is essential. No-slip or free-slip boundary conditions (see Domnik and Pudasaini (2012)) at the basal surface are not appropriate in coupling with the one-dimensional granular flow model used here. Note that both the bed friction angle and the internal friction angle are used in the two- and also in the one-dimensional model to describe the granular nature of the material. However, since the internal friction angle mainly effects the deposit (Pudasaini and Kröner, 2008), where depth-averaging is not appropriate, it does not make any sense to consider a correspondence for the internal friction angle.

4.5.3 Interface location

In the vicinity of the silo inlet there is a high momentum transfer in z-direction due to gravitational acceleration. Figure 4.13(a) shows the simulated w velocities near the silo inlet at $x = 0$. The flow shears and spreads rapidly just below the silo gate, while it remains almost unchanged in the further downstream locations. The shallowness parameter, defined as $\varepsilon = |\bar{w}|/|\bar{u}|$, indicates that close to the silo inlet the w velocity component is of the same order as the u velocity component, Fig. 4.13(b). At some distance from the inlet (few centimetres downstream), the w component becomes negligible. This trend is also confirmed by the shallowness parameter, expressed in terms of the Froude number $\varepsilon = 1/Fr^2$, obtained by a fast simulation of the one-dimensional model for an a priori estimate of the interface position. Note that the shallowness

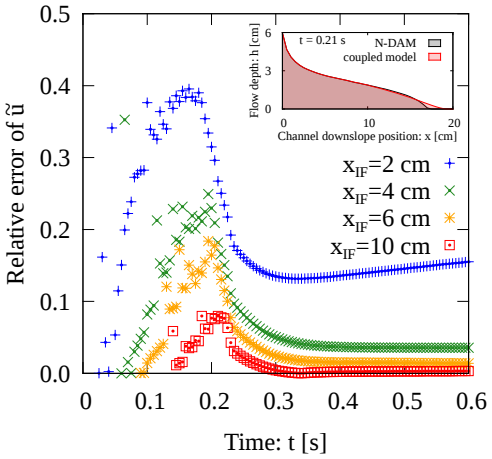

Figure 4.14: Relative error of the globally averaged velocity $\tilde{u}$ evolving with time for different interface positions x_{IF}. In the inset, the flow depth is shown for the coupled and the full two-dimensional model. The 2D-1D interface position of the coupled model in the inset is located at $x_{\text{IF}} = 0.1\,\text{m}$.

parameter appears in the dimensional analysis of the depth-averaged equations and is an ordering parameter. Therefore, the knowledge of its exact value is not required and it is natural that different approaches lead to slightly different results. This explains that the shallowness parameter estimated by the Froude number differs slightly from the one computed by the velocity ratio in Fig. 4.13(b). The important message here is that in regions with high momentum transfer in the flow depth direction, depth-averaging is not valid and the full two-dimensional model must be used.

To study the impact of the interface position, which separates the 2D and 1D model, we simulate the coupled model with different interface positions $x_{\text{IF}} = 2\,\text{cm}, 4\,\text{cm}, 6\,\text{cm}$ and $10\,\text{cm}$. We define the global velocity average by $\tilde{u}(l) = 1/l \int_0^l \bar{u} dx$, where $\bar{u}$ is defined by (4.20). Here, we use $l = 0.2\,\text{m}$, as we focus on the flow in the vicinity of the silo inlet. In Fig. 4.14 the relative error of the averaged velocity $\tilde{u}\,(0.2\,\text{m})$ is presented for different interface positions with respect to time. In the beginning, when the flow passes the respective interface, the relative error is on the order of 10 up to 40 %, depending on the interface position. This error is mainly due to the previously mentioned different front shapes in the 1D and 2D model (compare the simulated flow depth shown in the inset of Fig. 4.14). The one-dimensional model produces a strong diffusive flow front in contrast to the one generated by the MAC method in the two-dimensional model. After some time, the fluid front moves beyond the considered range for averaging and the relative error drops to only few percentages for interface positions $x_{\text{IF}} \geq 4\,\text{cm}$ and to roughly 15% for $x_{\text{IF}} = 2\,\text{cm}$ respectively. Two important observations can be deduced from Fig. 4.14: First, if the interface positions are not appropriately chosen, this can increase the inaccuracy of the coupled simulation dramatically. Second, for appropriately chosen interface locations, the relative error is not increasing with time. This means that the coupled and full two-dimensional model do not diverge with time. By comparing Figures 4.13(b) and 4.14 we conclude that $\varepsilon < 0.1$ is a minimum requirement at the interface position, in order to get a reason-

able accuracy of the coupled simulation. Thus, we suggest to use this requirement in the mentioned a priori estimate of the interface position. However, there is no strict rule for fixing the interface position and it is always a compromise between accuracy of the solution and computational cost.

4.6 Summary

We developed a full two-dimensional Coulomb-viscoplastic model for inclined channel flows of granular material that comes to rest once the flow hits a perpendicular wall in the downstream. The presented model includes the basic features and observed phenomena in dense granular flows like the exhibition of a yield strength and a non-zero slip velocity. We proposed a pressure-dependent yield strength to account for the frictional nature of granular materials. The yield strength is uniquely defined by the internal friction angle of the material and no additional calibration parameter is required as, e.g., for Bingham materials, which is a big advantage. We demonstrated that the pressure-dependent yield strength plays an important role in deposition processes. A Bingham-type material (pressure-independent yield stress) shows a completely different flow behaviour when hitting a perpendicular wall. For this type of flow, the wall mainly induces a change of the flow direction rather a development of a deposition region. In the proposed model, the interaction of the flow with the solid boundary is modelled by a pressure and rate-dependent Coulomb-viscoplastic sliding law. The bed friction angle defines the frictional strength and depends on both the granular material and the boundary substrate. As the sliding law has a substantial impact on the overall flow behaviour, a physically reasonable description of the bottom friction is very essential. Hence, the presented full two-dimensional Coulomb-viscoplastic granular flow model, characterised by the internal and bed friction angle, constitutes a substantial advancement to the existing models.

Additionally, we presented a novel multiscale and multiphysics strategy to couple the full two-dimensional, non depth-averaged model (N-DAM) with a one-dimensional, depth-averaged model (DAM) for rapid motions of frictional granular materials. With the coupled model the computational complexity can dramatically be reduced by using DAM in regions with smooth changes of flow variables. In regions where depth-averaging becomes inaccurate, like in the initiation and deposition regions and particularly, when the flow hits an obstacle or a defence structure, N-DAM must be used. With this, we retain the essential physics of the flow. This is a substantial advantage when considering large scale geophysical mass flows in nature such as snow avalanches, rock avalanches and debris flows. We presented different strategies for a suitable domain decomposition and propose an a priori estimate of the interface position by performing a foregoing, fast simulation with the one-dimensional model. With our choice of boundary conditions at the interfaces, reflections at the sub-domain boundaries can be avoided and the flow variables show a smooth transition at the interfaces. We numerically studied the role of the bed friction angle in both models (N-DAM and DAM). The compatibility of the Coulomb friction laws used in the respective models has been confirmed. We illustrated with examples that the inaccuracy

of the coupled simulation increases substantially if the interface positions are not appropriately chosen. However, there is no strict rule for fixing the interface position and it is always a compromise between accuracy of the solution and computational cost. The performance of the coupling is very high. The numerical results obtained by the coupled model only deviate by few percentages from the ones generated with the full two-dimensional model. This marginal error strongly justifies the coupling of the two-dimensional Coulomb-viscoplastic model with the one-dimensional model, based on the Mohr-Coulomb yield criterion. Remarkably, the run-time of the simulation can be reduced from days (for N-DAM) to hours (for coupled model) for the configurations considered here. We expect that in most applications the coupled model provides a significant improvement with respect to the computational effort, which will be even huge for large scale geophysical flows. In summary, we provide with the coupled model an attractive alternative to an expensive, full two-dimensional model.

Chapter 5

Comparison with Some Experimental Results*

In this chapter, we compare simulation results, obtained by numerically solving the coupled two-dimensional Coulomb-viscoplastic model presented in Chapter 4, with experimental data. As in the previous chapter, we consider a rapid flow of granular material down an inclined channel impinging on a rigid wall in the further downstream, see Fig. 4.1. The flow is continuously fed from a silo, where the silo gate has a height of $h_{\text{in}} = 0.06\,\text{m}$. Behind the silo gate, material with a volume of $V = 15\,l$ is stored, which is suddenly released by opening the gate. After release, material flows down a two metre long channel with an inclination of $\zeta = 50^\circ$ and a width of $w_c = 0.1\,\text{m}$. We demonstrate that the coupled two-dimensional Coulomb-viscoplastic model can reproduce flow velocities and deposits obtained from laboratory experiments. We make use of experimental data presented in Pudasaini et al. (2007), who recorded moving quartz sand particles in the lower half of the channel ($1\,\text{m} \leq x \leq 2\,\text{m}$) with charge coupled devices (CCD) cameras. The particle velocities were measured by using particle image velocimetry (PIV) method.

At first, simulation results of the silo release are presented. The simulated velocities at the silo gate are used to obtain inflow boundary conditions for an inclined channel flow. The simulation results of the inclined channel flow and the deposited material at the wall are then compared with experimental data.

5.1 Simulation of silo release

Before release, the silo contains material with a volume of $V = 15\,l$, which corresponds to a two-dimensional volume of $V^{2D} = V/w_c = 0.15\,\text{m}^2$. The stored material in the silo forms a horizontal surface (Fig. 4.1). Consequently, the stored material extends over a upslope length of $L_s = 0.5\,\text{m}$ and reaches a height of $H_s = 0.6\,\text{m}$ at the front wall of the silo, see the initial configuration at $t = 0$ in Fig. 5.1. (Note that the actual values of H_s and L_s in Fig. 5.1 are slightly smaller, as the simulation assumes

*Domnik, B., Pudasaini, S.P., and Miller, S.A., 2013b. Multiscale coupling of granular flows and comparison with experimental results. In preparation.

Table 5.1: Parameters describing the considered configuration and the material properties. V^{2D} is the two-dimensional initial silo volume, L_s and H_s are the length and the height, respectively, of the initially stored material in the silo, h_{in} is the height of the silo opening gap, L is the channel length, ζ is its inclination, $x_{\text{IF}}^{\text{2D-1D}}$ and $x_{\text{IF}}^{\text{1D-2D}}$ are the 2D-1D and 1D-2D interface positions, respectively, ϕ is the internal friction angle of the granular material, δ is the bed friction angle, ν is the kinematic viscosity and $\varnothing_{\text{grain}}$ is the grain diameter.

silo parameters	channel parameters	material parameters
$V^{2D} = 0.15\,\text{m}^2$	$L = 2\,\text{m}$	$\phi = 33°$
$L_s = 0.5\,\text{m}$	$\zeta = 50°$	$\delta = 22°$
$H_s = 0.6\,\text{m}$	$x_{\text{IF}}^{\text{2D-1D}} = 0.2\,\text{m}$	$\nu = 0.0067\,\text{m}^2\text{s}^{-1}$
$h_{\text{in}} = 0.06\,\text{m}$	$x_{\text{IF}}^{\text{1D-2D}} = 1.8\,\text{m}$	$\varnothing_{\text{grain}} = 4\,\text{mm}$

a smooth surface of the material stored in the deposit.) Due to the relatively small height of the silo gate (compared to L_s and H_s) and a channel inclination of $\zeta = 50°$, a rapid, relatively shallow flow develops in the channel, which requires different spatial and temporal resolutions than the motion of material within the silo. Hence, for technical and computational reasons it is advantageous to obtain the velocity at the silo gate by only considering granular flow in the silo. This velocity can be used as inflow boundary condition in the channel flow simulation.

Pudasaini et al. (2007) measured an internal friction angle of the quartz sand particles of $\phi = 33°$ and a bed friction angle with the channel bottom of about $\delta = 22°$. They do not provide an estimate of the viscosity of the flow. Here, we assume a dynamic viscosity of $\eta = 10\,\text{Pa}\,\text{s}$, which corresponds to a kinematic viscosity of $\nu = 0.0067\,\text{m}^2\text{s}^{-1}$ for a density of $\rho = 1500\,\text{kg}\,\text{m}^{-3}$. This value is within the range of reported viscosities for geophysical mass flows (Takahashi, 1991; Iverson, 1997; Takahashi, 2007). The diameter of the grains is $\varnothing_{\text{grain}} = 4\,\text{mm}$. The parameters describing the material and flow configuration are summarised in Table 5.1.

Figure 5.1 presents the simulated initial release of the stored material in the silo and the subsequent material flow within the silo. The simulation is based on the full two-dimensional model proposed in Section 4.2, which assumes a pressure-dependent yield stress, $\tau_y = \tau_p p$, where $\tau_p = \sin\phi = 0.5446$ for $\phi = 33°$. Friction with the channel boundary and the silo front wall is described by a pressure-dependent Coulomb friction (see Chapter 3 and Chapter 4). In the beginning, all particles are at rest and the granular material inside the silo behaves like a solid ($t = 0$). As soon as the silo gate is opened, the material in the vicinity of the silo gate starts to flow outward and down the channel ($t = 0.025\,\text{s}$). Two regions develop inside the silo: a fluidised region, where the particles move and large shear rates develop, and an immobile, solid-like region, where particles do not move and thus the shear rate is zero. The fluidised region within the silo grows with time, where the main flow direction is aligned along gravity. As time elapses, particles are moving faster and faster inside the silo, at the silo gate, and in the channel. Note that a significant shearing is observed at the silo boundaries as the stored granular material in the silo generates considerable normal

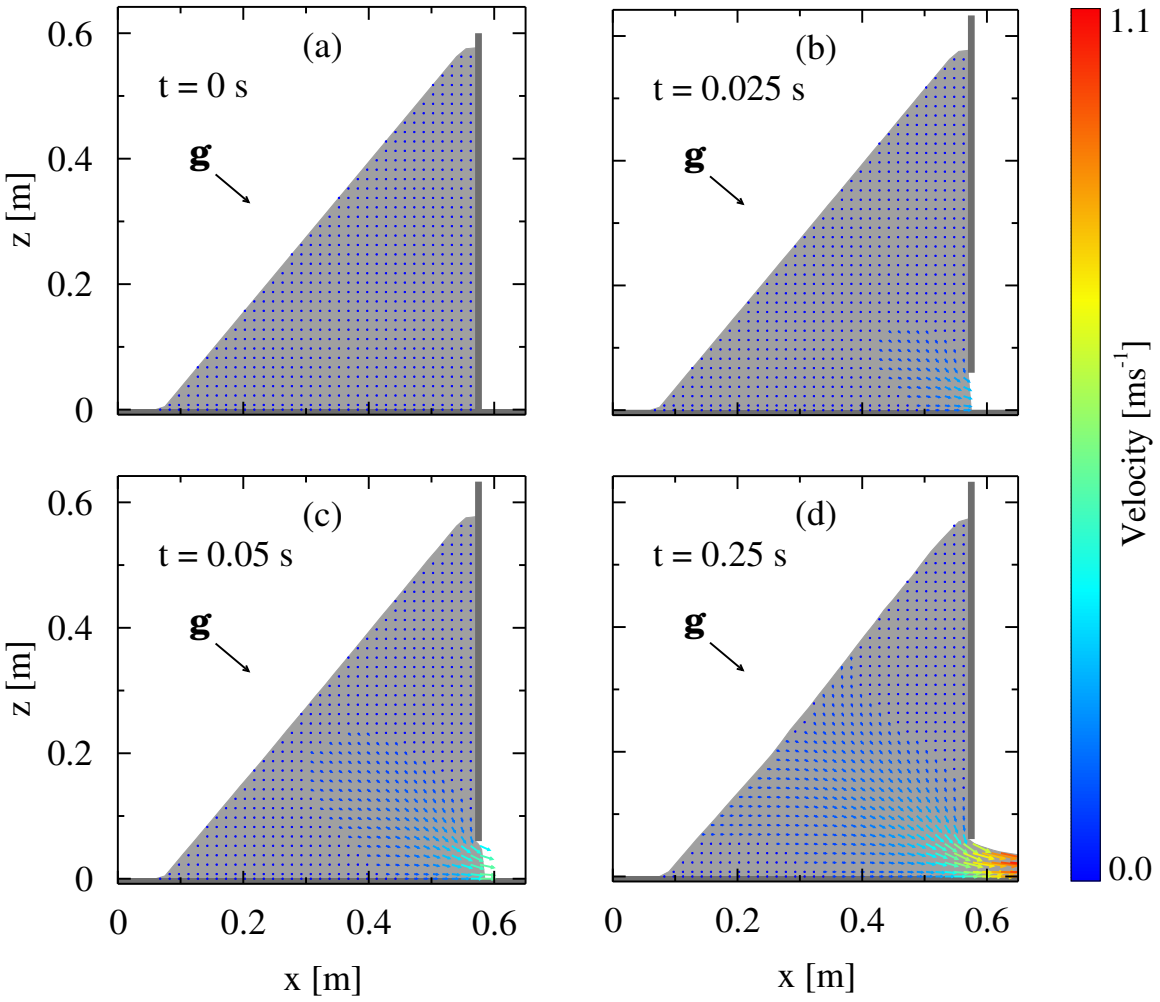

Figure 5.1: Release and flow of granular material stored in an inclined silo, after opening the silo gate. The vectors represent the velocity field and the grey filled area illustrates the area occupied by the granular material. Also shown is the silo front wall located at $x = 0.57\,\mathrm{m}$ and the direction of gravitation.

pressures on the walls. However, the material still slips along the boundaries as observed for granular flows (Massoudi and Phuoc, 2000; Pudasaini et al., 2005c, 2007; Platzer et al., 2007a,b; Pudasaini and Hutter, 2007).

Motion of granular materials within a silo are most often modelled by discrete element methods (DEM) (Yang and Hsiau, 2001; Sykut et al., 2008; González-Montellano et al., 2011), which are still restricted to small scale simulations even if simulation capabilities are growing fast. Our simulation results demonstrate that the proposed continuum model can successfully describe the motion of a granular material within a silo in laboratory scale, including solid-liquid transitions and (pressure-dependent) slip velocities at the silo boundaries, with moderate computational effort.

An enlarged view of the velocities at the silo gate is presented in Fig. 5.2. At the silo gate ($x = 0.57\,\mathrm{m}$) a strong shearing of the downslope velocity, u_{out}, both at the silo front wall and at the bottom surface is observed. In the further downstream, the

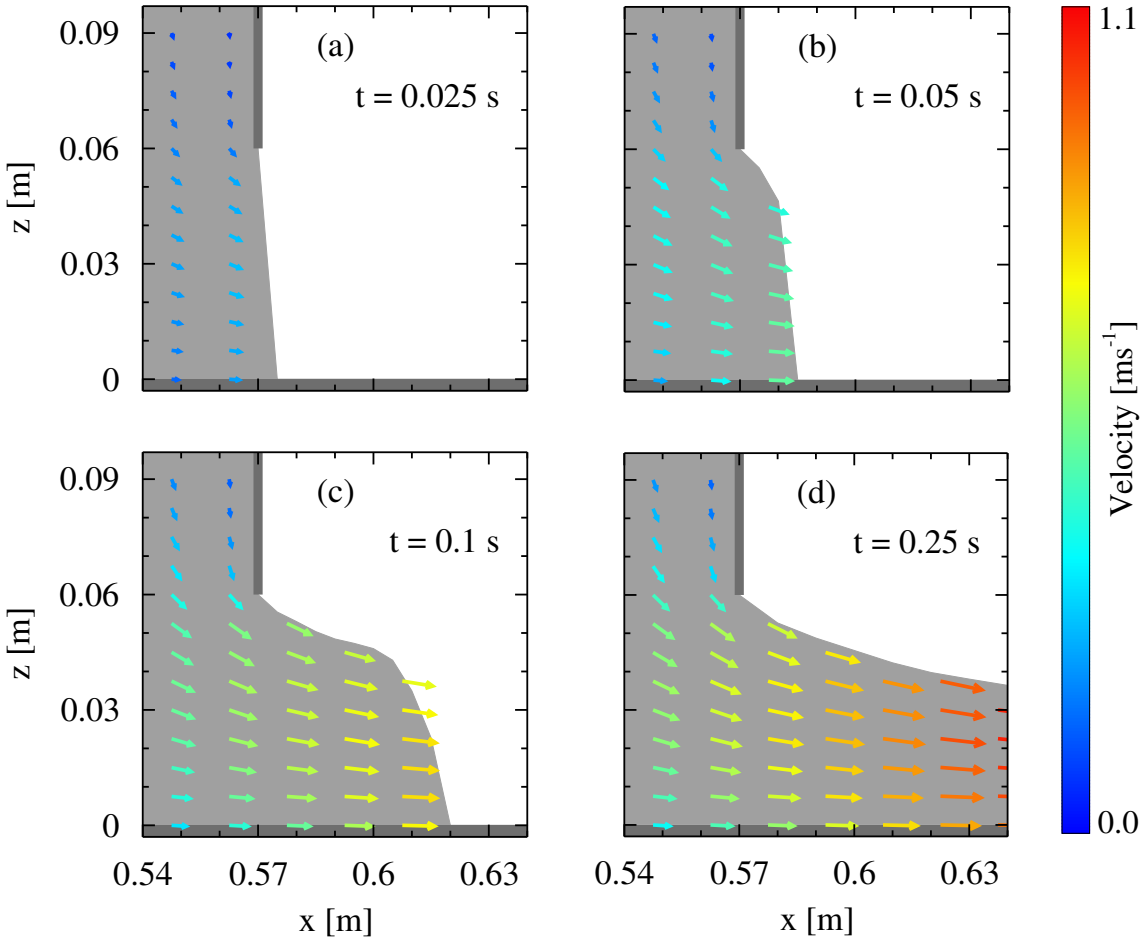

Figure 5.2: Simulated velocity field in the vicinity of the silo gate, which is located at $x = 0.57\,\mathrm{m}$. The vectors represent the velocity field and the grey background represents the area occupied by the granular material.

velocity quickly becomes largest at the free surface and smallest at the bottom due to friction ($t = 0.25\,\mathrm{s}$). The simulation results reveal that u_{out} varies both with time and flow depth. However, Fig. 5.2 also indicates that after some time, the temporal variations diminish. This is confirmed by Fig. 5.3, in which the time evolution of the outflow velocity is shown both for its depth-average and its distribution through the depth. The increase of the depth-averaged outflow velocity, $\bar{u}_{\mathrm{out}}$, with time can be described by an exponential function, $\bar{u}_{\mathrm{out}}(t) = e_1\,(1 - \exp\,(-e_2 t))$ with $e_1 = 0.62$ and $e_2 = 10.73$, Fig. 5.3(a). For $t > 0.2\,\mathrm{s}$, $\bar{u}_{\mathrm{out}}$ varies only slightly with time and is approximately a constant. However, shortly before the silo becomes empty, a time dependency of $\bar{u}_{\mathrm{out}}$ may be observed again. This is not considered here, as the whole silo discharge takes several seconds. A clear and strong shear profile of the outflow velocity is observed in Fig. 5.3(b). After a time $t_f \approx 0.05\,\mathrm{s}$, the flow front passes the silo gate, and the Coulomb friction law generates a strong shearing at the bottom surface. However, for $t \leq t_f$ the flow front is still located close to the silo gate, and the bottom shear stress vanishes at this point due to the free-surface condition.

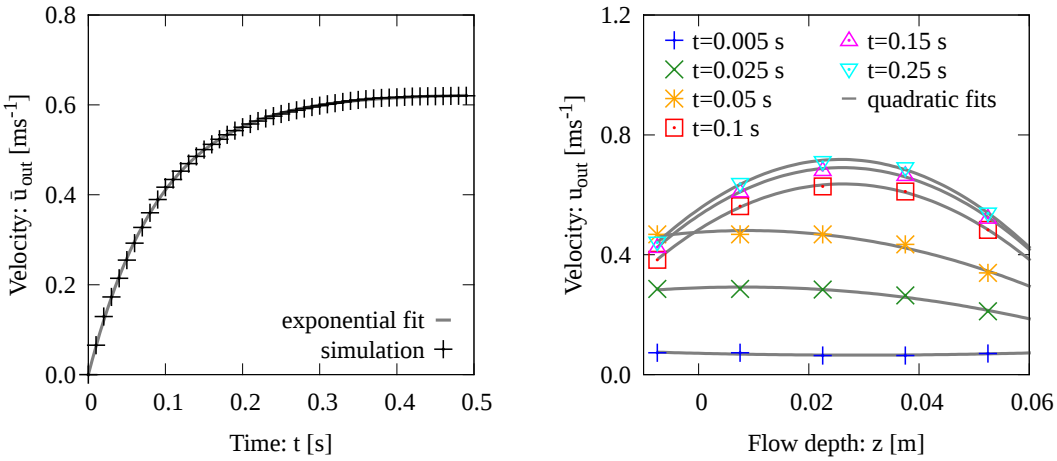

(a) $\bar{u}_{\text{out}}(t)$. (b) $u_{\text{out}}(z,t)$.

Figure 5.3: Time evolution of the outflow velocity at the silo gate: (a) depth-average, and (b) distribution through the depth.

The velocity distribution through the depth can approximately be described by a quadratic power law (parabola) with time-dependent parameters, $u_{\text{out}}(z,t) = q_0(t) + q_1(t)z - q_2(t)z^2$, as demonstrated by quadratic fits in Fig. 5.3(b). This is a consequence of the relatively strong velocity diffusion along the flow depth, as the silo front wall and the friction at the channel bottom cause a considerable shearing of the outflow velocity. In Fig. 5.4 the outflow velocity coefficients $q_i(t)$ ($i \in \{1,2,3\}$) are presented, where $q_i(t)$ are obtained by fitting $u_{\text{out}}(z)$ at different times t like in Fig. 5.3(b). For $t \leq t_f$, the variation of the outflow velocity coefficients with time can be described by a linear relationship, $q_i(t) = l_{0,i} + l_{1,i}t$. For $t > t_f$, an exponential function, $q_i(t) = e_{0,i} + e_{1,i}\left(1 - \exp\left(-e_{2,i}t\right)\right)$, can be fitted to the simulation data. This describes the reducing variations of u_{out} with time as already observed for the depth-averaged outflow velocity. The linear and exponential fit parameters describe the outflow velocity $u_{\text{out}}(z,t)$ completely and can be used to determine an inflow boundary condition in channel flow simulations. Their values are listed in Table 5.2 and Table 5.3.

5.2 Inclined channel flow

We consider a rapid flow of granular material down an inclined channel and impinging on a rigid wall, which is numerically solved with the coupled model presented in Chapter 4. In regions where depth-averaging may become inaccurate, like in the initiation (in the vicinity of the silo gate) and deposition regions (in the vicinity of the rigid wall), the full two-dimensional, non depth-averaged model (N-DAM) is used. The depth-averaged, one-dimensional granular flow model (DAM) is used in between, where the momentum transfer in flow depth direction is negligible. Driven by geometrical considerations and the results presented in Section 4.5.3, we choose a 2D-1D interface position of $x_{\text{IF}}^{\text{2D-1D}} = 0.2\,\text{m}$ and a 1D-2D interface position of $x_{\text{IF}}^{\text{1D-2D}} = 1.8\,\text{m}$.

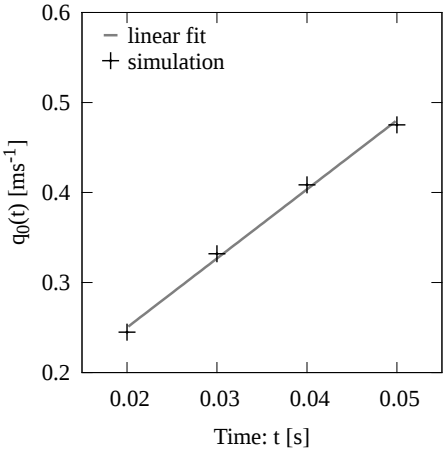

(a) $q_0(t)$ for $t \leq t_f$.

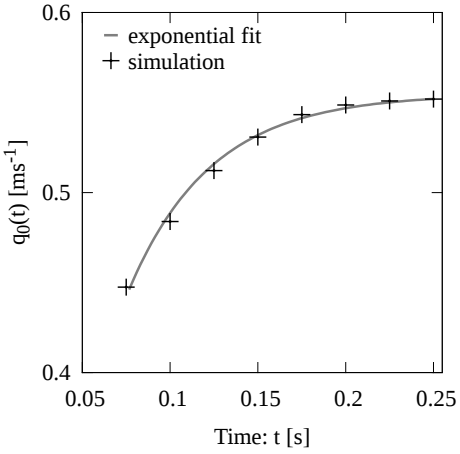

(b) $q_0(t)$ for $t > t_f$.

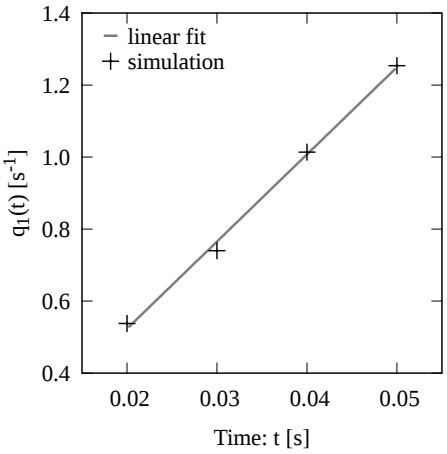

(c) $q_1(t)$ for $t \leq t_f$.

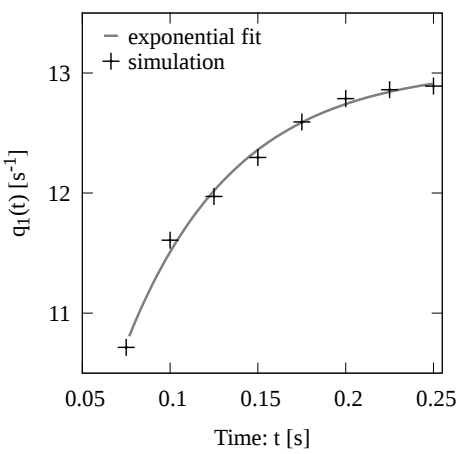

(d) $q_1(t)$ for $t > t_f$.

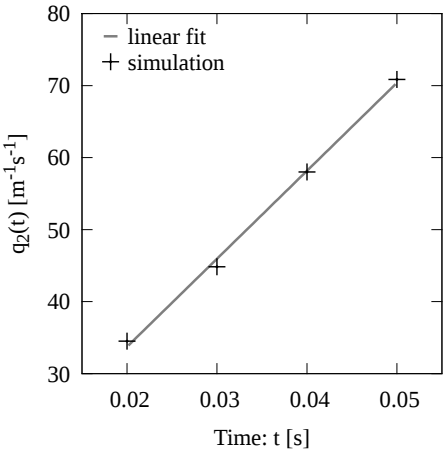

(e) $q_2(t)$ for $t \leq t_f$.

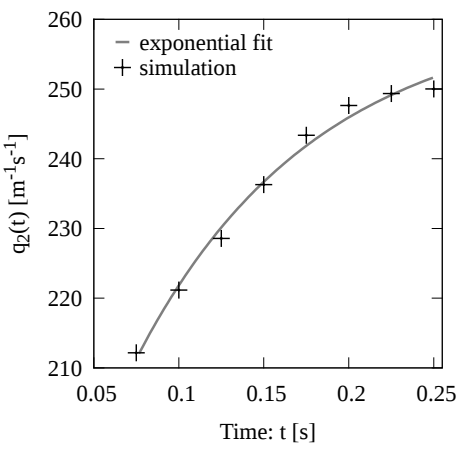

(f) $q_2(t)$ for $t > t_f$.

Figure 5.4: Inflow velocity coefficients $q_i(t)$ obtained by fitting $u_{\text{out}}(z)$ at different times t (symbols) and their linear ($t \leq t_f$) and exponential ($t > t_f$) fits (lines).

Table 5.2: Linear fit parameter $l_{0,i}$ and $l_{1,i}$ describing the outflow velocity coefficients $q_i(t)$ for $t \leq t_f$.

	$l_{0,i}$	$l_{1,i}$
$i = 0$	$0.097\,\mathrm{ms}^{-1}$	$7.67\,\mathrm{ms}^{-2}$
$i = 1$	$0.039\,\mathrm{s}^{-1}$	$24.21\,\mathrm{s}^{-2}$
$i = 2$	$9.296\,\mathrm{m}^{-1}\mathrm{s}^{-1}$	$1221.73\,\mathrm{m}^{-1}\mathrm{s}^{-2}$

Table 5.3: Exponential fit parameter $e_{0,i}$, $e_{1,i}$, and $e_{2,i}$ describing the outflow velocity coefficients $q_i(t)$ for $t > t_f$.

	$e_{0,i}$	$e_{1,i}$	$e_{2,i}$
$i = 0$	0	$0.56\,\mathrm{ms}^{-1}$	$21.27\,\mathrm{s}^{-1}$
$i = 1$	$5.36\,\mathrm{s}^{-1}$	$7.69\,\mathrm{s}^{-1}$	$16.08\,\mathrm{s}^{-1}$
$i = 2$	$159.57\,\mathrm{m}^{-1}\mathrm{s}^{-1}$	$101.56\,\mathrm{m}^{-1}\mathrm{s}^{-1}$	$9.50\,\mathrm{s}^{-1}$

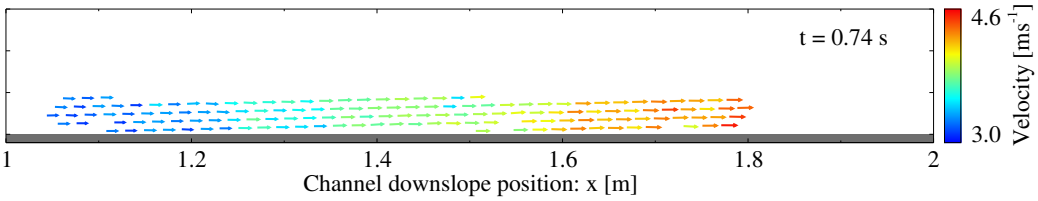

(a) PIV data.

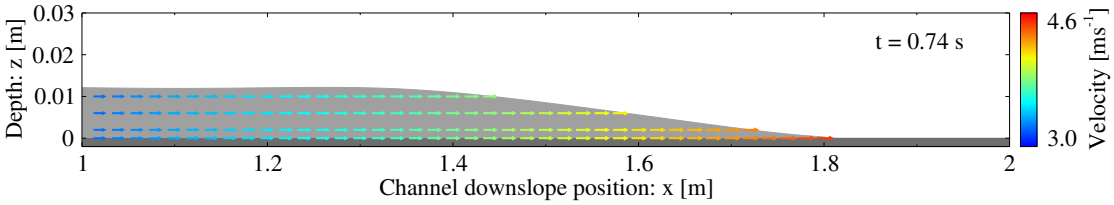

(b) Simulation.

Figure 5.5: Velocity field in the lower half of the channel at $t = 0.74\,\mathrm{s}$ obtained from the PIV measurements (Pudasaini et al., 2007) (a) and the simulation (b). In (a) the z-direction is not in scale.

Hence, a relatively long part of the channel is described by DAM and the computational complexity and time can dramatically be reduced with the coupled model by retaining all the basic physics of the flow (Domnik et al., 2013a). The inflow velocity $u_{\mathrm{in}}(z,t)$ is assumed to vary quadratically with flow depth and linear-exponentially with time as obtained from the silo simulation presented in the previous section.

Figure 5.5(a) presents the experimental velocities obtained with particle image velocimetry technique (Pudasaini et al., 2005c; Pudasaini and Hutter, 2007). Here, we

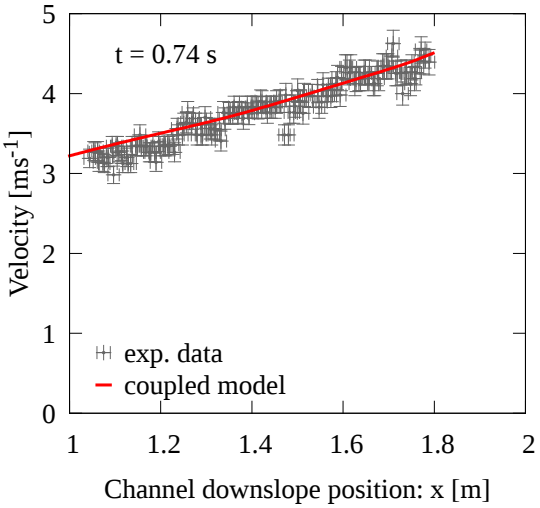

Figure 5.6: Comparison of simulated flow velocities along the channel with experimental data (Pudasaini et al., 2007) at $t = 0.74\,\mathrm{s}$.

consider $t = 0.74\,\mathrm{s}$, for which the material has not yet hit the front wall and the depth of the very shallow flow could not accurately be detected by the CCD cameras. These experimental observations are simulated in Fig. 5.5(b). The simulation well reproduces the front position and the velocity magnitudes including their growth along the channel. In Fig. 5.6 the simulated velocity magnitudes (here corresponding to the depth-averaged downslope velocities) along the channel are directly compared with experimental data. Pudasaini et al. (2007) reported a total error of the velocity of 3.63 % and a possible error in length of 0.0125 m, which define the size of the errorbars in Fig. 5.6. We observe a very good agreement of the simulated velocities with the experimental data.

Figure 5.7 compares the simulated deposit with deposit heights obtained by digitising a CCD photograph (from Pudasaini et al. (2007)) at $t = 1\,\mathrm{s}$. As the physical dimensions of the photograph are not exactly known and the available photographs have a limited optical resolution, the error of deposit depths and channel positions is expected to be considerable. This is indicated by the error bars in Fig. 5.7, which represent a resolution error of 1 cm. Within this resolution, a good agreement of the simulation with the experimental data is observed. Both the timing and the characteristic s-shape of the deposition, which is the upward propagating shock front, are very well reproduced by the simulation.

5.3 Summary

By using a full two-dimensional Coulomb-viscoplastic model with pressure-dependent yield strength, we numerically studied the release of granular material stored in an inclined silo through an opening gate. The material slips along the silo boundaries and the channel bottom according to a Coulomb friction law. We demonstrated that the proposed continuum model can successfully describe the motion of a granular material

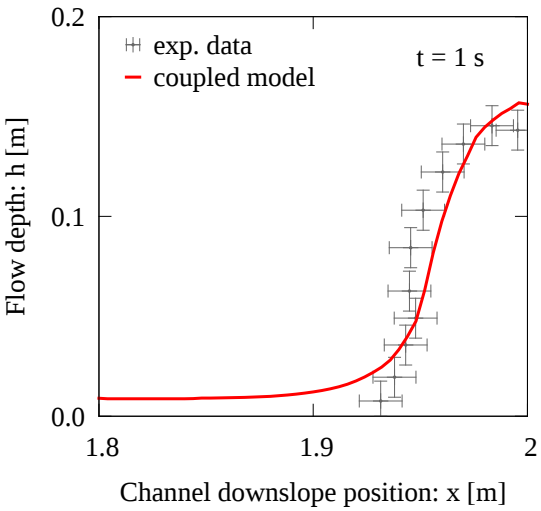

Figure 5.7: Comparison of simulated deposit depth with experimental data (Pudasaini et al., 2007) at $t = 1\,\mathrm{s}$.

within a silo, including solid-liquid transitions and (pressure-dependent) slip velocities at the silo boundaries. Inside the silo, we observed two regions: a fluidised region, where the particles move and large shear rates develop internally and along the silo boundaries, and an immobile, solid-like region, where particles do not move. As time elapses, the fluidised region grows and the solid-like region shrinks. Furthermore, the simulation results demonstrate a strong shearing of the outflow velocity at the opening gate, which is caused by the silo front wall and friction at the bottom surface. The distribution through the depth of the outflow velocity can be described by a quadratic law with time-dependent parameters. This time dependency is mainly exponential and after about 0.2 s a nearly constant outflow velocity is observed (constant with respect to time). We used these outflow velocities to describe the inflow boundary conditions for an inclined channel flow impinging on a rigid wall erected perpendicularly at the end of the channel. The channel flow was simulated by numerically solving a coupled two-dimensional Coulomb-viscoplastic model. The strategy of the coupled model is to apply a full two-dimensional model in the vicinity of the silo gate and the rigid front wall, and a depth-averaged, one-dimensional granular flow model in between. As a relatively long part of the channel could be described by the depth-averaged model, the computational complexity and time was dramatically reduced with the coupled model by retaining all the basic physics of the flow.

We demonstrated that the simulation results for the flow velocities and deposit heights agree very well with experimental observations presented in Pudasaini et al. (2007). The simulation of the channel flow well reproduces the flow front position and the velocity magnitudes including their growth along the channel. When the flow hits the front wall, material deposits with a characteristic s-shape of the deposition, which is also well reproduced by the simulation. Here, we did not consider the evolution of the deposition for larger times, since long time simulations are very time consuming as more and more material accumulates at the wall. In general, simulations of deposition

processes require high temporal and spatial resolutions, as the flow impinging on the deposit is very shallow and undergoes a strong and rapid deceleration. Further experimental results for rapid granular flows and their comparisons with numerical simulations can be found in Kröner (2013). The simulation results presented in this chapter and their very good agreements with experimental data imply that the proposed full two-dimensional Coulomb-viscoplastic model, including its numerical solution and its coupling to DAM, is able to describe gravity driven rapid granular flows.

Chapter 6

Energy Associated with Rapid Granular Flows*

We present a complete expression for the total energy associated with a rapid frictional granular shear flow down an inclined surface. This expression reduces to the often used energy for a non-accelerating flow of an isotropic, ideal fluid in a horizontal channel, or to the energy for a vertically falling mass. We utilize thickness-averaged mass and momentum conservation laws written in a slope-defined coordinate system. Both the enhanced gravity and friction are taken into account in addition to the bulk motion and deformation. The total energy of the flow at a given spatial position and time is defined as the sum of four energy components: the kinetic energy, gravity, pressure and the friction energy. Total energy is conserved for stationary flow, but for non-stationary flow the non-conservative force induced by the free-surface gradient means that energy is not conserved. Simulations and experimental results are used to sketch the total energy of non-stationary flows. Comparison between the total energy and the sum of the kinetic and pressure energy shows that the contribution due to gravity acceleration and frictional resistance can be of the same order of magnitude, and that the geometric deformation plays an important role in the total energy budget of the cascading mass. Relative importance of the different constituents in the total energy expression is explored. We also introduce an extended Froude number that takes into account the apparent potential energy induced by gravity and pressure.

6.1 Introduction

There is a wide spectrum of applications for granular flow, ranging from large-scale snow, rock or debris avalanches in nature, to small scale transport of granular materials in industrial handling and production processes. The energy associated with such flows is a major concern to avalanche dynamicists with respect to avalanche defense, hazard mitigation and planning. Estimation of the total energy carried out by the avalanching mass is important for civil engineers in designing structures and spacing

*This chapter is based on: Pudasaini, S.P. and Domnik, B., 2009. Energy considerations in accelerating rapid shear granular flows. Nonlinear Processes in Geophysics, 16(3):399–407.

because they must withstand at least the total destructive power of the avalanche. As an example, cone-shaped earthen mounds are frequently built in the lower part of the track and the run-out zone to retard and dissipate the destructive power of an avalanche by absorbing its energy from reducing velocity and shortening its flow path. Thus, the avalanche stops before it reaches the area needing protection (Rao, 1985; Pudasaini and Hutter, 2007). Simple energy balance is often used to determine the runout efficiency of the events. To analyze basic features, like the horizontal displacement L and the vertical height drop H, the energy conservation in the rigid mass model (Heim, 1932) is still widely used (Hsu, 1975; Ui, 1983; Erismann and Abele, 2001). In this simple model a single block with mass m steadily slides down an incline with uniform basal friction. A comparison of the energy at the beginning and end of the motion leads to the equation $gmH = W$, with the gravitation constant g and the work W done by friction. By assuming Coulomb friction, $F = \mu mg$, where μ is the effective coefficient of friction, one obtains $H/L = \mu$, whose reciprocal is a measure of the efficiency of mass movement (Ward and Day, 2006). This simple expression can be used to get information about flow characteristics without requiring the full equations of motion or determining the friction parameters from the experimental or field observation.

Recently, the energy mechanics of geophysical mass flows has attracted interest. Gwiazda (2005) considered kinetic and pressure energies for avalanche flows. Similarly, Fine et al. (2003), Castro et al. (2006) and Dutykh and Dias (2009) addressed the kinetic and gravitational energy for tsunami waves. Jin and Wen (2004) and Noelle et al. (2006, 2007) took into account the kinetic, gravitational and pressure energies for steady state shallow water flow in Cartesian coordinates with a lake at-rest conditions. However, none of these papers involves the role of the dissipative frictional resistance, and thus the entire energy of the flow was not considered. Bartelt et al. (2005, 2006) and Buser and Bartelt (2009) studied the energetics of snow avalanches by showing how frictional processes taking place at the basal surface are related to dissipative mechanisms within the avalanching body. They wrote an energy balance for thickness averaged flows, including the production of kinetic energy associated with the random movement of the snow granules; however, they always assumed a constant flow height and steady-state flow. Thus, they were not able to deduce how changes in flow height affected the overall energy balance and therefore the production of random energy.

In this chapter, we focus on the general aspects of deformable avalanching mass rapidly sliding down a slope and the associated total energy budget carried out by the flow. We attempt to answer the question of how frictional dissipation and the gravity acceleration are linked to spatial variations in flow height and the flow velocity. To do so, we first rewrite the thickness averaged frictional granular flow equations (Savage and Hutter, 1989; Pudasaini and Hutter, 2003, 2007) in terms of a single state variable, the flow height, following Le Roux (1998). For such equations, internal deformations, which are assumed to be governed by an earth pressure coefficient, can be directly related to spatial variations of the flow height. We then present a complete total energy function for accelerating rapid granular flows that is applicable for a non-steady

deformable mass sliding down inclines. Our energy expression takes into account all contributing factors, including kinetic energy, pressure potential, gravitational potential and the thermal energy due to frictional heat. The energy equation shows how variations in flow height and the net driving acceleration influence the overall energy distribution of granular masses sliding down inclines. Our analysis does not restrict itself to purely steady flows and therefore we can use the derived energy relations to constrain constitutive models for granular flows. We demonstrate that the contribution of the gravity potential and friction energies, collectively induced by the net driving acceleration, plays a crucial role in determining the total energy. In a series of simulations, we then show how and under which conditions, the term governing the internal deformations, bulk motions and the net driving acceleration of the system influence the total energy balance.

6.2 Frictional granular flow equations

As in Section 4.3, we consider one-dimensional frictional granular flow equations with Coulomb basal sliding law to describe incompressible rapid shear granular flows down inclined channels (Savage and Hutter, 1989; Gray et al., 1999; Pudasaini and Hutter, 2003; Pudasaini et al., 2005b; Pudasaini and Hutter, 2007; Pudasaini et al., 2008). These are thickness-averaged balance laws of mass and momentum in slope-fitted coordinates in the form of non-linear hyperbolic partial differential equations:

$$\begin{aligned} \frac{\partial h}{\partial t} + \frac{\partial}{\partial x}(hu) &= 0\,, \\ \frac{\partial}{\partial t}(hu) + \frac{\partial}{\partial x}\left(hu^2 + \frac{1}{2}\beta h^2\right) &= g\cos\zeta\,(\tan\zeta - \tan\delta)\,h, \end{aligned} \tag{6.1}$$

where h is the flow depth, u the velocity parallel to the sliding surface, ζ the channel slope angle, $\tan\delta$ the coefficient of friction, g the magnitude of gravitational acceleration, $\beta = gK\cos\zeta$ and $K = 2\sec^2\phi\left(1 \mp \sqrt{1-\cos^2\phi\sec^2\delta}\right) - 1$ is the earth pressure coefficient. This coefficient is a function of the internal (ϕ) and basal (δ) angles of friction that are active during extensional motion (upper sign) and passive during compressional motion (lower sign). The right-hand side of the momentum balance in (6.1) contains the net driving acceleration $s = g\cos\zeta\,(\tan\zeta - \tan\delta)$, which can be split into the acceleration due to gravity, $s_g = g\sin\zeta$, and the resistance due to friction, $s_f = -g\cos\zeta\tan\delta$. K and s incorporate the internal interaction of the media with itself and its interaction with the basal surface. Note that s is the source term, which makes the system of equations inhomogeneous. If the gravity is exactly balanced by friction, the mass is only subject to internal deformation as modeled by the term $\partial(0.5\beta h^2)/\partial x$, which corresponds to the pressure gradient induced by the free surface and the anisotropy (normal stress effect) in the granular material.

Rapid shear flows

The flows of granular material down a silo gate, or in the form of dam-break flows, are essentially rarefied flows (Mangeney et al., 2000; Pudasaini et al., 2005a, 2007). One

particularly interesting case is the granular flow down a steep rectangular chute, where the material is uniformly fed from the silo gate (Pudasaini and Kröner, 2008). In such a situation the velocity can be expressed locally as a function of the flow depth, i.e., $u = u(h)$. This simplifies the situation and reduces the number of field variables from two to one, namely, the flow depth. With this, (6.1) takes the form ($u' = du/dh$):

$$\begin{pmatrix} 1 & hu' + u \\ hu' + u & 2hu'u + u^2 + \beta h \end{pmatrix} \begin{pmatrix} \partial h/\partial t \\ \partial h/\partial x \end{pmatrix} = \begin{pmatrix} 0 \\ sh \end{pmatrix}. \tag{6.2}$$

Since the flow is driven by the net driving acceleration, the entire analysis depends on the parameter s. Depending on whether it is zero, positive or negative, the flow as a whole would be non-accelerating, accelerating or decelerating, respectively. However, in each case the individual particles may accelerate or decelerate due to the free surface gradient. Here, the classical (original) shallow water or Saint-Venant (1871) equations differ from our equations (Bouchut et al., 2003; Rudenko et al., 2007). In the shallow water model, the momentum transfer is only due to the free-surface (hydraulic) gradient of the flow. The model equations (6.1) reduce to the shallow water equations if $K = 1$ and $\zeta = \phi = \delta = 0$, which implies that the net driving force vanishes.

6.3 Total energy in rapid granular flows

Le Roux (1998) derived an energy function for non-homogeneous shallow-water equations which were written in Cartesian (horizontal-vertical) coordinates. The non-homogeneity emerges from the bottom elevation as measured from a horizontal datum. A ramp between two horizontal steps with two singularities is defined, on which rarefaction (thinning of the medium depth) of the flow takes place. No basal friction is considered. Therefore, the flow is driven by the free-surface (pressure) gradient and the gradient of the bottom elevation, which is treated as the source term. Although Le Roux did not derive the total energy for this situation (he neglected the potential energy due to gravity and the internal energy induced by friction) this concept is still useful. If the flow takes place in a steep slope, simulations produce better results when coordinates are defined by the slope instead of Cartesian coordinates. Therefore, we defined the coordinates along the slope and normal to it. As a consequence we do not need to consider the bottom elevation function that was treated before as the source term by Le Roux. Instead, the source term is composed of the gravity component along the channel minus the Coulomb friction, which has not yet been considered. In the present analysis, rarefaction can take place down the entire plane. We closely follow Le Roux (1998).

6.3.1 Introduction of the energy function

Absence of the net driving force

We start our analysis of a system when $s = 0$. Since $h \neq 0$, the matrix in (6.2) is necessarily singular, so the corresponding determinant must vanish, implying:

$$h(u')^2 - \beta = 0. \tag{6.3}$$

This is an exact ordinary differential equation, which can be solved to yield $u \pm 2\sqrt{\beta h} = \Lambda$, where Λ are constants of integration. These are Riemann invariants and remain constant along the flow characteristics $dx/dt = u \pm c$, where $c = \sqrt{\beta h}$ is the wave celerity. There is some experimental evidence that (6.3) has some validity. By applying geometric arguments, Bartelt et al. (2007) also derived a similar relationship between h and u, more precisely, $h \propto u^2$. They compared this formula to actual granular flows and showed how the tails – which are near steady state – agree with this result.

Presence of the net driving force

One immediate observation is that (6.3) no longer holds if $s \neq 0$. Therefore, the usual Riemann invariants do not play a role (Le Roux, 1998). We introduce a function $\mathcal{E}$ to analyze the system for the general case:

$$\mathcal{E}'(h) = \beta - h(u')^2. \tag{6.4}$$

Below, we will show that $\mathcal{E}$ is an energy function, which is related to the total energy of the system. This is the first energy function that we consider. By combining (6.4) with (6.2) we obtain:

$$\mathcal{E}'(h)\frac{\partial h}{\partial x} = s, \qquad \frac{\partial \mathcal{E}(h)}{\partial x} = s. \tag{6.5}$$

This shows that the spatial derivative of $\mathcal{E}$ is the net acceleration of the system. Again from the mass balance in (6.2) and applying the chain-rule of differentiation, we get:

$$\frac{\partial \mathcal{E}(h)}{\partial t} = -s\frac{d}{dh}(hu). \tag{6.6}$$

The time rate of $\mathcal{E}$ is also related to the net driving acceleration, and therefore the energy function $\mathcal{E}$ is constant if the system does not accelerate. Even if the flow is stationary (which here means the flux is constant with respect to the flow depth), $\mathcal{E}$ is not constant (although the time rate of $\mathcal{E}$ vanishes) because this does not apply to the partial derivative with respect to space. Equations (6.5) and (6.6) lead to the following representation of the energy function

$$\mathcal{E}(h) = s_g\,(x - x_d) + s_f x + \lambda(t), \tag{6.7}$$

where x_d is the constant of integration, which is the distance from the point of the mass release along the channel to the point where the flow hits the horizontal reference datum. Gravitational potential energy is maximum at the position of the mass release where the frictional dissipation is minimum (or zero), and vice versa at the reference datum. This is the reason for choosing different but appropriate references for s_g and s_f, respectively, in (6.7). Since the "granular-graph" varies in space for rarefied granular flows on inclines, $\partial h/\partial x \neq 0$. With $\partial_x \partial_t \mathcal{E} = \partial_t \partial_x \mathcal{E}$, this leads to the following exact representation of the granular-flux or momentum,

$$hu = \psi h + \mu, \tag{6.8}$$

where ψ and μ are constants of integration and ψ is the flux gradient, so has a dimension of a velocity. This establishes a simple and explicit linear relationship between

the flux and the flow height.

An alternative representation of $\mathcal{E}$ is achieved by combining (6.4) with (6.8):

$$\mathcal{E}(h) = \frac{1}{2}(u - \psi)^2 + \beta h. \tag{6.9}$$

Combining the two equivalent representations in (6.7) and (6.9), we obtain

$$\mathcal{E}(h) = \frac{1}{2}(u - \psi)^2 + \beta h \equiv s_g[(x - x_d) - \psi t] + s_f[x - \psi t] + \lambda_0, \tag{6.10}$$

where λ_0 is a constant. Note that the constants ψ, μ and λ_0 are problem-specific and their values can be determined differently for different problems, e.g., dam-break flows, roll waves, splash flows, or a flow discharged from a silo (Le Roux, 1998; Pudasaini and Kröner, 2008). The right-hand side of (6.10) shows that the energy function $\mathcal{E}$ is a solitary wave, which travels with speed ψ. Here, $s = s_g + s_f$ is the amplifying factor of the wave and $\lambda_0 - s_g x_d$ is the absolute shift.

Riemann variables and rarefied flows

The model equations (6.1) constitute a system of hyperbolic partial differential equations. They can be written in the general vectorial construct of the Riemann variables $\mathbf{W} = \mathbf{W}(h, u)$ and slopes of the characteristic lines $\mathbf{R}_K = \mathbf{R}_K(h, u)$ as $\partial\mathbf{W}/\partial t + \mathbf{R}_K \cdot \partial\mathbf{W}/\partial x = \mathbf{S}$, where $\mathbf{S}$ is the source term with $\mathbf{W} = (u + 2\sqrt{\beta h}, u - 2\sqrt{\beta h})^T$, $\mathbf{R}_K = (u + \sqrt{\beta h}, u - \sqrt{\beta h})$, and $\mathbf{S} = (0, s)^T$, where T is the transpose. For rarefied waves, such as induced by dam-break and silo discharge, the method of characteristics and the Riemann variables can be used to construct exact solutions for unknown fields h and u in terms of a similarity variable $\xi = x/t$ (thus rarefaction fan). The solutions read: $(h, u)(\xi) = \left[(2\sqrt{\beta h_0} - \xi - 0.5st)^2/9\beta,\ 2(\sqrt{\beta h_0} + \xi - 2st)/3\right]$, where h_0 is the initial flow height.

6.3.2 Constant flux and the total energy

If there is a relatively large amount of granular material fed from the outlet of the silo or the source, and if the flow takes place in an inclined channel, the flow quickly shears down the channel and the stationary or steady-state condition (constant flux) may prevail for a long time throughout the channel (Pudasaini et al., 2007; Pudasaini and Kröner, 2008). A stationary flow can be characterized by setting $\psi = 0$ in (6.10). Then the energy function takes the form:

$$\mathcal{E}(h) = \frac{1}{2}u^2 + \beta h \equiv s_g\,(x - x_d) + s_f x + \lambda_0. \tag{6.11}$$

It is interesting to observe the two expressions for $\mathcal{E}$ in (6.11). The right-side of the expression explicitly contains s but the left does not, which is influenced by s intrinsically through the dynamical field quantities u and h. Although the right-hand side does not contain u and h explicitly, the effect is implicit through the travel distance x.

In the following we consider only the left side for $\mathcal{E}$ in (6.11). The first term $0.5u^2$ corresponds to the kinetic energy (E_{kin}) and the second term βh is the pressure potential energy $\left(E^p_{\text{pot}}\right)$ due to the pressure gradient. $\mathcal{E}$ is a convex function of h. The energy level goes to infinity for either $h \to \infty$ or $h \to 0$, which corresponds physically to a very large inflow height at the top of the channel (silo gate), or a very thin flowing layer at long distances in the channel, respectively. Analysis of the result is rather simple. The situation $h \to 0$ implies that, E^p_{pot} tends to zero but E_{kin} tends to infinity. In contrast, $h \to \infty$ implies that, E^p_{pot} tends to infinity but E_{kin} reduces to zero. The energy function attains its minimum $\mathcal{E}_{min} = 0.5\mu^2/h^2_{min} + \beta h_{min}$ with $h_{min} = \mu^{2/3}/\beta^{1/3}$ for which the critical velocity is $u_{min} = \sqrt{\beta h_{min}}$.

We now define the total energy function E, which represents the total energy of the system at a given position and time (this is the second energy function that we consider):

$$E(h) = \underbrace{\tfrac{1}{2}u^2}_{E_{\text{kin}}} + \underbrace{\beta h}_{E^p_{\text{pot}}} + \underbrace{s_g\,(x_d - x)}_{E^g_{\text{pot}}} - \underbrace{s_f x}_{-E_{\text{fric}}}, \tag{6.12}$$

where we identify the kinetic energy as E_{kin}, the two potential energies by E^p_{pot} and E^g_{pot} (these are caused by the free-surface gradient of the flow with respect to the inclined sliding surface and the gravity in the direction of motion, respectively) and the thermal or internal energy induced by the frictional dissipation along the bed by E_{fric}. The thermal energy is distributed among the sliding mass, the basal surface and possibly to the ambient environment that collectively define a closed system. For a stationary flow, E is equal to λ_0 and consequently a conserved quantity. If the flow is non-accelerating, i.e., the gravity is exactly balanced by the material friction, the sum of the kinetic and the potential energy due to pressure always remains constant. This is the total mechanical energy for a flow when the net driving acceleration is neglected. The third energy function is:

$$\Sigma := E_{\text{kin}} + E^p_{\text{pot}} \left(= E - E^g_{\text{pot}} - E_{\text{fric}}\right). \tag{6.13}$$

Otherwise, there is an additional contribution, $E^g_{\text{pot}} + E_{\text{fric}}$, induced by the net acceleration. This clearly demonstrates that even for a constant flux, the energy Σ is not constant. It must incorporate the enhancing or dissipative contribution due to the non-vanishing acceleration, and take into account the gravitational and frictional forces. In general E and Σ are related by $E = \Sigma + E^g_{\text{pot}} + E_{\text{fric}}$. For non-accelerating and non stationary flows E and Σ differ only by $s_g x_d$: $E = \Sigma + s_g x_d$. For accelerating but stationary flows, the energy function $\mathcal{E}$ takes a physical meaning: $\mathcal{E} = \Sigma$.

6.3.3 Extended total energy function

For a non-stationary flow the total energy (6.12) is no longer a constant. Instead the following applies:

$$E = \lambda_0 - \frac{1}{2}\psi^2 - s\psi t + u\psi, \tag{6.14}$$

as deduced from (6.10) and (6.12). The time dependence of E is a consequence of the time-dependence of the flow height, which leads to the fact that the force induced by

the free-surface gradient is not conservative. This becomes more clear when calculating dE/dt from (6.14), and using the mass and momentum conservation together with (6.8): $dE/dt = -\psi\beta\partial h/\partial x = \beta\partial h/\partial t$, where $\psi = u + hdu/dh$ is a non-trivial wave speed. In the following the physical meaning of the total energy function is explained in more detail.

To get the total energy function in proper dimensional form we multiply (6.12) by the mass $m = \rho$ (per unit volume, where ρ is the bulk density of the granular material)

$$E(h) = \underbrace{\tfrac{1}{2}mu^2}_{E_{\text{kin}}} + \underbrace{m\beta h}_{E^p_{\text{pot}}} + \underbrace{ms_g\,(x_d - x)}_{E^g_{\text{pot}}} - \underbrace{ms_f x}_{-E_{\text{fric}}}\,. \tag{6.15}$$

Note that the energies E, E_{kin}, E^p_{pot}, E^g_{pot} and E_{fric} have been redefined to include the multiplicity of m. The contribution $E^g_{\text{pot}} + E_{\text{fric}}$ is of particular importance as it is driving the entire energy dynamics. The potential energy, $E^p_{\text{pot}} + E^g_{\text{pot}}$, attains a maximum value at the point of mass release (e.g., the silo gate) and becomes a minimum (or may even reduce to zero if the flow depth is negligible) as the flow hits the reference horizontal datum. At that moment the potential energy is transferred to the kinetic energy, E_{kin}, and the friction induced internal energy, E_{fric}.

In order to obtain the energy for an isotropic frictionless ideal fluid, we set $K = 1$ and $\phi = \delta = 0$. Then, with $\beta = gK\cos\zeta$ and $s_g = g\sin\zeta$, (6.15) reduces to:

$$E(h) = \frac{1}{2}mu^2 + mg\cos\zeta\, h + mg\sin\zeta\,(x_d - x)\,. \tag{6.16}$$

For the energy of an ideal fluid in a horizontal channel ($\zeta = 0$) we obtain the often used form $E = 0.5mu^2 + mgh$. Therefore, we conclude that (6.15) is the extended form of the total energy budget associated with rapid (or creeping) granular flows down a channel.

Finally, the most simple forms of total energies for granular flows are

$$\zeta = 0^\circ \quad : \qquad E(h) = \frac{1}{2}mu^2 + mgKh + mg\tan\delta\, x, \tag{6.17}$$

$$\zeta = 90^\circ \quad : \qquad E(h) = \frac{1}{2}mu^2 + mg\,(x_d - x)\,. \tag{6.18}$$

In (6.17), the only deformation is due to the pressure potential and the internal anisotropic pressure ($K \neq 1$), and resisted by the basal friction because the material is in contact with the channel. In this case, the flow can be rapid or creeping (like viscous deformation), depending on the free-surface gradient. By contrast, in (6.18) the potential energy is due only to the vertical drop of the material position $(x_d - x)$ because there is a free-fall of the material that is not in contact with the sliding surface, and the basal and the internal frictions are ineffective. This means that the material does not deform due to the change in the internal pressure or the basal shearing. Therefore, in (6.18) the total energy takes the usual form for a rigid body moving in a gravitational field. Moreover, in practice it is desirable to consider kinetic and pressure potential energies, and gravity potential energy together with the

friction contribution. Hence, (6.15) represents a unified and complete form of the total energy.

Importance of different terms in the total energy function

It is desirable to properly understand the relative importance of different terms in the total energy function in (6.15). The term $m\beta h$ is very important and plays a dominant role when there is a large height gradient. Examples include the situation just after avalanche release and the onset of dam-break flows (both in inclined and horizontal surfaces), and the flow hitting defense structures (Pudasaini and Kröner, 2008). So, $m\beta h$ can cause a massive acceleration or deceleration in either situation. Here, the momentum transfer is mainly due to the hydraulic (pressure) gradient. To correctly model dam-break flows, one must properly take into account the fluid pressure gradient. This arises because in situations of rapidly spreading non-shallow (deep) flows, basal friction (E_{fric}) plays virtually no role and the gravity potential (E^g_{pot}) is dominated by the pressure potential (E^p_{pot}). On the other hand, for shallow flows, the pressure gradient ($m\beta h$) is negligible whereas gravity and friction forces are effective. At high elevations, gravity potential plays dominant role, while in the lower part of the channel the friction dominates the energy budget. A part of the gravitational potential energy goes to the kinetic energy (E_{kin}) while the remaining energy is lost to frictional heat, which goes to the thermal (internal) energy in the granular body, the basal surface and the surrounding. This reduces the momentum of the flow.

Extended Froude number and its significance

With the definition of the total energy in (6.15), we can now define an extended Richardson or Froude number, which accounts for the potential energies, E^g_{pot} and E^p_{pot}, associated with the accelerating granular flows down inclines and the pressure. The extended Froude number is defined as the ratio between the kinetic and the potential energy: $F_r = u/\sqrt{\beta h + s_g\,(x_d - x)}$. In the classical definition of the shallow-water or granular flow Froude number, the potential energy associated with the surface elevation, $E^g_{\text{pot}} = m s_g\,(x_d - x)$, is not considered. The extended Froude number differs substantially from the classical Froude number for higher surface elevations. The term βh emerges from the change of the geometry of the moving mass along the slope. Dimensional analysis suggests that for shallow flows βh is of order $\ll 1$, while u and $s_g(x_d - x)$ are both of order unity. If the mass is shallow with a virtually bed-parallel free-surface, then βh can be disregarded. In this situation, if the gravity potential is not taken into account, then Fr is unbounded even though the kinetic energy is bounded. So, formally considering the additional contribution due to the gravitational potential energy, the singularity in Fr is removed. This explains the significance of the new definition of the Froude number.

6.3.4 Simulation results for the total energy

In the following we consider the total energy E for a non-stationary flow as given by (6.15) and compare it with Σ, which is defined in (6.13) and given by the sum of the kinetic and the potential energy due to pressure. Therefore, Σ is the obtained energy

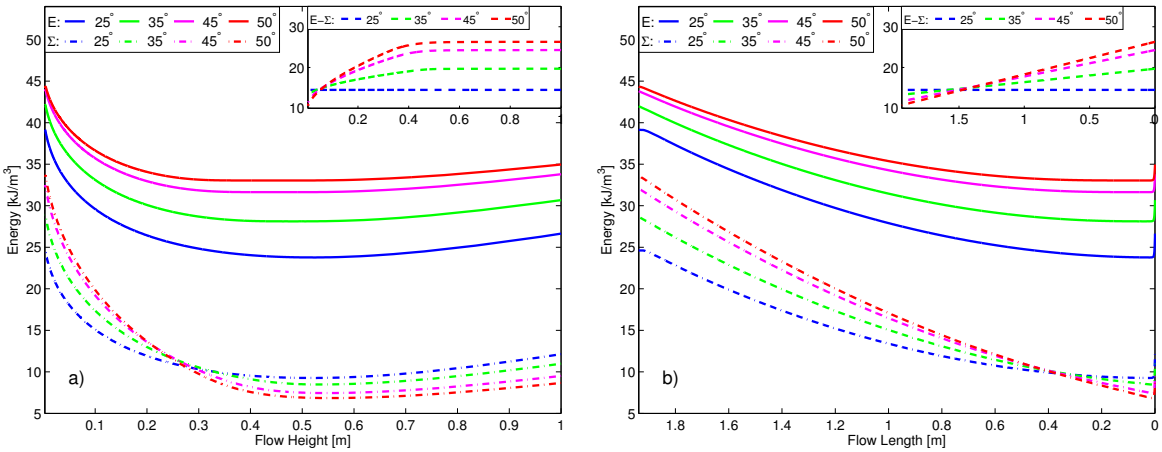

Figure 6.1: a) Energy curves E , Σ and difference $E - \Sigma$ in accelerating rapid frictional granular flows down a steep channel with respect to the flow height. b) Same as in a) but with respect to the flow length. u and h are obtained from simulation of (6.1). Flow is from right to left.

if one neglects the net driving acceleration. This comparison allows us to evaluate additional contributions to the total energy of the system due to the potential energy induced by gravity and the frictional heat internal (thermal) energy. We simulated a rapid frictional granular flow down a channel with different inclines. Our analysis is based on uniform material inflow height of 1 m at the silo gate ($x = 0$), and the outlet velocity is assumed to be 0.5 ms^{-1}. The internal and basal friction angles and the density are set to $\phi = 33°$, $\delta = 25°$, and $\rho = 1750\ \mathrm{kg\,m}^{-3}$. The flow variables u and h are obtained by numerically integrating (6.1) with TVD-NOC scheme (Pudasaini and Kröner, 2008). It is worth mentioning that the travel distance and the flow height are reciprocally related. This relation depends on many physical and geometrical parameters and flow configurations. As the travel distance increases, the flow height quickly decreases and the flow velocity increases.

In Fig. 6.1a both energies E and Σ are shown as a function of the flow height h for an accelerating flow down a channel with inclines from $\zeta = 25°$ up to 50°. At the silo gate both potential energies are maximum and the kinetic and the thermal energy are zero. As the flow hits the horizontal reference datum ($x = x_d$), the gravitational potential energy becomes zero, the pressure potential energy reaches a minimum (or is even negligible), and the kinetic energy and thermal energy attain their maxima. Hence, both E and Σ obtain maxima at $x = 0$ and $x = x_d$. Furthermore, the simulations reveal that as ζ increases, E also increases (for a given h), because of the associated higher potential energy. But for all slope angles Σ is smaller than E because it does not take into account the positive net driving acceleration. Therefore, Σ underestimates the associated energy of the flow, as anticipated. This becomes more clear with the energy difference curves, $E - \Sigma$ (in the inset). For the case $\zeta = \delta = 25°$, the difference is constant over the entire channel (blue line), but for $\zeta > \delta$, the flow is accelerating, $E - \Sigma$ is very large and strongly varies. For a large range of h, this difference is bigger

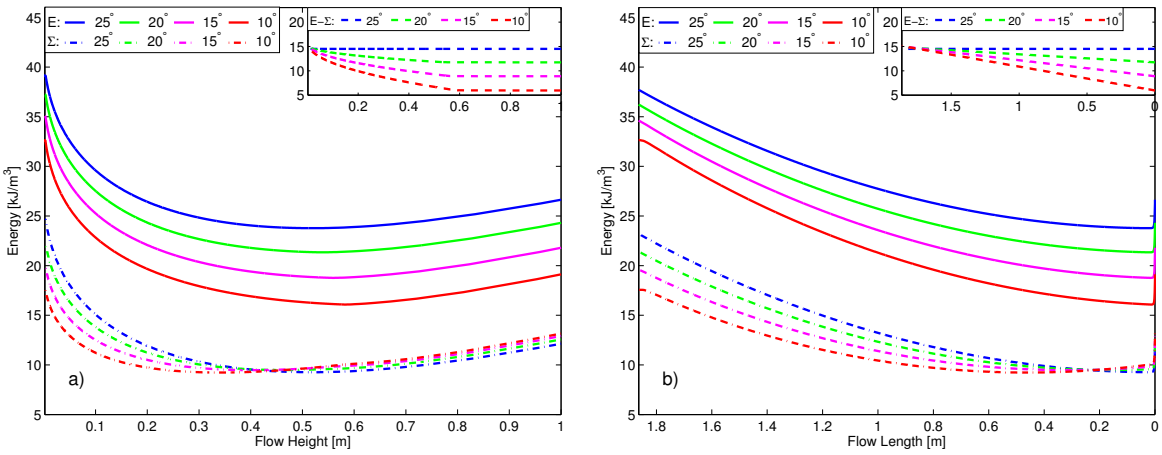

Figure 6.2: a) Energy curves E , Σ and difference $E - \Sigma$ in decelerating frictional granular flows down a steep channel with respect to the flow height. b) Same as in a) but with respect to the flow length. u and h are obtained from simulation of (6.1). Flow is from right to left.

for higher differences between slope and basal friction angles, $\zeta - \delta$. This analysis can also be complemented by plotting the energies as a function of the flow length x (Fig. 6.1b). The total energy decreases very rapidly just below the silo gate because the flow height decreases strongly, as does the pressure potential energy E^p_{pot}. This is also the reason for the constant value of the energy difference curve for big flow heights in Fig. 6.1a. The interesting point in the above analysis is that both total energy functions attain their minima, and that E is always bounded from below by Σ.

To complete the discussion, we also present the total energy curves for decelerating flows ($\delta > \zeta$) and the corresponding energy difference curves in Fig. 6.2. Here, ϕ and δ are kept fixed as before, but the channel slope angles are decreased to $\zeta = 25°, 20°, 15°$ and $10°$, respectively. Therefore, the flow is driven only by the surface gradient and resisted by the net driving deceleration (basal friction in excess to the gravity load). The results are analogous to Fig. 6.1, except that the energy difference ($E - \Sigma$, in the inset) is now increasing instead of decreasing along x due to the deceleration. Furthermore, the energy difference is bigger for higher differences $\delta - \zeta$ over a large portion of the channel. So, in general, for an accelerating or decelerating flow the magnitude of $E - \Sigma$ is related to the absolute value of $(\zeta - \delta)$. It is very important to properly include the net driving acceleration (deceleration) while calculating the total energy for flows when the friction (gravity) is dominated by gravity (friction). The net driving acceleration (or deceleration) plays an important role in determining the total energy.

Influence of the earth pressure coefficient

Recently, Pudasaini and Kröner (2008) studied the influence of the earth pressure coefficient on the dynamics of the rapid granular flows down an inclined channel. Their results, as compared with the experimental data, demonstrated that it is essential to employ the anisotropic earth pressure coefficient ($K \neq 1$) in contrast to the isotropic

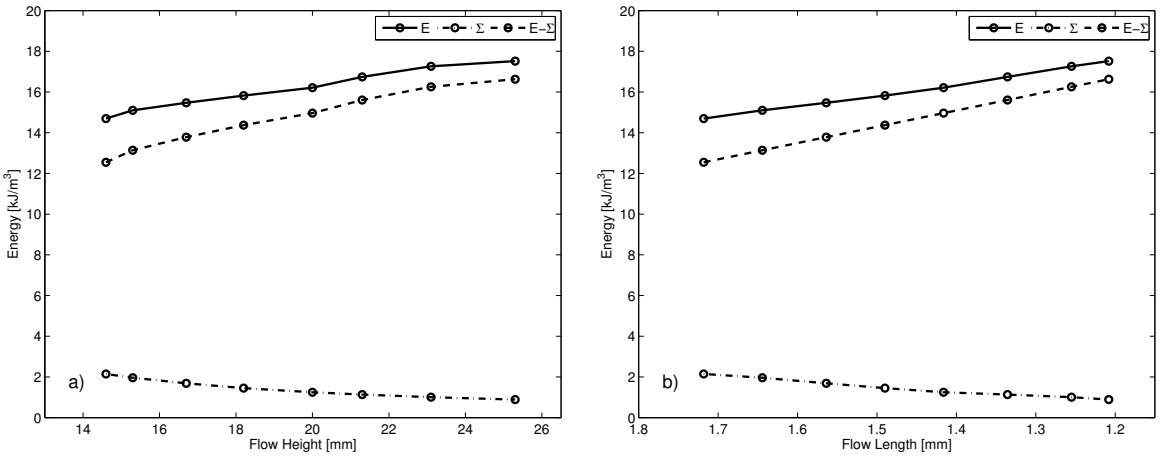

Figure 6.3: a) Energy curves E, Σ and difference $E - \Sigma$ in an accelerating rapid frictional granular flow down a steep channel with respect to the flow height. b) Same as in a) but with respect to the flow length. u and h are obtained from the experimental data (Pudasaini et al., 2007). Flow is from right to left.

pressure ($K = 1$). For extensional flow, with $\phi = 33°, \delta = 25°$, $K = 0.7656$, which is less than unity. Therefore, by using $K = 1$, the pressure potential energy would be increased non-physically by more than 23 %. This influence is substantial when the flow height and the difference in the friction angles ($\phi - \delta$) are larger, mainly in the vicinity of the silo gate. The influence of K is larger for Σ than for E.

Total energy of the experimental granular channel flow

We now consider an experiment with granular quartz particles of mean diameter 5 mm flowing down a 2 m long steep rectangular channel inclined at an angle 50°. The opening gap of the silo gate is 0.06 m and ϕ and δ are as before (Pudasaini et al., 2007). The total energy curves, both with respect to the flow height and the flow length, are shown in Fig. 6.3. The data is used to analyze the lower part of the channel. As explained before, the energy curves show large deviations of Σ from E. However, we do not have enough data to show how these energy curves would attain their minima like in Fig. 6.1. As inferred from the simulation, for Σ the energy minimum lies on the right side of the curve whilst for E on the left. Moreover, Figs. 6.1 and 6.3 represent similar qualitative behavior but for different boundary conditions.

The curves $E - \Sigma$ in Figs. 6.1-6.3 clearly demonstrate that the potential energy E^g_{pot} and the friction energy E_{fric} can not be neglected in the energy considerations for an accelerating (or decelerating) flow of frictional granular materials down sloping surfaces. Otherwise, one gets a substantial discrepancy to the actual total energy. This discrepancy can be of the order of tens of kilojoule per cubic meter of material for even one meter or a few centimeters of silo gate opening. This would be substantially higher for natural avalanches or debris flows consisting of up to 10^{12} m^3 of material (Pudasaini and Miller, 2013).

6.4 Conclusions

We considered the total energy E; carried out by the rapidly deforming and flowing frictional granular material down inclined slope; that takes into account the net driving acceleration of the system, spatio-temporal variations in flow height and the flow velocity. To derive an expression for E, we introduced an auxiliary energy function $\mathcal{E}$ which manifests itself as a solitary wave. $\mathcal{E}$ has some interesting features. It is related to the determinant of the corresponding matrix of the flow equations. The spatial derivative of $\mathcal{E}$ is the net-acceleration of the system and thus it is a constant if the system does not accelerate. For the case of an accelerating but stationary flow, this function is given by the sum of the kinetic and pressure potential energy associated with the variations in flow height and bulk deformations. Therefore, $\mathcal{E}$ supplies these two energy contributions to the total energy E, which additionally takes into account the gravitational potential and the dissipative frictional energy essential for modelling granular flows. The dissipative frictional energy is induced by the Coulomb friction force acting at the basal surface. It characterizes, together with the pressure potential energy (which takes into account the extensional or compressional nature of the flow with an anisotropic earth pressure coefficient), the whole frictional behavior of the granular flow. Since the force induced by the free-surface gradient is not conservative, the total energy E is not constant for non-stationary flows. It is a conserved quantity only for a stationary flow. If the flow is non-accelerating the total mechanical energy of the flow, as the sum of the kinetic and the potential energy due to pressure, always remains constant. When the media is an ideal fluid and the net-driving force vanishes, the total energy reduces to an often used energy form. Simulation and experimental results demonstrate that the influence of the net-driving force and the geometric deformation of the sliding mass on the total energy E is substantial. We have also defined the extended Froude number that differs substantially from the classical thin-film flow Froude number for higher surface elevations in that it takes into account the additional contribution due to gravitational potential energy not previously considered. Finally, we mention that the presented considerations enhances our understanding of mass flows and offers an explicit expression for the total energy for accelerating flows of frictional material down inclined slopes. Practitioners can find the energy functions derived here useful in dealing with the avalanche defense, hazard mapping and planning. A practical application is to help derive engineering formulas describing the dissipation of flow energy when avalanches strike retarding structures such as catching and deflecting dams, and breaking mounds.

Chapter 7

Summary and Conclusions

In this work we modelled and simulated full dimensional rapid granular free-surface flows in steep inclined channels. We addressed the problem of appropriate boundary conditions for granular flows and developed a new coupled two-dimensional pressure-dependent Coulomb-viscoplastic model with non-zero slip velocities, which provides a complete description of the flow dynamics, on the one hand, and a moderate computational effort, on the other hand. This coupled model uses a full two-dimensional model except in regions with smooth changes of flow variables, where a one-dimensional, depth-averaged model is used instead. The final coupled model is developed in several steps.

At first, we presented a full two-dimensional, Coulomb-viscoplastic sliding model, which includes some basic features and observed phenomena in dense granular flows like the exhibition of a yield strength and a non-zero slip velocity. The interaction of the flow with the solid boundary was modelled by a pressure and rate-dependent Coulomb-viscoplastic sliding law. The numerical treatment of the presented model required a set up of a novel pressure equation, which defines the pressure independent of the bottom boundary velocities. A simple viscoplastic granular flow down an inclined channel subject to slip or no-slip at the bottom boundary was studied numerically with the marker-and-cell method. The simulation results demonstrated the substantial influence of the chosen boundary condition. The Coulomb-viscoplastic sliding law revealed completely different flow dynamics and flow depth variations of the field quantities, including velocities and dynamic pressure, compared to the commonly used no-slip boundary condition. We showed that for the Coulomb-viscoplastic sliding law observable velocity shearing mainly takes place close to the sliding surface in agreement with observations. In contrast, for the no-slip boundary condition a considerable velocity shearing was observed along the entire flow depth, which contradicts with experimental observations. We showed that the hydrostatic pressure assumption, which is made by classical avalanche and granular flow models, does not hold for flow configurations considered here, as the simulated full dynamic pressure differs considerably from the hydrostatic pressure. A general Froude number, which includes both the pressure potential and gravity potential energies, was proposed. It increases with downslope positions and also while moving from the bottom to the free surface. The analysis of the Froude number showed that granular flows on inclined surfaces are

characteristically rapid supercritical flows.

An important aspect in our modelling and simulation approach is that, no assumptions are made both in the physical modelling and the numerical simulation scheme in contrast to the depth-averaged modelling and simulation, where a shallowness parameter is introduced and hydrostatic pressure, flux limiting and lateral pressure coefficients are assumed. Moreover, full dimensional modelling avoids the necessity of the inclusion of the earth pressure coefficient as we do not need to close the lateral pressure.

Subsequently, we extended our Coulomb-viscoplastic sliding model by proposing a pressure-dependent yield strength to account for the frictional nature of granular materials. In our approach, the yield strength is uniquely derived and expressed in terms of the internal friction angle of the material and plays an important role, e.g., in deposition processes. Hence, no additional calibration parameter is required as, e.g., in Bingham models, which is a big advantage. With the pressure-dependent yield strength, the material deposition at a rigid frontal wall was successfully simulated. In contrast, for a classical Bingham material law (pressure-independent yield stress) we observed almost no deposition but mostly a change of the flow direction. The proposed full two-dimensional Coulomb-viscoplastic model does not require any fit parameters, in contrast to some other models (Pouliquen, 1999; Pouliquen and Forterre, 2002; Jop et al., 2006), which is an advantage. Instead, material parameters like the internal and bed friction angle and the viscosity are used to describe the granular flow.

The presented full two-dimensional, extended Coulomb-viscoplastic sliding model belongs to the class of non depth-averaged models (N-DAM), which require high computational complexity and relatively large computing power compared to depth-averaged models (DAM). This motivated us for the development of an innovative multiscale strategy in which the full two-dimensional, non depth-averaged model was coupled with a one-dimensional, depth-averaged model. With the coupled model the computational complexity was reduced dramatically by using DAM in regions with smooth changes of flow variables. In regions where depth-averaging becomes inaccurate, like in the initiation and deposition regions and particularly, when the flow hits an obstacle or a defence structure, N-DAM must be used, because in these regions the momentum transfer must be considered in all directions. With this domain decomposition, the run-time of the simulation could be reduced from days (for N-DAM) to hours (for coupled model) for the configurations considered here. We demonstrated that the performance of the coupling is very high: The numerical results obtained by the coupled model deviate only slightly from the ones generated with the full two-dimensional model. This shows that the coupled model, which retains all the basic physics of the flow, is an attractive alternative to an expensive, full two-dimensional model. This is a substantial advantage when considering large scale geophysical mass flows in nature such as snow avalanches, rock avalanches, debris flows, and landslides.

The full two-dimensional model was used to numerically study the granular flow dynamics inside a silo and the release of the stored granular material through an opening gate. The material slips along the silo boundaries and the channel bottom according to a Coulomb friction law. We demonstrated that the proposed continuum mechanical model can successfully describe the motion of a granular material within a silo,

including solid-liquid transitions and (pressure-dependent) slip velocities at the silo boundaries. The simulation results revealed that the outflow velocity at the opening gate varies both with time and flow depth. With a set of fit parameters, the outflow velocity could be described analytically. This provides the inflow boundary condition for an inclined channel flow impinging on a rigid wall at the end of the channel that was simulated by numerically solving the coupled model. The usage of the coupled model reduced the computational complexity and time dramatically by retaining all the basic physics of the flow. We demonstrated that the simulated front position, flow velocities and deposit heights agree very well with the data obtained from laboratory experiments. This implies that the proposed full two-dimensional Coulomb-viscoplastic model with pressure-dependent yield strength, including its numerical solution and its coupling to DAM, is able to describe gravity driven rapid granular flows.

We also studied energies associated with rapid granular flows, which are useful in avalanche defence, hazard mitigation and planning. A complete expression for the total energy associated with a rapid frictional granular shear flow down an inclined surface was presented, in which gravity, friction, bulk motion, and its deformation were taken into account. We demonstrated that the total energy is conserved for stationary flow, but for non-stationary flow the non-conservative force induced by the free-surface gradient means that energy is not conserved. Numerical simulations showed that gravity acceleration and frictional resistance can be of the same order of magnitude as the sum of the kinetic and pressure energy. We also introduced an extended Froude number that takes into account the apparent potential energy induced by gravity and pressure.

By implementing a Coulomb friction law as boundary slip condition for non depth-averaged models, we have provided a possible solution to the issue already pointed out in the beginning of this thesis:

> "... when attempting a hydrodynamic approach to granular flow, we are still at a loss as to how to treat the boundaries correctly, while it is obvious that the ordinary hydrodynamic nonslip boundary assumptions are invalid" (Jaeger et al., 1996).

Furthermore, the presented multiscale strategy for coupling N-DAM with DAM provides a substantial advantage when considering large scale geophysical mass flows in nature such as snow avalanches, rock avalanches and debris flows, as this reduces the required computational power dramatically.

However, up to now there is no model, which can describe the full range of characteristics of granular flows. The friction (yield) criterion, which describes the solid-liquid transition, cannot describe the full characteristics of solid-liquid transitions in granular materials as it does not consider the history of previous deformations (Forterre and Pouliquen, 2008). For example, the initiation of the flow is sensitive to the initial preparation of the sample (Daerr and Douady, 1999). However, we showed that for rapid granular flows considered here, the proposed yield criterion describes the solid-liquid transitions of the material (both during the flow in the silo and in the deposition process) in an appropriate way such that the simulation results for the

velocities and deposit depth well reproduce experimental data. Next, hydrodynamic models are based on phenomenological approaches and a link to the microscopic properties of the grains is still in the early phase of development (Forterre and Pouliquen, 2008; Weinhart et al., 2012). Furthermore, the models presented in this work are based on the incompressibility assumption. Appropriate inclusion of density variations may be desirable, as it may be important, e.g., for flows suddenly stopped after hitting a rigid obstruction. In views of modelling geophysical mass flows, it may be necessary to advance from single phase to multiphase debris flows (Pudasaini, 2012), as granular materials under natural conditions are mainly mixtures of a loose solid phase, a liquid and/or a gas. Furthermore, natural flows take place over general topographies and may require a full three-dimensional treatment, which also includes the lateral spreading and contracting of the flow.

Appendix A

Strain Rate Dependent Coulomb Friction Law

Here, we explicitly obtain equation (3.11):

$$\left[(\mathbf{n}\cdot\nabla)\,(\mathbf{t}\cdot\mathbf{u})\right]^b - 2c^F\left[(\mathbf{t}\cdot\nabla)\,(\mathbf{t}\cdot\mathbf{u})\right]^b = \frac{c^F}{\nu^b_{\text{eff}}}p^b\,, \tag{A.1}$$

which represents a strain rate dependent Coulomb friction law on an arbitrarily orientated, flat boundary (indicated by the superscript b). We start with the computation of the strain rate vector across a surface with normal $\mathbf{n}$ and the tangent $\mathbf{t}$:

$$2\mathbf{D}\mathbf{n} = \left[(\nabla\otimes\mathbf{u}) + (\nabla\otimes\mathbf{u})^T\right]\mathbf{n},$$

where we used the definition (2.16) of the strain rate tensor $\mathbf{D}$. The del operator can be decomposed into its normal and tangential parts* (projected along $\mathbf{n}$ and $\mathbf{t}$, respectively), $\nabla = \mathbf{n}\partial_N + \mathbf{t}\partial_T$, yielding

$$\begin{aligned} 2\mathbf{D}\mathbf{n} &= \partial_N\left[(\mathbf{n}\otimes\mathbf{u}) + (\mathbf{n}\otimes\mathbf{u})^T\right]\mathbf{n} + \partial_T\left[(\mathbf{t}\otimes\mathbf{u}) + (\mathbf{t}\otimes\mathbf{u})^T\right]\mathbf{n} \\ &= \partial_N\left[(\mathbf{n}\cdot\mathbf{u})\,\mathbf{n} + \mathbf{u}\right] + \partial_T\,(\mathbf{n}\cdot\mathbf{u})\,\mathbf{t}, \end{aligned}$$

where we used the dyadic product rules

$$\begin{aligned} \left[\mathbf{v}\otimes\mathbf{w}\right]^T &= \mathbf{w}\otimes\mathbf{v}\,, \\ (\mathbf{v}\otimes\mathbf{w})\cdot\mathbf{u} &= \mathbf{v}\,(\mathbf{w}\cdot\mathbf{u})\,, \end{aligned}$$

and assumed that the orientation of the sliding surface ($\mathbf{n}$) remains unchanged along the channel. Using the decomposition $\mathbf{u} = u_n\mathbf{n} + u_t\mathbf{t}$, we obtain for the strain rate vector across a surface

$$2\mathbf{D}\mathbf{n} = 2\,(\partial_N u_n)\,\mathbf{n} + (\partial_N u_t + \partial_T u_n)\,\mathbf{t}\,. \tag{A.2}$$

*Here, we consider only two-dimensional stress states. However, the computations can easily be extended to three dimensions and the rate dependent Coulomb friction law computed here is valid both for two and three dimensions.

Recall the following expressions for the stress tensor (3.3), the shear stress and the normal pressure on a surface:

$$\begin{aligned}\boldsymbol{\sigma} &= -p\mathbb{1} + 2\nu_{\text{eff}}\mathbf{D},\\ T &= \boldsymbol{\sigma}\mathbf{n}\cdot\mathbf{t}\,,\\ N &= -\boldsymbol{\sigma}\mathbf{n}\cdot\mathbf{n}\,.\end{aligned}$$

With this, the shear stress at a rigid boundary surface, $T^b = \boldsymbol{\sigma}^b\mathbf{n}\cdot\mathbf{t}$, can be expressed as

$$T^b = 2\nu^b_{\text{eff}}\mathbf{D}^b\mathbf{n}\cdot\mathbf{t}.$$

Applying the result (A.2), we get

$$T^b = \nu^b_{\text{eff}}\left[\partial_N u_t + \partial_T u_n\right]^b.$$

With $\partial_N = (\mathbf{n}\cdot\nabla)$, $\partial_T = (\mathbf{t}\cdot\nabla)$, $u_n = (\mathbf{n}\cdot\mathbf{u})$, and $u_t = (\mathbf{t}\cdot\mathbf{u})$, this can equivalently be written as

$$T^b = \nu^b_{\text{eff}}\left[(\mathbf{n}\cdot\nabla)(\mathbf{t}\cdot\mathbf{u}) + (\mathbf{t}\cdot\nabla)(\mathbf{n}\cdot\mathbf{u})\right]^b.$$

Here, we assume that the material does not penetrate through a rigid boundary, so $\mathbf{n}\cdot\mathbf{u}^b = 0$ and also $\left[(\mathbf{t}\cdot\nabla)(\mathbf{n}\cdot\mathbf{u})\right]^b = 0$. Hence, the boundary shear stress is given by

$$T^b = \nu^b_{\text{eff}}\left[(\mathbf{n}\cdot\nabla)(\mathbf{t}\cdot\mathbf{u})\right]^b. \tag{A.3}$$

In an analogous manner, the normal pressure on a boundary surface can be expressed by:

$$\begin{aligned}N^b &= -\boldsymbol{\sigma}^b\mathbf{n}\cdot\mathbf{n}\\ &= p^b - 2\nu^b_{\text{eff}}\mathbf{D}^b\mathbf{n}\cdot\mathbf{n}\\ &= p^b - \nu^b_{\text{eff}}\left[2\partial_N u_n\mathbf{n} + (\partial_N u_t + \partial_T u_n)\,\mathbf{t}\right]^b\cdot\mathbf{n}\\ &= p^b - 2\nu^b_{\text{eff}}\left[\partial_N u_n\right]^b\\ &= p^b - 2\nu^b_{\text{eff}}\left[(\mathbf{n}\cdot\nabla)(\mathbf{n}\cdot\mathbf{u})\right]^b.\end{aligned}$$

By using the continuity equation

$$\begin{aligned}0 &= \nabla\cdot\mathbf{u}\\ &= (\mathbf{n}\partial_N + \mathbf{t}\partial_T)\cdot(u_n\mathbf{n} + u_t\mathbf{t})\\ &= \partial_N u_n + \partial_T u_t\\ &= (\mathbf{n}\cdot\nabla)(\mathbf{n}\cdot\mathbf{u}) + (\mathbf{t}\cdot\nabla)(\mathbf{t}\cdot\mathbf{u})\,,\end{aligned}$$

the normal pressure is then given by

$$N^b = p^b + 2\nu^b_{\text{eff}}\left[(\mathbf{t}\cdot\nabla)(\mathbf{t}\cdot\mathbf{u})\right]^b. \tag{A.4}$$

The Coulomb sliding law relates the shear stress to the normal pressure on the boundary

$$T^b = \frac{u^b}{|u^b|} \tan \delta N^b \,. \tag{A.5}$$

With (A.3) and (A.4), the Coulomb sliding law (A.5) can now alternatively be formulated in terms of strain rates and pressure:

$$\left[(\mathbf{n} \cdot \nabla) (\mathbf{t} \cdot \mathbf{u}) \right]^b - 2c^F \left[(\mathbf{t} \cdot \nabla) (\mathbf{t} \cdot \mathbf{u}) \right]^b = \frac{c^F}{\nu^b_{\text{eff}}} p^b \quad \text{with} \quad c^F = \frac{u^b}{|u^b|} \tan \delta \,.$$

This represents the strain rate dependent Coulomb friction law (A.1) on an arbitrarily orientated, flat boundary surface with normal $\mathbf{n}$ and tangent $\mathbf{t}$.

Appendix B

Discretisation of Momentum Balance

The momentum balance (Chapter 2) can be written as

$$\frac{d\mathbf{u}}{dt} = \nabla \cdot \boldsymbol{\sigma} + \mathbf{g}, \tag{B.1}$$

where the total derivative is given by $d\mathbf{u}/dt = \partial_t \mathbf{u} + (\mathbf{u} \cdot \nabla)\,\mathbf{u}$. The stress tensor for a viscoplastic material with a yield stress expressed as $\tau_y = \tau_c + \tau_p p$ can be decomposed into a Newtonian part* $\boldsymbol{\sigma}^N$, a Bingham part† $\boldsymbol{\sigma}^B$, which is related to τ_c, and a pressure-dependent part $\boldsymbol{\sigma}^P$, which is related to τ_p, as

$$\boldsymbol{\sigma} = \boldsymbol{\sigma}^N + \boldsymbol{\sigma}^B + \boldsymbol{\sigma}^P, \tag{B.2}$$

with

$$\boldsymbol{\sigma}^N = -p\mathbb{1} + 2\nu\mathbf{D}, \tag{B.3}$$
$$\boldsymbol{\sigma}^B = 2\nu_D \tau_c \mathbf{D}, \tag{B.4}$$
$$\boldsymbol{\sigma}^P = 2\nu_D \tau_p p \mathbf{D}, \tag{B.5}$$

where $\nu_D = (1 - \exp(-m_y\,||\mathbf{D}||))\,/\,||\mathbf{D}||$ and $\mathbf{D} = 1/2\left((\nabla\mathbf{u}) + (\nabla\mathbf{u})^T\right)$ (Section 3.2.1). By introducing the notations

$$\mathbf{F}^N = -(\mathbf{u} \cdot \nabla)\,\mathbf{u} + 2\nu\nabla \cdot \mathbf{D} + \mathbf{g}, \tag{B.6}$$
$$\mathbf{F}^B = \nabla \cdot \boldsymbol{\sigma}^B, \tag{B.7}$$
$$\mathbf{F}^P = \nabla \cdot \boldsymbol{\sigma}^P, \tag{B.8}$$

the momentum equations (B.1) can then be written in the form (4.8)

$$\partial_t \mathbf{u} = \mathbf{F} - \nabla p\,, \tag{B.9}$$

*For $\tau_c = 0$ and $\tau_p = 0$ the momentum equation describes the motion of a simple Newtonian fluid.

†This is called Bingham part as for $\tau_p = 0$ and $\tau_c \neq 0$ the momentum equations describe the motion of a Bingham fluid.

with $\mathbf{F} = \mathbf{F}^N + \mathbf{F}^B + \mathbf{F}^P$. By splitting the momentum balance (B.9) into its components (here we assume a two-dimensional flow), the equations (3.7) and (3.8) are obtained

$$\partial_t u = F - \partial_x p, \tag{B.10}$$
$$\partial_t w = G - \partial_z p, \tag{B.11}$$

where $\mathbf{F} = (F, G)^T$ and $\mathbf{u} = (u, w)^T$. The components of the two-dimensional strain rate tensor are given by

$$\mathbf{D} = \begin{pmatrix} \partial_x u & \frac{1}{2}\left(\partial_z u + \partial_x w\right) \\ \frac{1}{2}\left(\partial_z u + \partial_x w\right) & \partial_z w \end{pmatrix}. \tag{B.12}$$

In the following, first the discretisations of $\mathbf{F}^N$, $\mathbf{F}^B$, and $\mathbf{F}^P$ are presented, and finally the discretisation of the full momentum equations (B.10) and (B.11) is shown.

B.1 Newtonian parts

The Newtonian momentum term $\mathbf{F}^N$ is discretised as presented in Griebel et al. (1997). The momentum equations are written in conservative form ((3.5) and (3.6))

$$F^N = -\partial_x\left(u^2\right) - \partial_z\left(uw\right) + \nu\left(\partial_x^2 u + \partial_z^2 u\right) + g\sin(\zeta),$$
$$G^N = -\partial_z\left(w^2\right) - \partial_x\left(uw\right) + \nu\left(\partial_x^2 w + \partial_z^2 w\right) - g\cos(\zeta).$$

The convective terms are discretised by using a mixture of central differences and donor-cell discretisations (Gentry et al., 1966; Griebel et al., 1997)

$$\begin{aligned}
\left[\partial_x\left(u^2\right)\right]^u_{i,j} = \frac{1}{4dx}\big\{&(u_{i,j} + u_{i+1,j})^2 - (u_{i-1,j} + u_{i,j})^2 \\
&+\kappa\left|u_{i,j} + u_{i+1,j}\right|(u_{i,j} - u_{i+1,j}) \\
&-\kappa\left|u_{i-1,j} + u_{i,j}\right|(u_{i-1,j} - u_{i,j})\big\}, \\
\left[\partial_z\left(uw\right)\right]^u_{i,j} = \frac{1}{4dz}\big\{&(w_{i,j} + w_{i+1,j})(u_{i,j} + u_{i,j+1}) \\
&-(w_{i,j-1} + w_{i+1,j-1})(u_{i,j-1} + u_{i,j}) \\
&+\kappa\left|w_{i,j} + w_{i+1,j}\right|(u_{i,j} - u_{i,j+1}) \\
&-\kappa\left|w_{i,j-1} + w_{i+1,j-1}\right|(u_{i,j-1} - u_{i,j})\big\}, \\
\left[\partial_z\left(w^2\right)\right]^w_{i,j} = \frac{1}{4dz}\big\{&(w_{i,j} + w_{i,j+1})^2 - (w_{i,j-1} + w_{i,j})^2 \\
&+\kappa\left|w_{i,j} + w_{i,j+1}\right|(w_{i,j} - w_{i,j+1}) \\
&-\kappa\left|w_{i,j-1} + w_{i,j}\right|(w_{i,j-1} - w_{i,j})\big\}, \\
\left[\partial_x\left(uw\right)\right]^w_{i,j} = \frac{1}{4dx}\big\{&(u_{i,j} + u_{i,j+1})(w_{i,j} + w_{i+1,j}) \\
&-(u_{i-1,j} + u_{i-1,j+1})(w_{i-1,j} + w_{i,j}) \\
&+\kappa\left|u_{i,j} + u_{i,j+1}\right|(w_{i,j} - w_{i+1,j}) \\
&-\kappa\left|u_{i-1,j} + u_{i-1,j+1}\right|(w_{i-1,j} - w_{i,j})\big\},
\end{aligned}$$

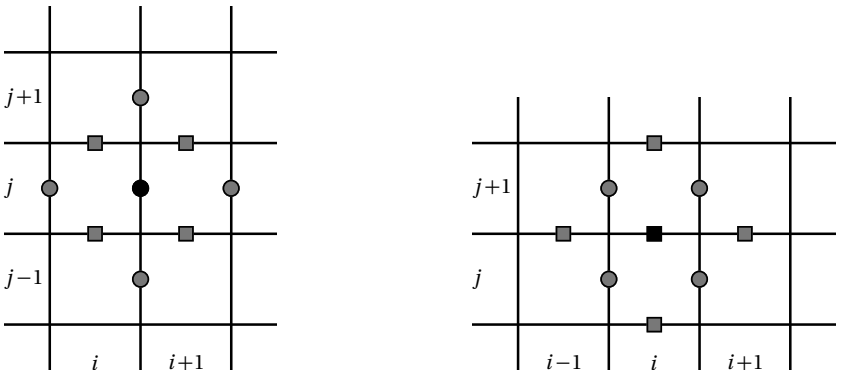

(a) $F^N_{i,j}$ (b) $G^N_{i,j}$

Figure B.1: Values required for the discretisation of $\mathbf{F}^N_{i,j}$ are shown. Filled circles represent u-velocities and filled squares represent w-velocities. The black symbols mark the discretisation points of $F^N_{i,j}$ and $G^N_{i,j}$, respectively.

where the spatial positions are specified by the subscripts i (along x) and j (along z), which denote the indices of the grid cell $C_{i,j}$. The superscripts u and w, respectively, denote the u- and the w-grid, respectively, on which the derivatives are evaluated (Fig. 3.2). On the one hand, centred differences provide a higher-order discretisation, but on the other hand, they may cause instabilities. This instability problem can be avoided by using a mixture of central differences and donor-cell discretisations through the donor-cell parameter $\kappa \in [0, 1]$, as the donor-cell scheme provides a stable discretisation of lower order. For $\kappa = 1$, a pure donor-cell discretisation is obtained, and for $\kappa = 0$, the convective derivatives are discretised by pure central differences. The value of κ should be chosen according to the dimensions of the convective terms relative to the diffusive ones, as instability problems are observed for dominating convective terms (Griebel et al., 1997). According to Hirt et al. (1975), κ should be chosen such that the condition

$$\kappa \geq \max_{i,j} \left(\left| \frac{u_{i,j} dt}{dx} \right|, \left| \frac{w_{i,j} dt}{dz} \right| \right)$$

is satisfied.

The diffusive terms are discretised by using centred differences

$$\begin{aligned}
\left[\partial_x^2 u\right]^u_{i,j} &= \frac{1}{dx^2} \left(u_{i+1,j} - 2u_{i,j} + u_{i-1,j} \right), \\
\left[\partial_z^2 u\right]^u_{i,j} &= \frac{1}{dz^2} \left(u_{i,j+1} - 2u_{i,j} + u_{i,j-1} \right), \\
\left[\partial_x^2 w\right]^w_{i,j} &= \frac{1}{dx^2} \left(w_{i+1,j} - 2w_{i,j} + w_{i-1,j} \right), \\
\left[\partial_z^2 w\right]^w_{i,j} &= \frac{1}{dz^2} \left(w_{i,j+1} - 2w_{i,j} + w_{i,j-1} \right).
\end{aligned}$$

The values required for the discretisation of $F^N_{i,j}$ and $G^N_{i,j}$ are presented in Fig. B.1.

B.2 Bingham parts

By applying the divergence on the stress tensor $\boldsymbol{\sigma}^B$ in (B.7), the discretisations of the Bingham momentum terms can be written as

$$\begin{aligned}
F_{ij}^B =& \left[\partial_x \sigma_{xx}^B\right]_{i,j}^u + \left[\partial_z \sigma_{xz}^B\right]_{i,j}^u \\
=& \frac{1}{dx}\left(\left[\sigma_{xx}^B\right]_{i+1,j}^p - \left[\sigma_{xx}^B\right]_{i,j}^p\right) + \frac{1}{dz}\left(\left[\sigma_{xz}^B\right]_{i,j}^c - \left[\sigma_{xz}^B\right]_{i,j-1}^c\right), \\
G_{ij}^B =& \left[\partial_x \sigma_{xz}^B\right]_{i,j}^w + \left[\partial_z \sigma_{zz}^B\right]_{i,j}^w \\
=& \frac{1}{dx}\left(\left[\sigma_{xz}^B\right]_{i,j}^c - \left[\sigma_{xz}^B\right]_{i-1,j}^c\right) + \frac{1}{dz}\left(\left[\sigma_{zz}^B\right]_{i,j+1}^p - \left[\sigma_{zz}^B\right]_{i,j}^p\right).
\end{aligned}$$

The discretisation of F_{ij}^B requires the discretisation of σ_{xx}^B on the p-grid and the discretisation of σ_{xz}^B on the c-grid. Here, we define the 'c-grid' by discretisation points, which are located at the upper right corner of the cells. We do not consider the discretisation of σ_{zz}^B explicitly, as $\sigma_{zz}^B = -\sigma_{xx}^B$, which follows from the continuity equation (2.5). Hence, in the following only the discretisation of F^B is considered for simplicity. With (B.4), F_{ij}^B can be expressed in terms of discretised values of $\mathbf{D}$ and ν_D:

$$\begin{aligned}
F_{ij}^B =& \frac{2\tau_c}{dx}\left(\left[\nu_D D_{xx}\right]_{i+1,j}^p - \left[\nu_D D_{xx}\right]_{i,j}^p\right) + \frac{2\tau_c}{dz}\left(\left[\nu_D D_{xz}\right]_{i,j}^c - \left[\nu_D D_{xz}\right]_{i,j-1}^c\right) \\
=& \frac{2\tau_c}{dx}\left(f_\nu(D_2^p)\left[D_{xx}\right]_{i+1,j}^p - f_\nu(D_1^p)\left[D_{xx}\right]_{i,j}^p\right) + \\
& \frac{2\tau_c}{dz}\left(f_\nu(D_2^c)\left[D_{xz}\right]_{i,j}^c - f_\nu(D_1^c)\left[D_{xz}\right]_{i,j-1}^c\right),
\end{aligned}$$

where the factor ν_D is considered as a function of the norm of the strain rate tensor $\nu_D = f_\nu(||\mathbf{D}||)$ with $f_\nu(||\mathbf{D}||) = (1 - \exp(-m_y ||\mathbf{D}||)) / ||\mathbf{D}||$ (Section 3.2.1). The norm of the strain rate tensor is given by $||\mathbf{D}|| = 2\sqrt{D_{xx}^2 + D_{xz}^2}$ (Section 2.3) and contains both normal and shear rates, whose proper discretisations are located on different grids (normal rates on p-grid, shear rates on c grid). Therefore, the approximations of $||\mathbf{D}||$, here denoted by D_k^p and D_k^c for $k \in [1, 2]$, are necessarily of lower order compared to the discretisations $[D_{xx}]_{i,j}^p$ and $[D_{xz}]_{i,j}^c$, for which central differences are applied. We propose the following discretisations

$$\begin{aligned}
\left[D_{xx}\right]_{i,j}^p &= \frac{1}{dx}\left(u_{i,j} - u_{i-1,j}\right), \\
\left[D_{xz}\right]_{i,j}^c &= \frac{1}{2dz}\left(u_{i,j+1} - u_{i,j}\right) + \frac{1}{2dx}\left(w_{i+1,j} - w_{i,j}\right), \\
D_1^p &= \sqrt{\left(2\left[D_{xx}\right]_{i,j}^p\right)^2 + \left(\left[D_{xz}\right]_{i,j}^c + \left[D_{xz}\right]_{i,j-1}^c\right)^2}, \\
D_2^p &= \sqrt{\left(2\left[D_{xx}\right]_{i+1,j}^p\right)^2 + \left(\left[D_{xz}\right]_{i,j}^c + \left[D_{xz}\right]_{i,j-1}^c\right)^2}, \\
D_1^c &= \sqrt{\left(\left[D_{xx}\right]_{i+1,j}^p + \left[D_{xx}\right]_{i,j}^p\right)^2 + \left(2\left[D_{xz}\right]_{i,j-1}^c\right)^2},
\end{aligned}$$

$$D_2^c = \sqrt{\left([D_{xx}]_{i+1,j}^p + [D_{xx}]_{i,j}^p \right)^2 + \left(2\,[D_{xz}]_{i,j}^c \right)^2}.$$

Note that there are many different possibilities to discretise the Bingham part $\mathbf{F}^B$. For example, one could explicitly compute the divergence in (B.7) by applying the partial derivatives to the stress tensor components. Then, $\mathbf{F}^B$ is explicitly formulated in terms of strain rates and its derivatives. However, our approach is based on a conservative form for $\mathbf{F}^B$ with the same numerical scheme as for a Newtonian fluid (Fig. B.1). With this approach, we observed more stable results, as no additional velocities, which are not available near free surfaces or boundaries, are required.

B.3 Pressure-dependent parts

With the use of (B.5) and (B.8) and after applying the product rule of differentiation, the following expressions are obtained for the pressure-dependent momentum terms

$$\begin{aligned} F^P &= f_0\, p + f_x\, \partial_x p + f_z\, \partial_z p, \\ G^P &= g_0\, p + g_x\, \partial_x p + g_z\, \partial_z p, \end{aligned}$$

with the abbreviations

$$\begin{aligned} f_0 &= 2\tau_p \left[\partial_x \left(\nu_D D_{xx} \right) + \partial_z \left(\nu_D D_{xz} \right) \right], \\ f_x &= 2\tau_p \nu_D D_{xx}, \\ f_z &= 2\tau_p \nu_D D_{xz}, \\ g_0 &= 2\tau_p \left[\partial_z \left(\nu_D D_{zz} \right) + \partial_x \left(\nu_D D_{xz} \right) \right], \\ g_x &= 2\tau_p \nu_D D_{xz}, \\ g_z &= 2\tau_p \nu_D D_{zz}. \end{aligned}$$

The pressure-dependent momentum terms are then discretised by

$$\begin{aligned} \left[F^P \right]_{i,j}^u &= [f_0]_{i,j}^u\, [p]_{i,j}^u + [f_x]_{i,j}^u\, [\partial_x p]_{i,j}^u + [f_z]_{i,j}^u\, [\partial_z p]_{i,j}^u, \\ \left[G^P \right]_{i,j}^w &= [g_0]_{i,j}^w\, [p]_{i,j}^w + [g_x]_{i,j}^w\, [\partial_x p]_{i,j}^w + [g_z]_{i,j}^w\, [\partial_z p]_{i,j}^w. \end{aligned}$$

For the pressure-dependent terms, we propose the discretisations

$$\begin{aligned} [p]_{i,j}^u &= \frac{1}{2} \left(p_{i+1,j} + p_{i,j} \right), \\ [\partial_x p]_{i,j}^u &= \frac{1}{dx} \left(p_{i+1,j} - p_{i,j} \right), \\ [\partial_z p]_{i,j}^u &= \frac{1}{4dz} \left(p_{i+1,j+1} + p_{i,j+1} - p_{i+1,j-1} - p_{i,j-1} \right), \\ [p]_{i,j}^w &= \frac{1}{2} \left(p_{i,j+1} + p_{i,j} \right), \\ [\partial_x p]_{i,j}^w &= \frac{1}{4dx} \left(p_{i+1,j+1} + p_{i+1,j} - p_{i-1,j+1} - p_{i-1,j} \right), \end{aligned}$$

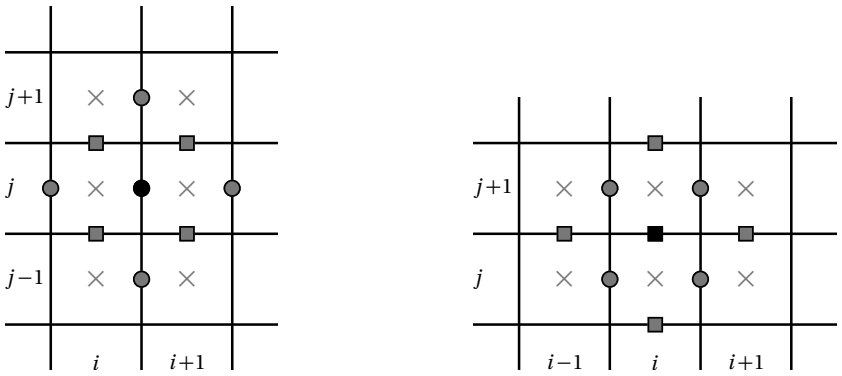

(a) $F^P_{i,j}$ (b) $G^P_{i,j}$

Figure B.2: Values required for the discretisation of $\mathbf{F}^P_{i,j}$. Filled circles represent u-velocities, filled squares represent w-velocities, and crosses represent pressures. The black symbols mark the discretisation points of $F^P_{i,j}$ respectively $G^P_{i,j}$.

$$[\partial_z p]^w_{i,j} = \frac{1}{dz}\left(p_{i,j+1} - p_{i,j}\right).$$

The discretisation of f_0 is similar to the discretisation of F^B, as formally $\tau_c f_0 = \tau_p F^B$. A corresponding relation holds for g_0. The other factors are discretised by

$$\begin{aligned}
[f_x]^u_{i,j} &= \tau_p \left([D_{xx}]^p_{i+1,j} + [D_{xx}]^p_{i,j}\right) f_\nu(D^u), \\
[f_z]^u_{i,j} &= \tau_p \left([D_{xz}]^c_{i,j} + [D_{xz}]^c_{i,j-1}\right) f_\nu(D^u), \\
[g_x]^w_{i,j} &= \tau_p \left([D_{xz}]^c_{i,j} + [D_{xz}]^c_{i-1,j}\right) f_\nu(D^w), \\
[g_z]^w_{i,j} &= \tau_p \left([D_{zz}]^p_{i,j+1} + [D_{zz}]^p_{i,j}\right) f_\nu(D^w),
\end{aligned}$$

where the norm of the strain rate tensor is approximated by

$$\begin{aligned}
D^u &= \sqrt{\left([D_{xx}]^p_{i+1,j} + [D_{xx}]^p_{i,j}\right)^2 + \left([D_{xz}]^c_{i,j} + [D_{xz}]^c_{i,j-1}\right)^2}, \\
D^w &= \sqrt{\left([D_{zz}]^p_{i,j+1} + [D_{zz}]^p_{i,j}\right)^2 + \left([D_{xz}]^c_{i,j} + [D_{xz}]^c_{i-1,j}\right)^2},
\end{aligned}$$

similar to the approximations in Appendix B.2. The values which are required for the discretisation of $F^P_{i,j}$ are shown in Fig. B.2.

Note that a discretisation of $\mathbf{F}^P$ based on conservative equations (like for $\mathbf{F}^B$) would require additional pressures, which are not available near free surfaces or boundaries. This is not the case for the discretisation scheme presented here. This is an advantage.

B.4 Full momentum equations

The momentum equations (B.10) and (B.11) are fully discretised in time and space by using an explicit Euler scheme for time discretisation, centred differences for the

discretisation of the pressure gradient, and the proposed discretisations of F and G (Appendices B.1-B.3):

$$u_{i,j}^{(n+1)} = u_{i,j}^{(n)} + dt\, F_{i,j}^{(n)} - \frac{dt}{dx}\left(p_{i+1,j}^{(n)} - p_{i,j}^{(n)}\right),$$
$$w_{i,j}^{(n+1)} = w_{i,j}^{(n)} + dt\, G_{i,j}^{(n)} - \frac{dt}{dz}\left(p_{i,j+1}^{(n)} - p_{i,j}^{(n)}\right),$$

where the superscript (n) denotes the time level.

The terms F and G may depend on the pressure, when a pressure-dependent Coulomb sliding law is used for the velocity boundary conditions, or when $\tau_p \neq 0$ (Chapter 3 and Chapter 4). If F and G are pressure-independent, a pressure Poisson equation is obtained, otherwise the pressure is computed by solving a more general pressure equation. The solution of these equations requires an explicit formulation of the dependency of F and G on the Coulomb boundary velocities like (3.25):

$$F_{i,j} = f_{i,j}^{(1)} u_{i,j-1}^{b} + f_{i,j}^{(2)},$$

This relation holds for a Coulomb friction law applied on the bottom surface, whereas $f_{i,j}^{(1)}$ and $f_{i,j}^{(2)}$ depend on the discretisation and can be calculated without the knowledge of the bottom boundary velocity:

$$f_{i,j}^{(1)} = \frac{\nu}{dz^2}, \tag{B.13}$$
$$f_{i,j}^{(2)} = F_{i,j} - f_{i,j}^{(1)} u_{i,j-1}^{b}. \tag{B.14}$$

Here, we take into account the dependency of the diffusive term $\nu\left[\partial_z^2 u\right]_{i,j}$, contained in $F_{i,j}^{N}$, on the bottom boundary velocity $u_{i,j-1}^{b}$. Note that the convective terms in $\mathbf{F}^N$ do not require any knowledge of the tangential boundary velocities. On the contrary, the Bingham and pressure-dependent parts of the momentum equation, $\mathbf{F}^B$ and $\mathbf{F}^P$, in general, depend on the tangential boundary velocities in a nonlinear manner. However, we approximate these terms near the rigid boundary such that $\mathbf{F}^B$ and $\mathbf{F}^P$ can be computed without the knowledge of the Coulomb boundary velocities[‡]. This simplifies the computations and avoids the solution of highly nonlinear equations.

[‡]The terms can be either spatially or temporally approximated. We observed that for an undisturbed flow, both approximations lead to consistent and meaningful results. However, for a flow against a rigid obstruction, strong deformations may occur, which may cause large errors when spatial approximations are used. Therefore, we propose temporal approximations by applying the results from the previous time step.

Appendix C

Multiscale Coupling Strategy

The multiscale strategy presented in Chapter 4 couples the full two-dimensional, non depth-averaged model (N-DAM) with a one-dimensional, depth-averaged model (DAM). The depth-averaged model is numerically solved by a higher-order NOC-TVD differencing scheme (Pudasaini and Hutter, 2007). A finite differencing scheme, based on the MAC-method, is used for the numerical solution of the non depth-averaged model (Section 3.3.1 and Appendix B). The corresponding numerical methods for DAM and N-DAM possesses different characteristics, which have to be taken into account in a coupling strategy.

We observe that the numerical solution of DAM may become instable for very small time steps, whereas the numerical solution of N-DAM often requires very small time steps to guarantee stability. For example, in N-DAM small time steps are required in modelling flows impinging on rigid walls or the initiation process of the flow (e.g., silo outflow), where high effective viscosities and hence large diffusion terms are observed in both situations. These situations are characterised by full two-dimensional flow characteristics and are exclusively modelled by N-DAM in the coupled model. Therefore, we introduce an internal time loop in N-DAM, which allows each numerical method (N-DAM and DAM) to have its own and automatic time stepping. The control flow of the multiscale coupling strategy is sketched in Fig. C.1. At the beginning, the inner velocities and flow depths at an initial time $t^{(n)}$ must be provided, where the term 'inner' refers to values within the flow without any boundary values. In the initialisation step of the computational program, this initial velocity field is complemented by pressure-independent boundary values. Pressure-dependent boundary values, which occur in N-DAM like Coulomb boundary velocities or pressure boundary conditions, cannot yet be applied, as the pressure is not yet known. After the initialisation of the program, a time stepping is performed, in which the velocities and flow depths at the next time step $t^{(n+1)} = t^{(n)} + dt$ are computed. According to the preceding considerations, the time step size dt is defined by DAM, $dt = dt^{\text{DAM}}$. At first, the depth-averaged velocity and the flow depth at $t^{(n+1)}$ are computed for DAM subdomains, as they may serve as boundary conditions for N-DAM subdomains (when an internal time loop is used). Subsequently, the time step size in N-DAM, $dt^{\text{N-DAM}}$, is computed according to appropriate stability criteria. For $dt^{\text{N-DAM}} < dt$, an internal time loop is performed with N_{it} iterations and the constraint $t^{(m=N_{it})} = dt$, where m

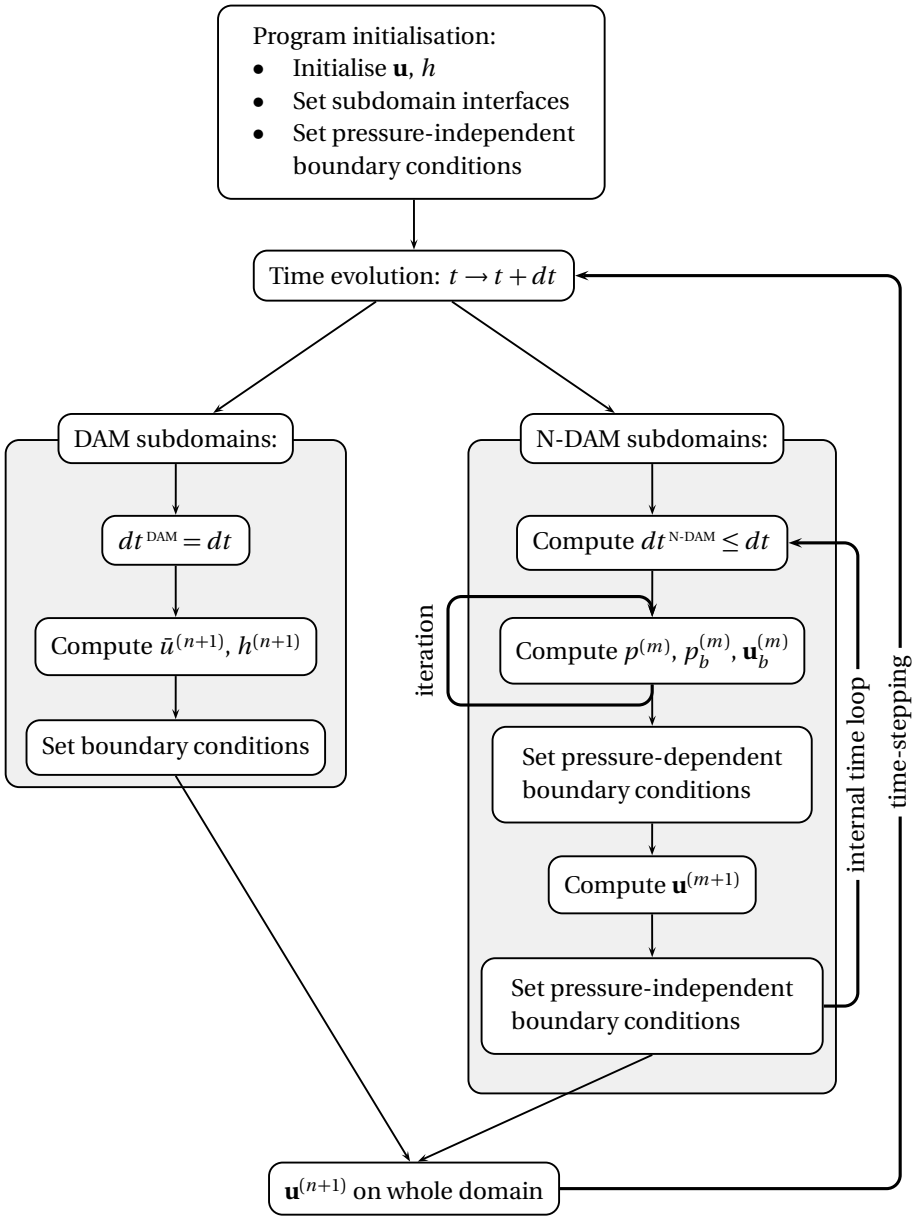

Figure C.1: A multiscale coupling strategy.

denotes the time level within the internal time loop. Thus, at the end of the internal time loop, the velocity fields at $t^{(n+1)}$ are obtained in N-DAM. In the internal time loop, all pressure-dependent quantities like the pressure itself, its boundary conditions, and the Coulomb boundary velocities, are computed at first. This is done by an iterative method depending on the underlying physical model*. The iteration stops, when the continuity equation, the pressure boundary conditions, and the Coulomb friction

*For $\tau_p \neq 0$, a modified version of the Powell's Hybrid method is used to solve the non-linear system of equations (Chapter 4). For $\tau_p = 0$, the successive overrelaxation (SOR) or conjugate gradient (CG) method can alternatively be applied (Chapter 3).

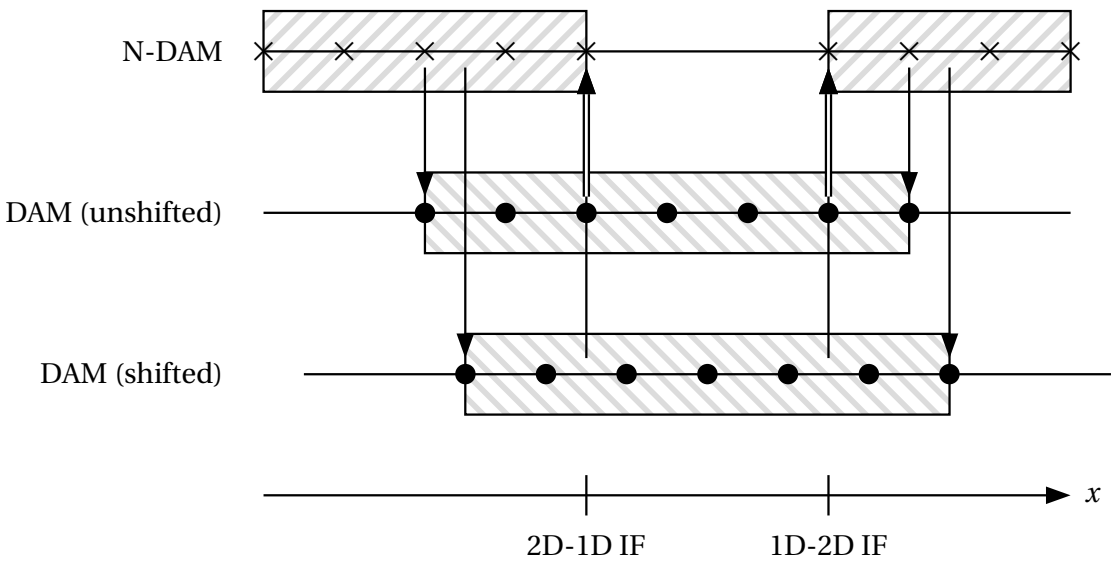

Figure C.2: Spatial arrangement of N-DAM and DAM grids along the x-direction (flow direction) in the coupled model. N-DAM grid points are marked by crosses and DAM grid points are marked by bullets.

law (velocity boundary conditions) are solved with a prescribed accuracy[†]. Afterwards, the complete velocity and pressure fields at time $t^{(m)}$ are available (including pressure-dependent boundary conditions). This allows for the computation of the inner velocities at time $t^{(m+1)} = t^{(m)} + dt^{\text{N-DAM}}$. Note that the boundary conditions at the interfaces belong to the pressure-independent boundary conditions and are applied after advancing the velocity field.

Furthermore, the numerical methods used in DAM and N-DAM define the flow variables on different grid types. This has to be taken into account properly, when arranging the N-DAM and DAM grids at the interfaces. In N-DAM a space-staggered grid is considered, in which the velocities and the pressure are not located at the same grid points (Fig. 3.2). However, the velocity along the flow depth direction and the pressure play no role in setting the in- and outflow boundary conditions for DAM (Section 4.4.2). Hence, only the u-grid in N-DAM has to be considered here. In DAM a time-staggered grid is used, where the boundaries of the cells at the new time level are the centres of the cells at the old time level. This means that the grid moves with time back and forth by a half grid width. Figure C.2 presents the spatial arrangement of N-DAM and DAM grids at the interfaces (IF). We define the interface position as the position of the outflow (2D-1D interface) or inflow (1D-2D interface) conditions of N-DAM. If the DAM grid includes grid points located exactly on the N-DAM grid, we call the DAM grid unshifted. When the DAM grid moves by a half grid width to the right in the next time step, it is called a shifted grid. The in- and outflow boundary conditions for N-DAM are obtained from DAM values and vice versa, which

[†]In this work, typically an accuracy of 10^{-5}-10^{-7} is prescribed in the solution of the system of equations.

is indicated by the vertical arrows in Fig. C.2. Two important observations can be deduced from Fig. C.2: (i) For the shifted DAM grid, a spatial interpolation is required to obtain the in- and outflow boundary conditions, as the DAM grid points are shifted with respect to the N-DAM grid points, and (ii) the N-DAM and DAM subdomains share an overlap region at the interfaces, in which both models have grid points. With the latter, the boundary conditions at the interface of one model do not directly depend on the boundary conditions at the interface of the other model. For example, the N-DAM outflow conditions are only obtained from inner DAM values, as the DAM inflow boundary values may depend on N-DAM outflow conditions. This procedure allows us to define appropriate in- and outflow boundary conditions for both models. Moreover, with this strategy different mesh sizes in x- and z-direction can be used in the subdomains, which is an advantage as the flow characteristics may be substantially to fundamentally different in individual subdomains.

Bibliography

Akivis, M.A. and Goldberg, V.V., 1972. An introduction to linear algebra and tensors. Courier Dover Publications. ISBN 9780486635453.

Ancey, C., 2007. Plasticity and geophysical flows: A review. Journal of Non-Newtonian Fluid Mechanics, 142(1-3):4–35.

Aranson, I.S. and Tsimring, L.S., 2006. Patterns and collective behavior in granular media: Theoretical concepts. Reviews of Modern Physics, 78(2):641–692.

Balmforth, N. and Frigaard, I., 2007. Viscoplastic fluids: From theory to application. Journal of Non-Newtonian Fluid Mechanics, 142(1-3):1–3.

Barbolini, M., Gruber, U., Keylock, C., Naaim, M., and Savi, F., 2000. Application of statistical and hydraulic-continuum dense-snow avalanche models to five real european sites. Cold Regions Science and Technology, 31(2):133–149.

Bartelt, P., Buser, O., and Kern, M., 2005. Dissipated work, stability and the internal flow structure of granular snow avalanches. Journal of Glaciology, 51(172):125–138.

Bartelt, P., Buser, O., and Platzer, K., 2007. Starving avalanches: Frictional mechanisms at the tails of finite-sized mass movements. Geophysical Research Letters, 34(20).

Bartelt, P., Buser, O., and Platzer, K., 2006. Fluctuationdissipation relations for granular snow avalanches. Journal of Geology, 52(179):631–643.

Beam, R. and Warming, R., 1976. An implicit finite-difference algorithm for hyperbolic systems in conservation-law form. Journal of Computational Physics, 22(1):87–110.

Bingham, E.C., 1922. Fluidity and plasticity. McGraw-Hill New York.

Bouchut, F., Mangeney-Castelnau, A., Perthame, B., and Vilotte, J.P., 2003. A new model of saint venant and savage–hutter type for gravity driven shallow water flows. Comptes Rendus Mathematique, 336(6):531–536.

Buser, O. and Bartelt, P., 2009. Production and decay of random kinetic energy in granular snow avalanches. 55(189):3–12.

Castro, M., Gallardo, J., and Parés, C., 2006. High order finite volume schemes based on reconstruction of states for solving hyperbolic systems with nonconservative products. applications to shallow-water systems. Mathematics of Computation, 75(255):1103–1134.

Christen, M., Kowalski, J., and Bartelt, P., 2010. Ramms: Numerical simulation of dense snow avalanches in three-dimensional terrain. Cold Regions Science and Technology, 63(1):1–14.

Coulomb, C., 1776. Essai sur une application des regles de maximis et minimis a quelques problemes de statique relatifs a l'architecture. Memoires de l'Academie Royale pres Divers Savants, 7.

Cui, X. and Gray, J., 2013. Gravity-driven granular free-surface flow around a circular cylinder. Journal of Fluid Mechanics, 720:314–337.

da Cruz, F., Emam, S., Prochnow, M., Roux, J.N., and Chevoir, F., 2005. Rheophysics of dense granular materials: Discrete simulation of plane shear flows. Physical Review E, 72(2):021309.

Dade, W. and Huppert, H., 1998. Long-runout rockfalls. Geology, 26(9):803–806.

Daerr, A. and Douady, S., 1999. Sensitivity of granular surface flows to preparation. Europhysics Letters, 47(3):324–330.

Davies, T., McSaveney, M., and Kelfoun, K., 2010. Runout of the socompa volcanic debris avalanche, chile: a mechanical explanation for low basal shear resistance. Bulletin of Volcanology, 72(8):933–944.

Dent, J. and Lang, T., 1982. Experiments on mechanics of flowing snow. Cold Regions Science and Technology, 5(3):253 – 258.

Domnik, B. and Pudasaini, S.P., 2012. Full two-dimensional rapid chute flows of simple viscoplastic granular materials with a pressure-dependent dynamic slip-velocity and their numerical simulations. Journal of Non-Newtonian Fluid Mechanics, 173:72–86.

Domnik, B., Pudasaini, S.P., Katzenbach, R., and Miller, S.A., 2013a. Coupling of full two-dimensional and depth-averaged models for granular flows. Journal of Non-Newtonian Fluid Mechanics, 201:56–68.

Domnik, B., Pudasaini, S.P., and Miller, S.A., 2013b. Multiscale coupling of granular flows and comparison with experimental results.

Dutykh, D. and Dias, F., 2009. Energy of tsunami waves generated by bottom motion. Proceedings of the Royal Society of London. Series A: Mathematical, Physical and Engineering Sciences, 465(2103):725–744.

Erismann, T.H. and Abele, G., 2001. Dynamics of rockslides and rockfalls. Springer Verlag.

Fang, C., Wang, Y., and Hutter, K., 2008. A unified evolution equation for the cauchy stress tensor of an isotropic elasto-visco-plastic material. Continuum Mechanics and Thermodynamics, 19:423–440.

Fine, I.V., Rabinovich, A.B., Thomson, R.E., and Kulikov, E.A., 2003. Numerical modeling of tsunami generation by submarine and subaerial landslides. In A. Yalçiner, E. Pelinovsky, E. Okal, and C. Synolakis, editors, Submarine landslides and tsunamis, volume 21, pages 69–88. Springer Netherlands.

Fischer, G., 2008. Lineare Algebra: eine Einführung für Studienanfänger. Vieweg Studium: Grundkurs Mathematik. Vieweg + Teubner. ISBN 9783834895745.

Fischer, J.T., Kowalski, J., and Pudasaini, S.P., 2012. Topographic curvature effects in applied avalanche modeling. Cold Regions Science and Technology, 74–75(0):21 – 30.

Formaggia, L., Gerbeau, J., Nobile, F., and Quarteroni, A., 2001. On the coupling of 3d and 1d navier–stokes equations for flow problems in compliant vessels. Computer Methods in Applied Mechanics and Engineering, 191(6):561–582.

Forterre, Y. and Pouliquen, O., 2008. Flows of Dense Granular Media. Annual Review of Fluid Mechanics, 40:1–24.

Galassi et al, M., 2009. GNU Scientific Library: Reference Manual. Network Theory. ISBN 0954612078.

Gauer, P., Elverhoi, A., Issler, D., and De Blasio, F., 2006. On numerical simulations of subaqueous slides: Back-calculations of laboratory experiments of clay-rich slides. Norwegian Journal of Geology, 86(3):295.

Gentry, R.A., Martin, R.E., and Daly, B.J., 1966. An eulerian differencing method for unsteady compressible flow problems. Journal of Computational Physics, 1(1):87–118.

Goldstein, S., 1938. Modern developments in fluid dynamics. Clarendon Press, Oxford.

González-Montellano, C., Ramirez, A., Gallego, E., and Ayuga, F., 2011. Validation and experimental calibration of 3d discrete element models for the simulation of the discharge flow in silos. Chemical Engineering Science, 66(21):5116–5126.

Granick, S., Zhu, Y., and Lee, H., 2003. Slippery questions about complex fluids flowing past solids. Nature Materials, 2(4):221–227.

Gray, J., Tai, Y.C., and Noelle, S., 2003. Shock waves, dead zones and particle-free regions in rapid granular free-surface flows. Journal of Fluid Mechanics, 491:161–181.

Gray, J., Wieland, M., and Hutter, K., 1999. Gravity-driven free surface flow of granular avalanches over complex basal topography. Proceedings of the Royal Society of London. Series A: Mathematical, Physical and Engineering Sciences, 455(1985):1841.

Gresho, P. and Sani, R., 1987. On pressure boundary conditions for the incompressible navier-stokes equations. International Journal for Numerical Methods in Fluids, 7(10):1111–1145.

Griebel, M., Dornseifer, T., and Neunhoeffer, T., 1997. Numerical simulation in fluid dynamics: a practical introduction. Society for Industrial and Applied Mathematics, Philadelphia.

Gruber, U. and Bartelt, P., 2007. Snow avalanche hazard modelling of large areas using shallow water numerical methods and gis. Environmental Modelling and Software, 22(10):1472 – 1481.

Gwiazda, P., 2005. On measure-valued solutions to a two-dimensional gravity-driven avalanche flow model. Mathematical methods in the applied sciences, 28(18):2201–2223.

Hákonardóttir, K. and Hogg, A., 2005. Oblique shocks in rapid granular flows. Physics of Fluids, 17:077101.

Harlow, F. and Welch, J., 1965. Numerical calculation of time-dependent viscous incompressible flow of fluid with free surface. Physics of Fluids, 8(12):2182–2189.

Hartel, C., Meiburg, E., and Necker, F., 2000. Analysis and direct numerical simulation of the flow at a gravity-current head. part 1. flow topology and front speed for slip and no-slip boundaries. Journal of Fluid Mechanics, 418:189–212.

Heim, A., 1932. Bergsturz und Menschenleben. Fretz & Wasmuth, Zürich.

Hill, R., 1998. The Mathematical Theory of Plasticity. Oxford Classic Texts in the Physical Sciences Series. Oxford University Press, Incorporated. ISBN 9780198503675.

Hirt, C., Nichols, B., and Romero, N., 1975. Sola: A numerical solution algorithm for transient fluid flows. Technical Report LA-5852, Los Alamos, NM: Los Alamos National Lab.

Hirt, C.W. and Nichols, B.D., 1981. Volume of fluid (vof) method for the dynamics of free boundaries. Journal of Computational Physics, 39(1):201–225.

Hsu, K., 1975. On sturzstroms—catastrophic debris streams generated by rockfalls. Geological Society of America Bulletin, 86:129–140.

Hutter, K. and Jöhnk, K., 2004. Continuum methods of physical modeling: continuum mechanics, dimensional analysis, turbulence. Springer Verlag.

Hwang, H. and Hutter, K., 1995. A new kinetic model for rapid granular flow. Continuum Mechanics and Thermodynamics, 7(3):357–384.

Iordanoff, I. and Khonsari, M., 2004. Granular lubrication: toward an understanding of the transition between kinetic and quasi-fluid regime. Journal of Tribology, 126(1):137–145.

Iverson, R., 1997. The physics of debris flows. Reviews of Geophysics, 35:245–296.

Jaeger, H., Nagel, S., and Behringer, R., 1996. Granular solids, liquids, and gases. Reviews of Modern Physics, 68(4):1259–1273.

Jenkins, J. and Savage, S., 1983. A theory for the rapid flow of identical, smooth, nearly elastic, spherical particles. Journal of Fluid Mechanics, 130(1):187–202.

Jin, S. and Wen, X., 2004. An efficient method for computing hyperbolic systems with geometrical source terms having concentrations. Journal of Computational Mathematics, 22(2):230–249.

Jop, P., Forterre, Y., and Pouliquen, O., 2006. A constitutive law for dense granular flows. Nature, 441(7094):727–730.

Kern, M., Tiefenbacher, F., and McElwaine, J., 2004. The rheology of snow in large chute flows. Cold Regions Science and Technology, 39(2-3):181–192.

Kerswell, R., 2005. Dam break with coulomb friction: A model for granular slumping? Physics of Fluids, 17:057101.

Khan, A.S. and Huang, S., 1995. Continuum Theory of Plasticity. John Wiley and Sons.

Kröner, C., 2013. On granular flow. PhD Thesis, Department of Geodynamics and Geophysics, University of Bonn (in preparation).

Landau, L. and Lifshitz, E., 1987. Fluid mechanics, volume 6. ISBN 0080339336.

Le Roux, A., 1998. Riemann solvers for some hyperbolic problems with a source term. In ESAIM: Proceedings, volume 6, pages 75–90.

Leger, L., Hervet, H., Massey, G., and Durliat, E., 1997. Wall slip in polymer melts. Journal of Physics: Condensed Matter, 9:7719–7740.

Liu, Y., Liu, X., and Wu, E., 2004. Real-time 3d fluid simulation on gpu with complex obstacles. In 12th Pacific Conference on Computer Graphics and Applications, 6—8 October 2004, pages 247–256. Seoul, South Korea.

Lun, C.K.K., Savage, S.B., Jeffrey, D.J., and Chepurniy, N., 1984. Kinetic theories for granular flow: inelastic particles in couette flow and slightly inelastic particles in a general flowfield. Journal of Fluid Mechanics, 140:223–256.

Mangeney, A., Heinrich, P., and Roche, R., 2000. Analytical solution for testing debris avalanche numerical models. Pure and Applied Geophysics, 157(6-8):1081–1096.

Massoudi, M. and Phuoc, T., 2000. The effect of slip boundary condition on the flow of granular materials: a continuum approach. International Journal of Non-Linear Mechanics, 35(4):745–761.

Mergili, M., Schratz, K., Ostermann, A., and Fellin, W., 2012. Physically-based modelling of granular flows with open source gis. Natural Hazards and Earth System Science, 12(1):187–200.

MiDi, G., 2004. On dense granular flows. Eur. Phys. J. E, 14:341–365.

Miglio, E., Perotto, S., and Saleri, F., 2004. A multiphysics strategy for free surface flows. In R. Kornhuber, R. Hoppe, J. Periaux, O. Pironneau, O. Widlund, and J. Xu, editors, Domain Decomposition Methods in Science and Engineering, pages 395–402. Springer.

Moriguchi, S., Borja, R., Yashima, A., and Sawada, K., 2009. Estimating the impact force generated by granular flow on a rigid obstruction. Acta Geotechnica, 4(1):57–71.

Moriguchi, S., Yashima, A., Sawada, K., Uzuoka, R., and Ito, M., 2005. Numerical simulation of flow failure of geomaterials based on fluid dynamics. Soils and Foundations, 45(2):155–165.

Muravleva, E., 2009. Finite-difference schemes for the computation of viscoplastic medium flows in a channel. Mathematical Models and Computer Simulations, 1:768–779. 10.1134/S2070048209060118.

Naaim, M., Vial, S., and Couture, R., 1997. Saint-venant approach for rock avalanches modelling. In Saint Venant Symposium, Paris, pages 28–29.

Noelle, S., Pankratz, N., Puppo, G., and Natvig, J., 2006. Well-balanced finite volume schemes of arbitrary order of accuracy for shallow water flows. Journal of Computational Physics, 213(2):474–499.

Noelle, S., Xing, Y., and Shu, C.W., 2007. High-order well-balanced finite volume weno schemes for shallow water equation with moving water. Journal of Computational Physics, 226(1):29–58.

Oda, K., Moriguchi, S., Kamiishi, I., Yashima, A., Sawada, K., and Sato, A., 2011. Simulation of a snow avalanche model test using computational fluid dynamics. Annals of Glaciology, 52(58):57.

Papanastasiou, T., 1987. Flows of materials with yield. Journal of Rheology, 31:385.

Platzer, K., Bartelt, P., and Jaedicke, C., 2007a. Basal shear and normal stresses of dry and wet snow avalanches after a slope deviation. Cold Regions Science and Technology, 49(1):11–25.

Platzer, K., Bartelt, P., and Kern, M., 2007b. Measurements of dense snow avalanche basal shear to normal stress ratios (s/n). Geophysical Research Letters, 34(7):L07501.

Pouliquen, O., 1999. Scaling laws in granular flows down rough inclined planes. Physics of Fluids, 11:542.

Pouliquen, O. and Forterre, Y., 2002. Friction law for dense granular flows: application to the motion of a mass down a rough inclined plane. Journal of Fluid Mechanics, 453:133–151.

Powell, M., 1970. A hybrid method for nonlinear equations. Numerical methods for nonlinear algebraic equations, 6:87–114.

Prager, W. and Drucker, D., 1952. Soil mechanics and plastic analysis or limit design. Quarterly of Applied Mathematics, 10(2):157–165.

Pudasaini, S.P. and Domnik, B., 2009. Energy considerations in accelerating rapid shear granular flows. Nonlinear Processes in Geophysics, 16(3):399–407.

Pudasaini, S., 2011. Some exact solutions for debris and avalanche flows. Physics of Fluids, 23:043301.

Pudasaini, S., 2012. A general two-phase debris flow model. Journal of Geophysical Research, 117:F03010.

Pudasaini, S. and Hutter, K., 2003. Rapid shear flows of dry granular masses down curved and twisted channels. Journal of Fluid Mechanics, 495:193–208.

Pudasaini, S. and Hutter, K., 2007. Avalanche dynamics: Dynamics of rapid flows of dense granular avalanches. Springer, Berlin, New York.

Pudasaini, S., Hutter, K., Hsiau, S., Tai, S., Wang, Y., and Katzenbach, R., 2007. Rapid flow of dry granular materials down inclined chutes impinging on rigid walls. Physics of Fluids, 19:053302.

Pudasaini, S. and Kröner, C., 2008. Shock waves in rapid flows of dense granular materials: Theoretical predictions and experimental results. Physical Review E, 78(4):041308.

Pudasaini, S. and Miller, S., 2013. The hypermobility of huge landslides and avalanches. Engineering Geology, 157:124–132.

Pudasaini, S., Wang, Y., and Hutter, K., 2005a. Modelling debris flows down general channels. Natural Hazards and Earth System Science, 5(6):799–819.

Pudasaini, S., Wang, Y., and Hutter, K., 2005b. Rapid motions of free-surface avalanches down curved and twisted channels and their numerical simulation. Philosophical Transactions of the Royal Society A: Mathematical, Physical and Engineering Sciences, 363(1832):1551.

Pudasaini, S., Wang, Y., and Hutter, K., 2005c. Velocity measurements in dry granular avalanches using particle image velocimetry technique and comparison with theoretical predictions. Physics of Fluids, 17:093301.

Pudasaini, S., Wang, Y., Sheng, L., Hutter, K., and Katzenbach, R., 2008. Avalanching granular flows down curved and twisted channels: Theoretical and experimental results. Physics of Fluids, 20:073302.

Rao, N., 1985. Avalanche protection and control in the himalayas. Defence Science Journal, 35(2):255–266.

Reynolds, O., 1885. On the dilatancy of media composed of rigid particles in contact, with experimental illustrations. Philosophical Magazine, 20:469–481.

Rognon, P., Chevoir, F., Bellot, H., Ousset, F., Naaïm, M., and Coussot, P., 2008. Rheology of dense snow flows: Inferences from steady state chute-flow experiments. Journal of Rheology, 52:729.

Rudenko, O., Sobisevich, A., and Sobisevich, L., 2007. Nonlinear dynamics of slope flows: Simple models and exact solutions. 416(1):1109–1113.

Sani, R., Shen, J., Pironneau, O., and Gresho, P., 2006. Pressure boundary condition for the time-dependent incompressible navier–stokes equations. International Journal for Numerical Methods in Fluids, 50(6):673–682.

Savage, S. and Hutter, K., 1989. The motion of a finite mass of granular material down a rough incline. Journal of Fluid Mechanics, 199:177–215.

Schowalter, W., 1988. The behavior of complex fluids at solid boundaries. Journal of Non-Newtonian Fluid Mechanics, 29:25–36.

Sykut, J., Molenda, M., and Horabik, J., 2008. Dem simulation of the packing structure and wall load in a 2-dimensional silo. Granular Matter, 10(4):273–278.

Tai, Y. and Gray, J., 1998. Limiting stress states in granular avalanches. Annals of Glaciology, 26:272–276.

Tai, Y., Noelle, S., Gray, J., and Hutter, K., 2002. Shock-capturing and front-tracking methods for granular avalanches. Journal of Computational Physics, 175(1):269–301.

Takahashi, T., 1991. Debris flow. IAHR-AIRH Monograph Series A, Balkema.

Takahashi, T., 2007. Debris flow: mechanics, prediction and countermeasures. Taylor and Francis, Leiden.

Tomé, M., Doricio, J., Castelo, A., Cuminato, J., and McKee, S., 2007. Solving viscoelastic free surface flows of a second-order fluid using a marker-and-cell approach. International Journal for Numerical Methods in Fluids, 53(4):599–627.

Uhland, E., 1976. Modell zur beschreibung des fließens wandgleitender substanzen durch düsen. Rheologica Acta, 15(1):30–39.

Ui, T., 1983. Volcanic dry avalanche deposits-identification and comparison with non-volcanic debris stream deposits. Journal of Volcanology and Geothermal Research, 18(1):135–150.

Upadhyay, A., Kumar, A., and Chaudhary, A., 2010. Velocity measurements of wet snow avalanche on the dhundi snow chute. Annals of Glaciology, 51(54):139–145.

Voight, B. and Sousa, J., 1994. Lessons from ontake-san: A comparative analysis of debris avalanche dynamics. Engineering Geology, 38(3–4):261 – 297.

von Mises, R., 1913. Mechanik der festen körper im plastisch deformablen zustand. Nachrichten von der Gesellschaft der Wissenschaften zu Göttingen, Mathematisch-Physikalische Klasse, 1:582–592.

Ward, S.N. and Day, S., 2006. Particulate kinematic simulations of debris avalanches: interpretation of deposits and landslide seismic signals of mount saint helens, 1980 may 18. Geophysical Journal International, 167(2):991–1004.

Weinhart, T., Thornton, A.R., Luding, S., and Bokhove, O., 2012. Closure relations for shallow granular flows from particle simulations. Granular Matter, 14(4):531–552.

Whipple, K., 1997. Open-channel flow of bingham fluids: Applications in debris-flow research. Journal of Geology, pages 243–262.

Yang, S.C. and Hsiau, S.S., 2001. The simulation and experimental study of granular materials discharged from a silo with the placement of inserts. Powder Technology, 120(3):244 – 255.

Young, D., Munson, B., Okiishi, T., and Huebsch, W., 2010. A Brief Introduction To Fluid Mechanics. John Wiley & Sons. ISBN 9780470596791.

Young, D., 2003. Iterative solution of large linear systems. Dover Publications, New York.

Yu, H., 2006. Plasticity and Geotechnics. Advances in Mechanics and Mathematics Series. Springer Science+Business Media, LLC. ISBN 9780387335995.

Zhu, H., Zhou, Z., Yang, R., and Yu, A., 2008. Discrete particle simulation of particulate systems: A review of major applications and findings. Chemical Engineering Science, 63(23):5728 – 5770.

List of Figures

Abbreviations and Symbols

Abbreviations

1D, 2D	one-, two-dimensional
CCD	charge coupled devices
CFD	computational fluid dynamics
CG	conjugate gradient method
DAM	depth-averaged model
DEM	discrete element method
IF	interface
MAC	marker-and-cell method
N-DAM	non depth-averaged model
NOC	non-oscillatory central
PIV	particle image velocimetry
SOR	successive overrelaxation method
TVD	total variation diminishing
VOF	volume of fluid method

Latin Symbols

$\mathbf{A}$	Coulomb friction matrix; (3.24), page 26
A, B	constants in Drucker-Prager yield criterion; (2.28), page 13
$\mathbf{B}$	Coulomb friction matrix; (3.24), page 26
$\mathbf{b}$	body force density
$\mathbf{b}_c$	inhomogeneity vector of Coulomb friction; (3.24), page 26
$\mathbf{b}_L$	inhomogeneity vector of pressure equation; (3.28), page 26

$\mathbf{b}_p$	inhomogeneity vector of Poisson equation; (3.18), page 24
$\mathbf{C}$	elasticity tensor
c	cohesion
c^{F}	friction factor; (3.12), page 21
$C_{i,j}$	cell with centre at $((i-0.5)\,dx, (j-0.5)\,dz)$
$c^p_{i,j}$	pressure coefficient in Coulomb friction; (3.23), page 25
$c^u_{i,j}$	bottom velocity coefficient in Coulomb friction; (3.23), page 25
c_r	restitution coefficient
$\mathbf{D}$	strain rate tensor
$\mathbf{d}$	displacement vector
$D^c_{1/2}$, $D^p_{1/2}$, D^u, D^w	discretisations of $\|\|\mathbf{D}\|\|$; Appendix B
dt	time step size
dx	mesh width in x-direction
dz	mesh width in z-direction
e	specific internal energy
$e_{k,i}$	coefficients describing the exponential temporal variation of q_i
E_{kin}, E^p_{pot}, E^g_{pot}, E_{fric}	kinetic, pressure potential, gravitational potential, and frictional energies; (6.12), page 87
E	total energy function; (6.12), page 87
F	part of right hand side of x-momentum equation; (3.5), page 20
f_0, f_x, f_z	coefficients in $\mathbf{F}^P$; Appendix B.3
$f^{(1)}_{i,j}$, $f^{(2)}_{i,j}$	(3.25), page 26 and Appendix B.4
F^r_e	effective friction ratio; (3.13), page 21
Fr	Froude number
$\mathbf{F}$	$= (F, G)^T$; (4.7), page 50
$\mathbf{F}^B$	Bingham part of $\mathbf{F}$; (B.7), page 103
$\mathbf{F}^N$	Newtonian part of $\mathbf{F}$; (B.6), page 103
$\mathbf{F}^P$	pressure-dependent part of $\mathbf{F}$; (B.8), page 103

$\mathbf{g}$	gravitational acceleration
G	part of right hand side of z-momentum equation; (3.6), page 20
g_0, g_x, g_z	coefficients in $\mathbf{G}^P$; Appendix B.3
h	flow depth
h_{in}	inflow depth
H	characteristic flow depth
H_s	height of stored material within a silo
i, j	indices
i_{max}	number of cells in x-direction
j_{max}	number of cells in z-direction
$K_{act/pas}$	active/passive earth pressure coefficient
Kn	Knudsen number
$\mathbf{L}$	pressure matrix; (3.28), page 26
$l_{k,i}$	coefficients describing the linear temporal variation of q_i
L	characteristic length scale
L_s	length of stored material within a silo
$\mathbf{M}$	Poisson equation matrix; (3.18), page 24
m	mass density
m_c	coulomb friction smoothing exponent
m_y	yield stress smoothing exponent; (3.4), page 19
$\mathbf{n}$	surface normal vector
N	normal pressure on a surface
N_c	number of Coulomb cells
N_d	dimension of tensor/matrix
N_I	number of inner fluid cells
P	characteristic pressure
p	isotropic pressure

p_D	dynamic pressure
p_H	hydrostatic pressure
$p_{i,j}$	discrete value of pressure at cell centre $((i-0.5)\,dx, (j-0.5)\,dz)$
$\mathbf{p}$	vector of discretised pressures; (3.18), page 24
$\mathbf{Q}$	relates $\mathbf{b}_p$ to $\mathbf{u}^b$; (3.26), page 26
q_i	coefficients describing $u_{\text{out}}(z)$
$\mathbf{q}$	heat flux vector
$\mathbf{q}_p$	inhomogeneity vector; (3.26), page 26
r	radius of Mohr's circle
s	net acceleration in DAM's momentum balance; (4.15), page 52
s_e	specific energy supply
s_f	frictional resistance
s_g	gravitational acceleration
$\mathbf{s}$	stress vector across a surface
$\mathbf{t}$	surface tangential vector
T	characteristic time scale, shear stress on a surface
t	time
t_f	after this time, the flow front passed the silo gate; Chapter 5
$\mathbf{u}$	velocity vector
U	characteristic velocity
u	velocity component in x-direction
$\mathbf{u}^b$	vector of discretised bottom velocities
$u_{i,j}$	discrete value of x-velocity at edge midpoint $(i\,dx, (j-0.5)\,dz)$
u_{in}	inflow velocity
u_{out}	outflow velocity at silo gate
$\tilde{u}$	global velocity average
v	velocity magnitude

V	material volume
V^{2D}	two-dimensional material volume in x-z plane
w	velocity component in z-direction
w_c	channel width
$w_{i,j}$	discrete value of z-velocity at edge midpoint $((i-0.5)\,dx, j\,dz)$
x_d	distance from point of mass release along the channel to point where flow hits the horizontal reference datum
x_{IF}	interface position
x, y, z	Cartesian coordinates

Greek Symbols

β	coefficient of pressure gradient term in DAM; (4.15), page 52
δ	bed friction angle
$\mathcal{E}$	energy function; (6.4), page 85
ε	shallowness parameter
$\boldsymbol{\varepsilon}$	strain tensor
η	dynamic viscosity
η_{eff}	effective dynamic viscosity
$\dot{\gamma}$	shear rate
κ	donor-cell discretisation parameter
λ	mean free path
λ_0	$\lambda(t)$ at $t = 0$
$\lambda(t)$	time dependent part of energy function; (6.7), page 85
μ	integration constant of granular flux; (6.8), page 85
ν	kinematic viscosity
ν_{eff}	effective kinematic viscosity
Ω	flow domain
Φ	volume fraction
ϕ	internal friction angle

ψ	integration constant of granular flux; (6.8), page 85
ρ	bulk density
ρ_g	particle density of grains
Σ	sum of kinetic and pressure potential energies; (6.13), page 87
σ	normal stress
$\boldsymbol{\sigma}$, σ_{ij}	Cauchy stress tensor, its components
σ_1, σ_2	principal stresses in 2D stress state
$\boldsymbol{\sigma}_D$	deviatoric stress tensor
σ_m	centre of Mohr's circle
$\boldsymbol{\sigma}_V$	volumetric stress tensor
τ	shear stress
τ_c	tensile strength contribution to τ_y
τ_p	proportionality constant in $\tau_y(p)$; (4.5), page 49
τ_y	yield stress
ζ	inclination angle

Miscellaneaous Symbols

$\mathbb{1}$	unit tensor
$\lvert(\bullet)\rvert$	absolute value
$\nabla \cdot \mathbf{v}$, $\operatorname{div} \mathbf{v}$	divergence of vector or matrix $\mathbf{v}$
$\operatorname{grad} \mathbf{v}$	$= (\nabla \mathbf{v})$, gradient of a vector $\mathbf{v}$
Δ	Laplace operator
∇	del operator, nabla
$\dfrac{\partial}{\partial x}$, ∂_x	partial derivative with respect to x
$\dfrac{d}{dt}$, $\dot{(\bullet)}$	total time derivative
$\overline{(\bullet)}$	depth-average
$(\bullet)'$	derivative

$\det \mathbf{M}$	determinant of matrix $\mathbf{M}$
$\emptyset_{\text{grain}}$	grain diameter
$\hat{(\bullet)}$	dimensionless quantity
$\mathbf{M}_1 : \mathbf{M}_2$	$= \text{tr}\left(\mathbf{M}_1 \mathbf{M}_2^{\text{T}}\right)$, inner matrix product
I_M, II_M, III_M	first, second, and third invariant of tensor $\mathbf{M}$
$\|\| (\bullet) \|\|$	norm
$\mathbf{a} \otimes \mathbf{b}$	$= \mathbf{ab}$, dyadic (tensor) product of vectors $\mathbf{a}$ and $\mathbf{b}$.
$\mathbf{a} \cdot \mathbf{b}$	scalar product of vectors $\mathbf{a}$ and $\mathbf{b}$.
$(\bullet)^{\text{b}}$	variable evaluated at bottom surface
$(\bullet)^{c}$	variable evaluated at c-grid
$(\bullet)^{(n)}$	variable at time level $t^{(n)}$
$(\bullet)^{p}$	variable evaluated at p-grid
$(\bullet)^{\text{surf}}$	variable evaluated at free surface
$(\bullet)^{u}$	variable evaluated at u-grid
$(\bullet)^{w}$	variable evaluated at w-grid
$\text{tr}\, \mathbf{M}$	trace of matrix $\mathbf{M}$
$\mathbf{M}^T$	transpose of matrix $\mathbf{M}$

Acknowledgements

First and foremost, I would like to thank my supervisors Prof. Dr. Stephen A. Miller and Dr. Shiva P. Pudasaini, for the extremely interesting research project and their full support. In particular, I thank Shiva for his contribution to our good work and his scientific input. In addition, I would like to express my sincere gratitude to Stephen for his additional financial support. I also would like to express my special thanks to Prof. Dr. Andreas Kemna for his commitment to the examination of this work. Furthermore, many thanks are given to the remaining members of the examination board, Prof. Dr. Andreas Hense and Prof. Dr. Ian C. Brock, for being part of the committee.

I wish to extend my gratitude to all members of the Geodynamics / Applied Geophysics group for the nice working atmosphere. In particular, I am very grateful to Dr. Andreas Dreist for the excellent IT working conditions and to Lisa Takacs for her administrative support.

The Deutsche Forschungsgemeinschaft (DFG), the German Science Foundation, provided a financial support through contract no. PU 381-1,2: *Transition of a granular flow into the deposit*, for which I am very thankful.

Finally, I would like to express immense thanks to my companion in life Gregor Klabisch, my parents Gisela and Harry Domnik, my sister Kirsten Domnik, as well as my friends, for their encouragement, thoughtfulness and undesigning support.